Fall 2022

DISORDER EFFECTS IN FRUSTRATED MAGNETS AND ABSORBING STATE TRANSITIONS

Xuecheng Ye
Missouri University of Science and Technology

Department: Physics

DISORDER EFFECTS IN FRUSTRATED MAGNETS AND ABSORBING STATE TRANSITIONS

by

XUECHENG YE

A DISSERTATION

Presented to the Graduate Faculty of the

MISSOURI UNIVERSITY OF SCIENCE AND TECHNOLOGY

In Partial Fulfillment of the Requirements for the Degree

DOCTOR OF PHILOSOPHY

in

PHYSICS

2022

Approved by:

Thomas Vojta, Advisor
Aleksandr V. Chernatynskiy
Alexey Yamilov
Gerald Wilemski
Yanzhi Zhang

PUBLICATION DISSERTATION OPTION

This dissertation consists of the following three articles, formatted in the style used by the Missouri University of Science and Technology.

Paper I: X. Ye, R. Narayanan, and T. Vojta, Stripe order, impurities, and symmetry breaking in a diluted frustrated magnet, pages 21-52. Published in Physical Review B 105, 024201 (2022)

Paper II: X. Ye and T. Vojta, Contact process with simultaneous spatial and temporal disorder, pages 53-91. Published in Physical Review E 106, 044102 (2022)

Paper III: X. Ye et al., Unconventional Josephson junctions with topological Kondo insulator weak links, pages 92-107. Published in Physical Review B 100, 104505 (2019)

ABSTRACT

Correlation, topology, and disorder can fundamentally affect the properties of interacting many-particle systems. After a short introduction which covers the basic concepts of phase transitions and scaling as well as the physics of Josephson junctions, the dissertation focuses on three separate projects.

The first project is motivated by the stripe and nematic phases observed e.g. in cuprate superconductors and iron pnictides. To understand the effects of disorder on such phases, we have investigated the behavior of the diluted J_1-J_2 Ising model. Spinless impurities generate a random-field disorder for the spin-density (stripe) order parameter, which destroys the stripe phase. Combining symmetry arguments, percolation theory and Monte Carlo simulations, we show that a weak spatial interaction anisotropy restores the stripe phase. Moreover, we determine the phase diagram and explain it using percolation theory. We also analyze the critical behavior of the transition into the stripe phase.

Many-particle systems far from thermal equilibrium can undergo abrupt transitions between different steady states which resemble thermal transitions. In the second project, we have studied the absorbing-state phase transition of the 1-D contact process, which can be understood as a model of epidemic spreading, under the combined influence of spatial and temporal disorders. We discuss the stability of the directed percolation universality class against such disorder, and then perform Monte Carlo simulations to confirm our theory. We also investigate the Griffiths singularities that accompany the nonequilibrium transition.

In the third project, we have constructed unconventional Josephson junctions by coupling superconducting Nb leads to the surface states of a SmB_6 crystal. We have found a robust critical current at low temperatures which responds to out-of-phase magnetic fields. This behaviour significantly deviatates from the usual Fraunhofer patterns, forming so-called Shaphiro steps. We have also found the effects of Kondo breakdown in our devices, as well as the coexistence of magnetism with superconductivity at the SmB_6 surface.

ACKNOWLEDGMENTS

First, I want to give my deepest thanks to my advisor Dr. Thomas Vojta for his guidance and support, and for allowing me to be his student in the first place. He is not only one of the most successful professors in the field, but also a very understanding teacher, and an even greater role model in my life. I can't thank him enough.

Secondly, I want to thank Dr. Cihan Kurter for guiding me into the graduate research. She helped me a lot in guiding a new graduate student to read papers and operating machines, and helped me to publish my first paper. She also provided help and support for me even when she was no longer my teacher.

I wish to give my thanks to my committee members, Dr. Aleksandr V. Chernatynskiy, Dr. Alexey Yamilov, Dr. Gerald Wilemski and Dr. Yanzhi Zhang. Thanks for the valuable disccussion and understanding, especially when I had to postpone my graduation for several times.

I also want to thank all the professors and other teachers in our Physics department. I give my special thanks to the teachers, Prof. Jerry Peacher, Prof. John Story, Prof. Paul Parris, Prof. Ulrich Jentschura and Prof. George Waddill. They have taught me physics and advised me to become a good researcher. I also want to thank our fabulous and magical office staff Pamela Crabtree and Janice Gargus. They have made every nonacademic thing so easy that I could dedicate myself completely to study and research.

I give my thanks to my late mom, who has educated me to become a scientist and gave her everything to me, and my farther, who is trying his best to love me in every way. Also thanks to my aunt and sister for the parenting support when I am far from home.

Also thanks to Simeng, the love of my life. She is my everything.

TABLE OF CONTENTS

Page

PUBLICATION DISSERTATION OPTION iii

ABSTRACT iv

ACKNOWLEDGMENTS v

LIST OF ILLUSTRATIONS x

LIST OF TABLES xiii

SECTION

1. INTRODUCTION 1

1.1. PHASE TRANSITIONS 1

1.1.1. Order Parameter and Landau Theory 2

1.1.2. Scaling Hypothesis 3

1.2. DISORDER EFFECTS AT PHASE TRANSITIONS 6

1.2.1. Random Field Disorder vs Random Mass Disorder 6

1.2.2. Imry-Ma Criterion 7

1.2.3. Harris Criterion 8

1.2.4. Rare Regions and Griffiths Effect 10

1.3. APPLICATIONS 12

1.3.1. Magnetic Stripe Order and the $J_1 - J_2$ Ising Model 12

1.3.2. Nonequilibrium Phase Transitions in the Contact Process 14

1.4. JOSEPHSON JUNCTION 16

1.4.1. Topological Insulator 17

1.4.2. Topological Kondo Insulator 19

1.4.3. Shaphiro Steps 19

PAPER

I. STRIPE ORDER, IMPURITIES, AND SYMMETRY BREAKING IN A DILUTED FRUSTRATED MAGNET 21

ABSTRACT 21

1. INTRODUCTION 22

2. MODEL AND RANDOM-FIELD MECHANISM 24

2.1. DILUTED ANISOTROPIC J_1-J_2 ISING MODEL 24

2.2. RANDOM-FIELD DISORDER 26

2.3. DOMAIN FORMATION 28

2.4. MAGNETIC PHASE TRANSITION 29

3. MONTE CARLO SIMULATIONS 30

4. RESULTS 34

4.1. ISOTROPIC INTERACTIONS, $\Delta J = 0$ 34

4.2. ANISOTROPIC INTERACTIONS, $\Delta J > 0$ 36

4.3. CRITICAL BEHAVIOR 40

5. CONCLUSION 43

ACKNOWLEDGEMENTS 46

REFERENCES 46

II. CONTACT PROCESS WITH SIMULTANEOUS SPATIAL AND TEMPORAL DISORDER 53

ABSTRACT 53

1. INTRODUCTION 54

2. CONTACT PROCESS 56

3. SCALING SCENARIOS 58

3.1. CLEAN CONTACT PROCESS: CONVENTIONAL POWER-LAW CRITICAL BEHAVIOR 58

3.2. SPATIALLY DISORDERED CONTACT PROCESS: INFINITE-RANDOMNESS CRITICAL BEHAVIOR 61

3.3. TEMPORALLY DISORDERED CONTACT PROCESS: INFINITE-NOISE CRITICAL BEHAVIOR 62

4. RARE EVENTS AND GRIFFITHS SINGULARITIES 64

4.1. SPATIAL DISORDER 64

4.2. TEMPORAL DISORDER 66

5. SIMULATIONS METHODS 67

6. RESULTS: CRITICAL BEHAVIOR 68

6.1. GENERALIZED HARRIS CRITERION 68

6.2. ADDING WEAK SPATIAL DISORDER TO THE TEMPORAL DISORDERED CONTACT PROCESS 70

6.3. ADDING WEAK TEMPORAL DISORDER TO SPATIAL DISORDER CASE 73

6.4. SPATIAL AND TEMPORAL DISORDER OF COMPARABLE STRENGTH 75

7. RESULTS: RARE REGIONS AND GRIFFITHS SINGULARITIES 79

7.1. THEORY 79

7.2. SIMULATION RESULTS 81

8. CONCLUSIONS 85

ACKNOWLEDGEMENTS 87

REFERENCES 88

III. UNCONVENTIONAL JOSEPHSON JUNCTIONS WITH TOPOLOGICAL KONDO INSULATOR WEAK LINKS 92

ABSTRACT 93

1. INTRODUCTION 94

2. EXPERIMENTAL 95

3. CONCLUSION 102

ACKNOWLEDGEMENTS 102

REFERENCES 102

SECTION

2. SUMMARY AND CONCLUSIONS 108

REFERENCES 110

VITA 115

LIST OF ILLUSTRATIONS

Figure Page

1.1. Schmatic phase diagram of water 1

1.2. Derivation of Imry-Ma criterion. Domain of the spin-up phase embedded in spin-down bulk. 8

1.3. Derivation of Harris criterion. The system is divided into independent blocks, each with its own critical temperature. 9

1.4. Sketch of a diluted magnet, the shaded region is devoid of impurities and acts as a rare region 11

1.5. Interactions of the anisotropic $J_1 - J_2$ model 13

1.6. Phase diagram of $J_1 - J_2$ Hamiltonian for both uncorrelated and anticorrelated site dilution at an impurity concentration of $p = 1/8$ compared to the phase diagram of the undiluted system (open symbols) 14

1.7. Random field mechanism in diluted $J_1 - J_2$ model. 14

1.8. Energy band of topological insulator [49] 18

1.9. AC Josephson effect giving rise to Shaphiro steps in I-V 20

PAPER I

1. Interactions of the anisotropic J_1-J_2 model. 25

2. Random-field mechanism: A pair of vacancies on horizontal nearest-neighbor sites prefers horizontal stripes (left) over vertical stripes (right) by an energy difference of $2J_1$. 26

3. Root-mean-square random-field energy of a perfect stripe state per lattice site, $\langle E_{RF}^2 \rangle^{1/2}/L^2$, vs. linear system size L for several dilutions p. 27

4. Energy per site E/N vs. Monte Carlo sweep for a system of linear size $L = 96$, $\Delta J = 0$ and temperature $T = 1.15$. 32

5. Comparison of simulations with hot starts (random initial spin configuration, run starts at highest temperature) and cold starts (spins initially in perfect stripe state, run starts at lowest temperature). 33

6. Average Binder cumulant g_{av} vs. temperature T for isotropic interactions $\Delta J = 0$ and several system sizes L. $p = 1/4$, $J_1 = J_2 = 1$. 35

7. Snapshots of the local nematic order parameter η_i of one particular disorder configuration for several anisotropies: $\Delta J = 0$, 0.002, 0.01, 0.05 (left to right). . 35

8. Average Binder cumulant $g_{\rm av}$ vs. temperature T for anisotropic interactions with $\Delta J = 0.2$ and several system sizes L. $p = 1/4$, $J_1 = J_2 = 1$. 37

9. Average Binder cumulant $g_{\rm av}$ vs. temperature T for anisotropic interactions with $\Delta J = 0.005$ and several system sizes L. $p = 1/4$, $J_1 = J_2 = 1$. 37

10. Transition temperature T_c into the long-range stripe ordered phase vs. interaction anisotropy ΔJ for $p = 1/4$, $J_1 = J_2 = 1$. 39

11. Semilog plot of the specific heat C vs. system size L at the critical temperature $T_c = 1.8670$ for $\Delta J = 0.2$, $J_1 = J_2 = 1$, $p = 1/4$. 41

12. Double logarithmic plot of $\chi_s L^{-7/4}$ vs. system size L at the critical temperature $T_c = 1.8670$ for $\Delta J = 0.2$, $J_1 = J_2 = 1$, $p = 1/4$. 42

PAPER II

1. Inverse survival probability $1/P_s$ vs $\ln t$ close to criticality.($p_t = 0.2$, $c_t = 0.05$, $\Delta t = 6$, $p = 0.2$ and $c = 0.8$). 71

2. $(N_s/t)^{-1/y_N}$ and $(R/t)^{-1/y_R}$ vs $\ln t$ at criticality, $\lambda_c = 28.4$ for $p_t = 0.2$, $c_t = 0.05$, $\Delta t = 6$, $p = 0.2$ and $c = 0.8$. 71

3. Inverse survival probability $1/P_s$ vs $\ln t$ at criticality for different c and $p_t = 0.2$, $c_t = 0.05$, $\Delta t = 6$, $p = 0.2$. 72

4. Left: Critical infection rate λ_c as a function of spatial disorder strength c for $p_t = 0.2$, $c_t = 0.05$, $p = 0.2$. Right: Critical λ_c as a function of temporal disorder strength c_t for $p = 0.3$, $c = 0.2$, $p_t = 0.2$. 73

5. Survival probability vs time plotted as $P_s^{-1/\bar{\delta}}$ vs $\ln t$ close to criticality, where $\bar{\delta} = 0.38197$ ($p_t = 0.2$, $c_t = 0.8$, $\Delta t = 6$, $p = 0.3$ and $c = 0.2$). 74

6. $(N_s)^{1/\Theta}$ and $(R)^{\psi}$ vs $\ln t$ at criticality $\lambda_c = 5.52$ for $p_t = 0.2$, $c_t = 0.8$, $\Delta t = 6$, $p = 0.3$, and $c = 0.2$. 74

7. Survival probability vs time plotted as $P_s^{-1/\bar{\delta}}$ vs $\ln t$ at criticality for different c_t, where $\bar{\delta} = 0.38197$ ($p_t = 0.2$, $\Delta t = 6$, $p = 0.3$ and $c = 0.2$). 75

8. Schematic renormalization group flow on the critical manifold spanned by the spatial and temporal disorder strengths. (DP marks the direct percolation fixed point of the clean contact process.)..... 76

9. Survival probability vs time for $p_t = 0.2$, $c_t = 0.05$ $p = 0.2$, $c = 0.05$, and $\Delta t = 6$) 77

10. Number of active sites vs time for $p_t = 0.2$, $c_t = 0.05$ $p = 0.2$, $c = 0.05$, and $\Delta t = 6$) 78

11. Main panel: $\ln P_s$ vs $\ln t$ for different λ below criticality $\lambda_c \approx 5.52$ for $p = 0.3$, $c = 0.2$, $p_t = 0.2$, $c_t = 0.8$ and $\Delta t = 6$. 82

12. Main panel: $\ln P_s$ vs t for different λ between 2.3 and 3.9, far from criticality $\lambda_c \approx 7.26$ for $p = 0.3$ and $c = 0.2$, $p_t = 0.2$, $c_t = 0.4$ and $\Delta t = 6$). 83

13. (a) $\ln P_s$ vs $\ln t$ for different λ below criticality $\lambda_c \approx 7.26$ for $p = 0.3$, $c = 0.2$, $p_t = 0.2$, $c_t = 0.4$ and $\Delta t = 6$). (b) $\ln P_s$ vs $t^{1/y}$ for the same data. 84

14. (a) Double-log plot of lifetime τ vs system size L for different λ above criticality $\lambda_c \approx 11.08$ for $p = 0.3$, $c = 0.2$, $p_t = 0.2$, $c_t = 0.2$ and $\Delta t = 6$. (b) The same data plotted as $\ln \tau$ vs $L^{1/y}$, with y chosen such that the data fall onto straight lines. 85

PAPER III

1. (Color online) (a) Scanning electron microscopy SEM image of one of the studied devices, junction-1, made with two Nb leads ~ 100 nm apart on a polished crystal of SmB_6. (b) Current-voltage I-V characteristics of the junction-1 for a set of temperatures. The supercurrent persists up to 3.6 K. 96

2. (Color online) (a) AC Josephson effect giving rise to Shaphiro steps in IV and (b) corresponding peaks in differential resistance for another sample, junction-1. (c) and (d) Color plots demonstrating such steps for junction-2 at two different frequencies. 97

3. (Color online) (a), (b) Magnetic diffraction patterns of the I_c for the junction-3 and the junction-2 as the out of plane magnetic field is swept in forward and reverse directions. (c) and (d) Color plots of dV/dI vs bias current as a function of perpendicular magnetic field for the junction-1..... 98

4. (Color online) (a) Color plot of dV/dI vs bias current as a function of temperature for junction-4. (b) Temperature evolution of hysteresis in normal state resistance with sweep direction for junction-4. (c) Rate dependence of magnetic field hysteresis in normal state resistance of junction-4. 100

LIST OF TABLES

Table Page

1.1. Critical exponent values in Landau (mean-field) theory and for the 2D Ising universality class [3, 9]..... 5

1. INTRODUCTION

1.1. PHASE TRANSITIONS

A phase represents a state of matter. Its properties are uniform in space and time-independent, and its qualitative characteristics do not change upon small changes of external parameters (control parameters) such as pressure, temperature, magnetic field, and chemical composition. Correspondingly, a phase transition is defined as a qualitative change in a thermodynamic system in response to a change of the control parameters. The transition between two phases happens when one crosses the boundary in the phase diagram, which shows the different phases of a material as a function of the control parameters. A well-known example are the three phases of water (solid, liquid and gas), as shown in Figure 1.1. For water, the phase boundaries correspond to the melting of ice and the evaporating of liquid water.

First-order phase transitions involve phase coexistence and latent heat. During the transition, the system either absorbs or releases a fixed amount of energy per mass to turn one phase into the other at the phase boundary. For example, ice and liquid water coexist at the melting transition at 0°C, and a finite amount of heat is necessary to melt the ice at

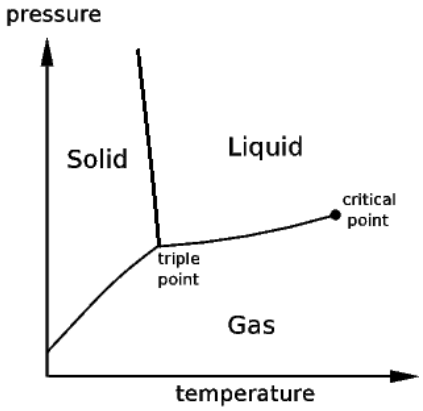

Figure 1.1. Schmatic phase diagram of water

this temperature. This implies that the first derivative of the free energy with respect to temperature is discontinuous. In contrast, second-order phase transitions (continuous phase transitions) do not feature latent heat or phase coexistence. Their first derivatives of the free energy (such as entropy and magnetization) are continuous, but the second derivatives such as susceptibility and specific heat are potentially divergent at the transition point.

1.1.1. Order Parameter and Landau Theory. Modern theories of phase transitions are mostly built on Landau theory [1, 2, 3, 4]. Landau generalized mean-field theory and proposed the concept of the order parameter, which is a macroscopic thermodynamic observable that has a nonzero value in the ordered phase and vanishes in the disordered phase. Laudau theory assumes that the free energy F_L of a system can be described as an analytical function of the order parameter. The physical state then corresponds to the minimum of F_L with respect to the order parameter. For example, in a ferrormagnetic system using magnetization m as its order parameter, the free energy F_L can be written in the form:

$$F_L = F_L(0) + hm + rm^2 + um^4 + O(m^5), \tag{1.1}$$

where h is the external field, and r and u are expansion coefficients that are independent of the order parameter, yet dependent on all other degrees of freedom. There is no cubic term because of Z_2 symmetry. They vary with the external parameters such as temperature, pressure, etc. In the absence of an external field ($h = 0$), the free energy F_L is an even function. This case is easily discussed. If $r \geq 0$, F_L reaches its minimum at $m = 0$. This represents the system in the disordered paramagnetic phase. On the other hand, if $r < 0$, the free energy F_L now reaches its minimum value at nonzero magnetization,

$$m = \pm\sqrt{-r/2u}. \tag{1.2}$$

This solution represents the ordered, ferrormagnetic phase.

The phase transition between the paramagnetic and ferromagnetic phases happens at $r = 0$, thus, r is a measure of the distance from the transition point (critical point). From Equation (1.2), it follows that m is a continuous function of r at the phase transition point $r = 0$. In general, we can define the critical exponent β of the order parameter using

$$m \sim (-r)^{\beta}. \tag{1.3}$$

Landau theory predicts the value $\beta = 1/2$, identical to the value in simple mean-field theories. Other critical exponents will be introduced in the next section.

Landau theory can also describe a discontinuous phase transition. Take the same example of a ferrormagnet in the ordered phase, $r < 0$. At $h < 0$, the system will be in a phase with $m < 0$. If we tune the field from $h < 0$ to $h > 0$, the system will discontinuously change to a phase with $m > 0$. At the transition point, $h = 0$, the phases with $m > 0$ and $m < 0$ coexist.

1.1.2. Scaling Hypothesis. Scaling theory is a phenomenological theory of the behavior close to the transition point of a continuous phase transition, i.e. close to criticality. It is based on the observation that the correlation length ξ becomes very large close to the critical point ($r = 0$) and diverges as

$$\xi \sim |r|^{-\nu}. \tag{1.4}$$

Here, ν is the correlation length critical exponent. This suggests that the correlation length is the only relevant length scale in the system close to the critical point. Thus, if all lengths in the system are rescaled by a positive arbitrary length scale factor b while the external parameters are adjusted so that the correlation length retains its value, the physical properties do not change. According to the scaling hypothesis [5, 6], we need to rescale the distance from criticality r_b as rb^{y_r} and field h_b as hb^{y_h}, where y_r and y_h are critical exponents. This leads to a homogeneity relation for the free energy density

$f = -(k_B T/V)\ln(Z)$ that has the form

$$f(r,h) = b^{-d} f(rb^{y_r}, hb^{y_h}). \tag{1.5}$$

Here, d is the space dimentionality. Under the same transformation, the correlation length ξ behaves as

$$\xi(r,h) = b\xi(rb^{y_r}, hb^{y_h}). \tag{1.6}$$

The freedom of setting the length scale factor b to an arbitary value can be used to derive the behavior of various observables. Choosing $b = r^{-1/y_r}$, the free energy density and correlation length now become,

$$f(r,h) = r^{d/y_r} f_S(hr^{-y_h/y_r}), \tag{1.7}$$

$$\xi(r,h) = r^{-1/y_r} \xi_S(r^{-y_h/y_r} h), \tag{1.8}$$

where f_S and ξ_S are unary scaling functions using the combination $r^{-y_h/y_r} h$ as argument. In the absence of a field ($h = 0$), combining Eqs. (1.4) and (1.8) we have $\nu = 1/y_r$. Moreover, by taking appropriate derivatives of $f(r,h)$, we obtain the order parameter m,

$$m(r,h) = -(\frac{\partial f}{\partial h}) = b^{y_h - d} m(rb^{1/\nu}, hb^{y_h}). \tag{1.9}$$

The susceptibility χ reads

$$\chi(r,h) = (\frac{\partial m}{\partial h}) = b^{2y_h - d} \chi(rb^{1/\nu}, hb^{y_h}), \tag{1.10}$$

and the specific heat C reads

$$C(r,h) = -T(\frac{\partial^2 f}{\partial^2 r}) = b^{2/\nu - d} C(rb^{1/\nu}, hb^{y_h}). \tag{1.11}$$

Table 1.1. Critical exponent values in Landau (mean-field) theory and for the 2D Ising universality class [3, 9]

critical exponent	**Landau theory**	**2-dimensional Ising**
α	0	0
β	1/2	1/8
γ	1	7/4
δ	3	15
ν	1/2	1

Setting b equal to $r^{-\nu}$ as before and $h = 0$, these three equations now yield,

$$m \sim r^{(d-y_h)\nu} = r^{\beta}, \tag{1.12}$$

$$\xi \sim r^{(d-2y_h)\nu} = r^{-\gamma}, \tag{1.13}$$

$$C \sim r^{d\nu-2} = r^{-\alpha}, \tag{1.14}$$

which defines the susceptibility critical exponent γ and specific heat critical exponent α. By setting $b = h^{-1/y_h}$ and $r = 0$, Equation (1.12) gives

$$m \sim h^{d/y_h-1} = h^{1/\delta} \tag{1.15}$$

where δ is the critical isotherm exponent. Their values can be found in Table 1.1. By comparing these definitions of critical exponents, we find that they are not all independent. Eliminating y_h, we obtain the following scaling relations [5, 7, 8]

$$\alpha = 2 - d\nu \qquad \text{Josephson's Identity,} \tag{1.16}$$

$$2\beta + \gamma + \alpha = 2 \qquad \text{Rushbook's Identity,} \tag{1.17}$$

$$\beta(\delta - 1) = \gamma \qquad \text{Widom's Identity.} \tag{1.18}$$

1.2. DISORDER EFFECTS AT PHASE TRANSITIONS

The results discussed in the previous section are based on spatially homogeneous, or 'pure', systems. However, such pure systems are rather an expectation than the rule. In nature, almost any real material contains different types of defects and impurities which introduce quenched disorder into the system. This leads to a number of important questions, especially: Will the ordered phase still exist in the presence of quenched disorder? Will the phase transition remain sharp? Will the order of the transition or the critical behavior change under the influence of disorder? Before answering these questions, we must distinguish two fundementally different types of disorder.

1.2.1. Random Field Disorder vs Random Mass Disorder. Disorder or randomness can have different sources such as impurity atoms and vacancies or extended defects. Almost all disorder in condensed matter systems is time-independent over experimental time scales, so it is called $quenched$ disorder. In contrast, $annealed$ disorder changes over experimental time scales. Here we only discuss quenched disorder.

According to Landau, ordered phases can be classified according to their broken symmetries. This suggests that types of disorder should also be classified according to their symmetries. Consider, for example, an Ising ferromagnet in an external magnetic field $h(x)$ that varies randomly in space. This type of disorder is called random-field disorder. As it couples linearly to the order parameter, it appears in the linear term in the free energy Equation (1.1):

$$-h(x)m(x,r). \tag{1.19}$$

Random fields locally prefer one particular direction of m over others and thus $locally$ break the spin up-down symmetry. If the distribution of $h(x)$ is even, no direction is preferd globally, so the global symmetry is preserved (in the statistical sense).

In contrast, let us now consider a ferrormagnet with a number of randomly distributed vacancies. Since the vacancies do not prefer a particular spin direction, both local and global up-down spin symmetries of the Hamitonian are preserved. Yet, the vacancies cause local variations in the tendency towards ferromagnetism and change the critical temperature. This type of disorder is therefore called $random - T_C$ disorder, or random-mass disorder. In a Landau expansion, it couples to the square of the order parameter, leading to a random variation $\delta(x)$ in space of the quadratic coefficient. The corresponding quadratic term in the free energy Equation (1.1) reads

$$[r + \delta(x)]m^2(x, r). \tag{1.20}$$

1.2.2. Imry-Ma Criterion. A basic problem is whether a symmetry-breaking ordered phase can suvive random-field disorder. In order to solve this problem, Imry and Ma [10] analyzed whether macroscopic phase coexistence is possible under random-field disorder.

As an example, consider a d-dimensional ferromagnet (FM) having a spin-up domain of linear size L embedded within a larger spin-down domain as shown in Figure 1.2. In the absence of random fields, the bulk free energy densities of both domains are identical.

The free energy loss due to the formation of the domain wall is proportional to the domain wall area,

$$E_{DW} \sim L^{d-1}, \tag{1.21}$$

and the free energy gain from aligning the spin-up domain with the local random fields can be estimated from the central limit theorem,

$$E_{dis} \sim L^{d/2}. \tag{1.22}$$

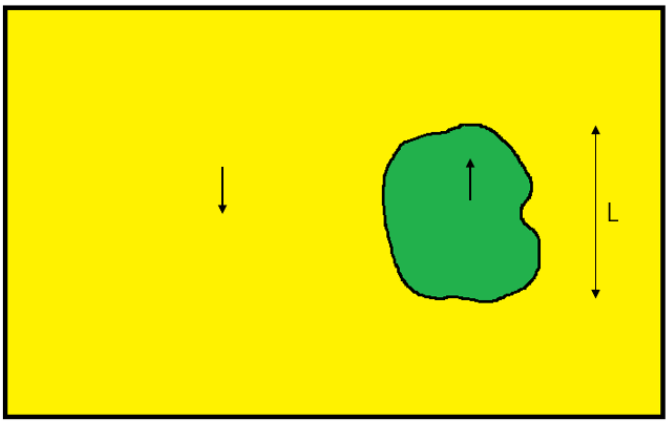

Figure 1.2. Derivation of Imry-Ma criterion. Domain of the spin-up phase embedded in spin-down bulk.

Based on Imry and Ma, we need to compare these two different energies. If $E_{dis} < E_{DW}$, the formation of domains is unfavorable, and the uniformly ordered FM phase is stable. If $E_{dis} > E_{DW}$, domains proliferate, destroying the ferromagnetic state. This leads to a simple requirement for the dimension. If $d \leq 2$, quenched disorder will destroy the FM phase for arbitrary weak random fields because the disorder energy will allow a domain 'wall' for sufficently large L. For $d > 2$, in contrast, the ordered phase remains stable against sufficiently weak random fields. This result is called the Imry-Ma criterion [11]; it was later proven rigorously by Aizeman and Wehr [12] for classical phase transitions and by Aizeman, Greenblatt and Lebowitz [13] for quantum phase transitions.

1.2.3. Harris Criterion. At first, people believed that weak random-T_C (random-mass) disorder would destroy any critical point, because the system would break up into separate sub-regions which would undergo the phase transition at different temperatures, destroying the sharp change in thermodynamic observables associated with a phase transition. However, it was later found that phase transitions generically remain sharp under weak and short-range random-T_C disorder.

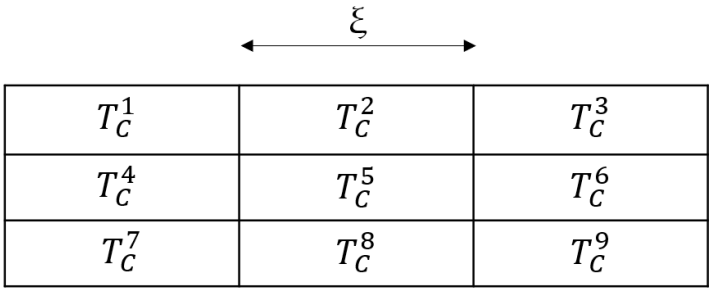

Figure 1.3. Derivation of Harris criterion. The system is divided into independent blocks, each with its own critical temperature.

Harris [14] found a simple criterion for the stability of a clean critical point of a classical phase transition against weak random-mass disorder. It was later proven to be applicable to quantum critical points as well [15].

Let us understand Harris' finding. Let us assume a system that undergoes a continuous phase transition in the presence of random-mass disorder at an overall critical temperature T_c. Imagine the system is divided into many sub-systems whose linear size is equal to the correlation length ξ, see Figure 1.3. Each sub-system i behaves independently and has its own 'critical temperature' T_C^i, which depends on its disordered local microscopic parameters.

We define ΔT_C to be the variation of these local critical temperatures. If $\Delta T_C > |T - T_C|$, some sub-systems will be in one phase and some will be in the other phase. Thus, a uniform phase transition is forbidden. On the other hand, If $\Delta T_C < |T - T_C|$, almost all blocks are in the same phase. Harris's argument compares these two cases, and concludes that a neccessary condition for the stability of the clean critical point against disorder is that $\Delta T_C \ll |T - T_C|$ always holds.

According to the central limit theorem, the variantion of the local critical temperatures ΔT_C can be estimated based on the size of the subsystems, i.e., the correlation length ξ:

$$\Delta T_C \sim \xi^{-d/2}. \tag{1.23}$$

If the distance from criticality r is replaced by $|T - T_C|$ in Equation (1.4), we obtain the relation:

$$|T - T_C| \sim \xi^{-1/\nu}. \tag{1.24}$$

Combining equations Eqs. (1.23) and (1.24), we find that the critical point is stable if $\xi^{-d/2} \ll \xi^{-1/\nu}$ for $\xi \to \infty$. This implies that, the clean critical point is stable if:

$$d\nu > 2. \tag{1.25}$$

This is the neccessary condition for the stability of a critical point, known as the famous Harris criterion [14]. Several generalizations of the Harris criterion to correlated disorder, temporal disorder, and others have been found, see e.g., Vojta and Dickmann [16].

1.2.4. Rare Regions and Griffiths Effect. In some disordered systems, the fate of the system will be dominated by rare events. Consider a randomly diluted classical magnet, see Figure 1.4. For a dilution not strong enough to destroy the phase transition, the critical temperature will drop from its clean value T_{C0} to T_C. Due to statistical fluctuations, there is a small but nonzero probability for large spatial regions (rare regions) that are devoid of impurities. Griffiths effects arise where the temperature is in the range $T_C < T < T_{C0}$; this region of the phase diagram is thus called Griffiths region or Griffiths phase [17]. In this temperature range, rare regions show local magnetic order even though the bulk system is in the paramagnetic phase (disordered phase). Griffiths proved that the rare regions produce a singularity in the free energy of the system in this temperature range [18].

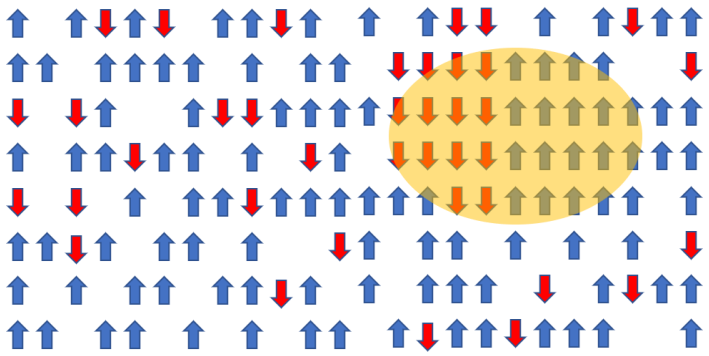

Figure 1.4. Sketch of a diluted magnet, the shaded region is devoid of impurities and acts as a rare region

The contributions of the rare regions to the thermodynamic behavior of the system can be estimated from the probability P for finding a rare region, which is a function of its size L_{RR}:

$$P(L_{RR}) \sim \exp(-AL_{RR}^{d}), \tag{1.26}$$

where A is a constant. Using this probability, the rare region contribution to, say, the magnetic susceptibility χ can be estimated as

$$\chi_{RR} \sim \int dL_{RR} P(L_{RR}) \chi(L_{RR}), \tag{1.27}$$

where $\chi(L_{RR})$ is the susceptibility of an individual rare region of size L_{RR}.

The Griffiths effect then depends on the effective dimension d_{RR} of the rare regions and its relation to the lower critical dimension d_C^- of the transition [19]. [d_C^- is the dimensionality below which there is no phase transition.]

(i) For $d_{RR} < d_C^-$, the rare region cannot undergo the phase transiton by itself. Since the contribution of the rare region to χ_{RR} scales as power law of its size, it cannot overcome the exponential decay of the rare region probability P in Equation (1.26). Thus, all the rare region effects are exponentially weak. This generically happens in classical systems with point defects.

(ii) For $d_{RR} = d_C^-$, the rare regions are exactly at the lower critical dimension. In this case, the rare region still cannot undergo the phase transition by itself, but $\chi(L_{RR})$ grows exponentially with L_{RR} so that it can overcome the decrease of the rare region probability P. This produces power-law Griffiths singularities that dominate the behavior at the critical point. The critical point itself features exotic exponential scaling (infinite-randomness critical point). Examples are the infinite-randomness critical point of the McCoy-Wu model [20, 21, 22, 23] and the quantum critical point of the transverse-field Ising model [15, 24].

(ii) For $d_{RR} > d_C^-$, the rare region can undergo the phase transition by itself and independently from the bulk system. Since the dynamices of the locally ordered rare regions completely freezes, the phase transition of the whole system will become smeared. An example is the classical three-dimensional Ising magnet with planar defects [25] or the quantum phase transition in itinerant Ising magnets [26, 27, 28].

1.3. APPLICATIONS

The concepts and phenomena discussed above can be used in many disorderd systems. In this section, we introduce their applications to the systems studied in papers I and II.

1.3.1. Magnetic Stripe Order and the J_1-J_2 Ising Model. Many materials feature modulated charge or spin order, i.e., charge and spin density waves (or 'stripes'). Such stripe order can be seen for example in iron pnictides and cuprate superconductors.

A prototypical model to study the formation of a stripe phase is the $J_1 - J_2$ two-dimensional Ising model. The Hamiltonian reads:

$$H_0 = -J_1 \sum_{\langle ij \rangle} S_i S_j - J_2 \sum_{\langle\langle ij \rangle\rangle} S_i S_j \ , \tag{1.28}$$

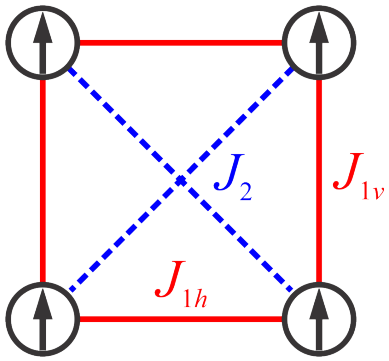

Figure 1.5. Interactions of the anisotropic $J_1 - J_2$ model

where $S_i = \pm 1$ are classical Ising variables, and $J_1 > 0$ and $J_2 < 0$ are the nearest-neighbor and second-neareast neighbor interactions respectively (see Figure 1.5). In the absence of vacancies, the phase transitions of the system are well studied (see, e.g., Refs. [29, 30, 31, 32]). If the ratio $|J_2|/J_1 < 1/2$, the ground state of the system will be ferromagnetic. It doesn't break any real-space symmetry. But if the ratio $|J_2|/J_1 > 1/2$, the ground states breakes the C_4 rotation symmetry of the lattice and will result in stripe phase. Figure 1.6 shows the existence of the stripe phase in the phase diagram of the undiluted system.

How do spinless impurities affect the phase diagram of the $J_1 - J_2$ Ising model? If the system is in the ferrormagnetic phase ($|J_2|/J_1 < 1/2$), spinless impurities do not break the order-parameter symmetry (the spin up-down symmetry). They therefore act as random-T_C disorder.

As the stripe order that occurs for $|J_2|/J_1 > 1/2$ breaks a real-space symmetry (the C_4 lattice rotation symmetry), the impurities are expected to create random-field disorder. The explicit random-field mechanism was analyzed in [33], where it was shown that horizontal vacancy pairs favor horizontal stripes and vertical vacancy pairs favor vertical stripes by an energy differenct of $2J_1$ (see Figure 1.7).

The resulting random-field disorder destroys the long-range stripe-ordered phase via domain formation [33], as predicted by the Imry-Ma argument.

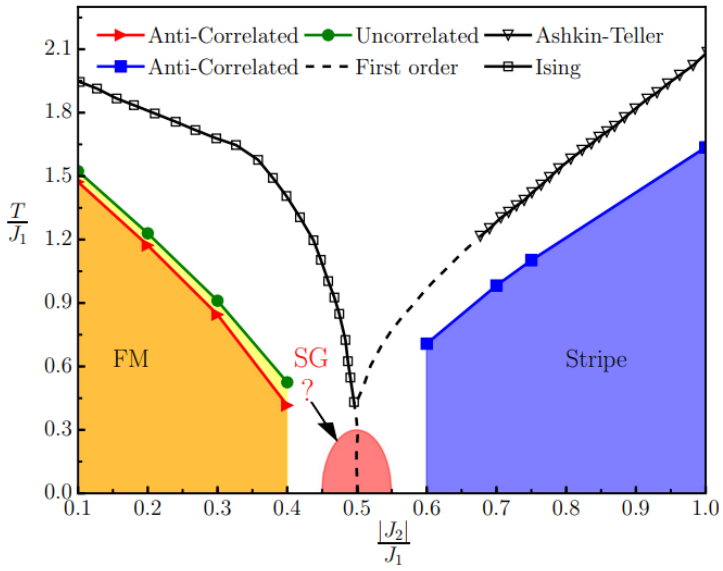

Figure 1.6. Phase diagram of $J_1 - J_2$ Hamiltonian for both uncorrelated and anticorrelated site dilution at an impurity concentration of $p = 1/8$ compared to the phase diagram of the undiluted system (open symbols)

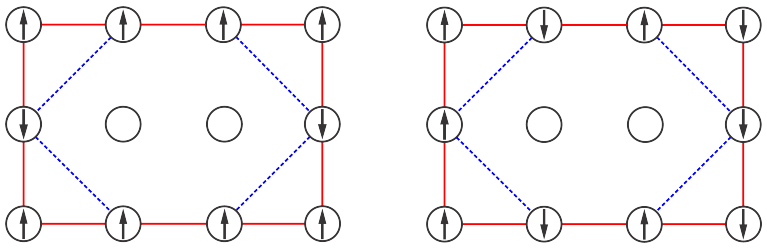

Figure 1.7. Random field mechanism in diluted $J_1 - J_2$ model. The energy of the horizontal stripe state(left) is lower by $2J_1$ than the energy of the vertical stripe state(right).

In paper I, we analyze the effects of an additional weak interaction anisotropy, introduced, for example, by strain on the sample.

1.3.2. Nonequilibrium Phase Transitions in the Contact Process. In the previous sections, phase transitions in equilibrium systems were studied. However, research has shown that abrupt transitions can also occur between different nonequilibium steady states [34].

One example is the *contact process* introduced by Harris [35, 36] as a prototypical model that undergoes a noneequilibrium continuous phase transition. The model is defined on a hypercubic lattice in d dimension. Each site can be occupied by a particle (active) or it can be empty (inactive). The time evolution of the contact process is a continuous-time *Markov process*, and it contains 2 basic trasitions.

(i) Active site spontaneously becomes inactive with a 'healing' rate μ, this 'healing' rate μ is usually set to unity for simplification.

(ii) Inactive sites get 'infected' at rate $n\lambda/2d$ where n is the number of active nearest neighbor sites, and λ is called the infection rate.

The infection rate λ is the overall control parameter and determines the fate of the contact process. For sufficiently small λ, the healing process dominates the state of the system. Eventually all active sites will die out, resulting in an *inactive state*. This state is called an absorbing state because the system cannot leave this state. For sufficiently large λ, the infection process dominates the state, the fraction of active sites is nonzero at all times, resulting in the *active state*. The nonequilibrium phase transition between the inactive and active states occurs at a critical value of the infection rate λ_C.

Now we disscuss the critical phenomena of the contact process. Near the critical point, the density of active sites in the steady state ρ_s shows a power-law denpendence on the distance from criticality $r \sim (\lambda - \lambda_C)$:

$$\rho_s \sim r^{\beta}. \tag{1.29}$$

where β is the order parameter critical exponent. The characterstic size of clusters of active sites, the correlation length ξ, also follows a power-law dependence on r:

$$\xi \sim |r|^{\nu_\perp}. \tag{1.30}$$

where ν is the correlation length critical exponent. The corresponding time scale, the correlation time τ follows the relation

$$\tau \sim \xi^z. \tag{1.31}$$

where z is the dynamical critical exponent.

These three exponents β, ν, z define the universality class of the transition which is known as the directed percolation universality class. In one dimension, they take the values $\beta = 0.276486$, $\nu_\perp = 1.733847$, $z = 1.580745$.

Paper II is devoted to the effects of simultaneous spatial and temporal disorder on the transition of the contact process.

1.4. JOSEPHSON JUNCTION

The Josephson effect is a quantum mechanical phenomenon that allows supercurrents to go through a thin non-superconducting barrier or restriction between two superconductors. A device that can present this phenomenon and produce supercurrent is called Josephson junction. This was predicted by B. D. Josephson in 1962 [37] and experimentally confirmed shortly after.

This barrier separating two superconductors can be an insulator, creating a S-I-S junction, or a non-superconducting metal, creating a S-N-S junction, or a physical constriction that weakens the contact point, creating a S-c-S junction. If a Josephson junction is on the surfaces of a 3D topological insulator, a topological superconductor can be achieved through proximity induced superconductivity [38, 39, 40, 41, 42, 43, 44, 45, 46, 47].

The DC Josephson effect is a direct current crossing the insulator without external electromagnetic field. The supercurrent depends on the phase difference ϕ between two superconducting electrodes. The supercurrent density through tunneljunction is:

$$J = J_c \sin \phi. \tag{1.32}$$

where J_c is the maximum supercurrent that can flow through the Josephson junction, and $\phi = \phi_1 - \phi_2$ is the phase difference of the macroscopic quantum phases of the superconductors.

The AC Josephson effect, on the other hand, serves as a voltage standard, with the phase varying linearly with time and current being a sinusoidal AC with time. A second explanation possible for AC Josephson effect is that the tunneling Cooper pairs are accelerated due to the presence of the voltage and gain energy. As the cooper pairs are not allowed to alter their energy while tunneling, a photon is emitted.

The Josephson effect is an example of a macroscopic quantum phenomenon, which manifests itself in various quantum implications such as superconducting quantum interference devices (SQUIDs) or superconducting qubits.

1.4.1. Topological Insulator. A topological insulator is a material that behaves as an insulator in the bulk phase, but the surface or edge can contain conducting states. These states are possible due to the combination of spin-orbit interactions and time-reversal symmetry. The topological insulator is closely related to the 2D integer quantum Hall state, which also has unique edge states. The surface or edge states of a topological insulator features conduncting states which are unlike any other known 1D or 2D electronics systems [48].

As shown in Figure 1.8, inside the topological insulator, its Fermi level lies between conducting band and valence band, so it behaves as normal insulator. Yet on the surface, there exist symmetry-protected Dirac fermions. These states can fall within the bulk energy gap and allow surface metallic conduction [50].

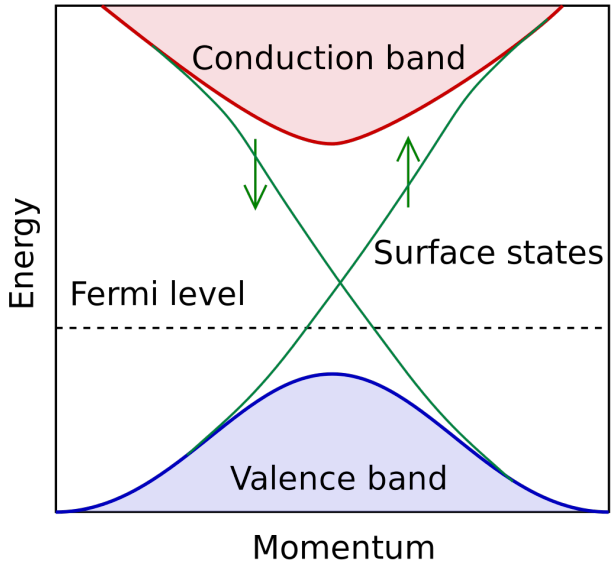

Figure 1.8. Energy band of topological insulator [49]

Topological insulators have non-trivial symmetry-protected topological order, the distinction between 2D and 3D topological insulators is determined by the Z_2 topological invariant that defines the ground s tate. If there is a single Z_2 invariant distinguishing the insulator from the quantum spin-Hall phase, it is in 2D. If there are four Z_2 invariant distinguishing the insulator, it is in 3D.

Being also one of the topics of this dissertation, three-dimensional topological insulators have drawn a great deal of attention due to their conducting 2D helical surface states protected by time reversal symmetry and strong spin-orbit coupling. These protected surface states are immune to magnetic disorder and localization effects; therefore transport through them is expected to be dissipationless [51, 52].

Proximity-induced superconductivity in topologically non-trivial surface states of a 3D topological insulator is predicted to give rise to an exotic quantum phenomenon called fractional Josephson effect. Although existent 3D topological insulators are not perfect insulators in the bulk, it has been demonstrated theoretically [53] and experimentally [42, 44] that the supercurrent primarily flows through the surface states rather than the bulk in a topologcial Josephson junction. Since surface states of the topological barrier are symmetry

protected from backscattering, the system can possess gapless bound states as in the case of SNS junction with perfectly transparent SN contacts (N denotes normal metal, S denotes superconductor). In the non-adiabatic limit, a special pair of bound states crosses at $\phi = \pi$ (bringing a continuum of gapless states at zero energy) due to fermion parity conservation [54]. This leads to a doubling in the periodicity of a conventional SNS Josephson relation, i.e. fractional Josephson effect.

1.4.2. Topological Kondo Insulator. Topological Kondo insulators are a class of narrow gap topologically ordered insulators. This topological order comes from the large spin orbit coupling and the odd-parity of the f-states. At room temperature, these insulators are metals containing magnetic moments; at sufficiently low temperatures, Kondo hybridization of localized f-electrons with itinerant d-electrons in the conduction band opens up a narrow insulating band gap where the Fermi level lies [55].

One of the biggest drawbacks of commonly studied 3D topological insulators is the presence of conducting bulk that obscures both surface states and low energy bound sates. Kondo insulators are materials with strongly correlated electrons that open up a narrow band gap at low temperatures. The band gap opens up at low temperatures due to hybridization of localized electrons. Thus, the material will become insulating at low temperatures. As a result, topological Kondo insulators such as SmB_6 have a truely insulating bulk at low temperatures [56, 57]. Introducing superconductivity in topological Kondo insulators is therefore a promising avenue.

1.4.3. Shaphiro Steps. If a Josephson junction is exposed to microwave photons of frequency f, it undergoes an inverse AC Josephson effect; consequently the dc current-voltage characteristics will display quantized features, called Shaphiro steps [58, 59]. Shapiro steps will appear from the response of the supercurrents at voltages equal to $nhf/2e$. Here, h is Planck's constant, e is the electron charge, and n is an aribitary interger. This phenomena is also known as phase-locking effect since the Shaphiro steps occur due to the phase matching between the junction and the drive frequency.

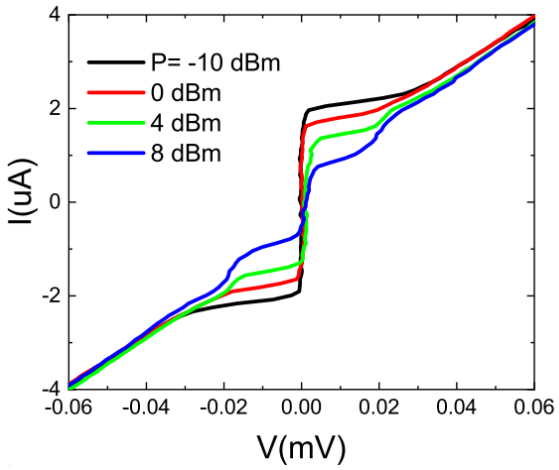

Figure 1.9. AC Josephson effect giving rise to Shaphiro steps in I-V

Figure 1.9 shows clear Shaphiro steps manifesting AC Josephson effect in the current-voltage characteristics of a $Nb/SmB_6/Nb$ Josephson junction The details about the fabrication and the performance of such devices will be explained in paper III.

PAPER

I. STRIPE ORDER, IMPURITIES, AND SYMMETRY BREAKING IN A DILUTED FRUSTRATED MAGNET

Xuecheng Ye

Department of Physics, Missouri University of Science and Technology, Rolla, MO 65409, USA

Rajesh Narayanan

Department of Physics, Indian Institute of Technology Madras, Chennai 600036, India

Thomas Vojta

Department of Physics, Missouri University of Science and Technology, Rolla, MO 65409, USA

ABSTRACT

We investigate the behavior of the frustrated J_1-J_2 Ising model on a square lattice under the influence of random dilution and spatial anisotropies. Spinless impurities generate a random-field type disorder for the spin-density wave (stripe) order parameter. These random fields destroy the long-range stripe order in the case of spatially isotropic interactions. Combining symmetry arguments, percolation theory and large-scale Monte Carlo simulations, we demonstrate that arbitrarily weak spatial interaction anisotropies restore the stripe phase. More specifically, the transition temperature T_c into the stripe phase depends on the interaction anisotropy ΔJ via $T_c \sim 1/|\ln(\Delta J)|$ for small ΔJ. This logarithmic dependence implies that very weak anisotropies are sufficient to restore the transition

temperature to values comparable to that of the undiluted system. We analyze the critical behavior of the emerging transition and find it to belong to the disordered two-dimensional Ising universality class, which features the clean Ising critical exponents and universal logarithmic corrections. We also discuss the generality of our results and their consequences for experiments.

1. INTRODUCTION

The influence of impurities, defects, and other types of quenched random disorder on the symmetry-broken low-temperature phases of many-particle systems and on their phase transitions is an important topic in condensed matter physics. Fundamentally, disorder effects are governed by the interplay between the symmetries of the order parameters characterizing the phase or phase transition and the symmetries of the disorder (see, e.g., Ref. [1] for a pedagogical discussion).

If the impurities respect the order parameter symmetries, they generically lead to random-T_c disorder, i.e., to spatial variations in the tendency towards the symmetry-broken phase. As this disorder appears in the mass term of the order parameter field theory, it is also called random-mass disorder. The diluted ferromagnet is an example for this case because spinless impurities do not prefer a particular magnetization direction and thus do not break the spin symmetry. Random-mass disorder can influence phase transitions profoundly, e.g., by rounding first-order phase transitions [2, 3, 4] or by modifying the critical behavior of continuous ones [5]. Quantum phase transitions can feature additional disorder effects including infinite-randomness critical points [6, 7, 8, 9, 10], smeared phase transitions [11, 12], and quantum Griffiths singularities [13, 14, 15, 16] (see Refs. [17, 18, 19] for reviews).

If, on the other hand, the impurities locally break the order parameter symmetries, a stronger coupling between the disorder and the order parameter can be expected. The generic result is random-field disorder [20], i.e., randomness in the field conjugate to

the order parameter in the corresponding field theory. More complicated scenarios such as random-easy-axis disorder [21] can occur if the impurities break the order parameter symmetries only partially. Random fields can have more dramatic effects than random-mass disorder. In sufficiently low space dimensions ($d \leq 2$ for discrete order parameter symmetry and $d \leq 4$ for continuous order parameter symmetry), even weak random fields destroy the symmetry-broken phase itself via domain formation [4, 20, 22].

Recent years have seen renewed interest in phases that spontaneously break real-space symmetries in addition to spin, phase, or gauge symmetries, including the charge-density wave or stripe phases in cuprate superconductors [23, 24, 25], the Ising-nematic phases in the iron pnictides [26, 27, 28], as well as valence-bond solids in certain quantum magnets [29, 30, 31]. In general, impurities locally break the real-space symmetries of the associated order parameters. They thus generically lead to random-field type disorder for such order parameters [32, 33, 34, 35, 36, 37, 38, 39]. In addition to destroying the original long-range order, these random fields can also induced novel phases of matter [38, 39].

A prototypical model for impurity-induced random fields is the frustrated J_1-J_2 Ising model on a square lattice, with ferromagnetic nearest-neighbor interactions and antiferromagnetic next-nearest-neighbor interactions. For sufficiently strong next-nearest-neighbor interactions, it features a stripe-ordered low-temperature phase. As site or bond dilution locally break the symmetry between the two equivalent stripe directions, they generate random fields for the nematic order [32, 37] which destroy the stripe phase via domain formation. Interestingly, the strength of the random fields can be tuned by the repulsion between the impurities [37].

In the present paper, we revisit the diluted J_1-J_2 Ising model and focus on the interplay between the random-field disorder and global interaction anisotropies that may arise, e.g., from strain engineering, epitaxial growth or the shape of crystallites or samples. We combine symmetry arguments, percolation theory and large-scale Monte Carlo simulations to show that the stripe phase is restored by an arbitrarily weak global anisotropy

(modeled, e.g., by a difference ΔJ between the horizontal and vertical interaction strengths) that explicitly breaks the symmetry between the two stripe directions. Importantly, the transition temperature T_c into the stripe phase varies with the interaction anisotropy as $T_c \sim 1/|\ln(\Delta J)|$. This logarithmic dependence implies that a very weak anisotropy is sufficient to suppress most random-field effects and restore the transition temperature to a value comparable to that of the undiluted system. We also determine the critical behavior of the emerging phase transition between the paramagnetic and stripe phases. Just as the transition in the diluted Ising ferromagnet, it belongs to the disordered two-dimensional Ising universality class which is characterized by the clean Ising exponents and universal logarithmic corrections.

The remainder of our paper is organized as follows. In Sec. 2, we define the J_1-J_2 Ising model. We also discuss the random-field mechanism and domain formation. Our computer simulation methods are introduced in Sec. 3. Section 6 is devoted to the simulation results and a comparison with theoretical predictions. We conclude in Sec. 5 by discussing the generality of our findings and their consequences for experiments.

2. MODEL AND RANDOM-FIELD MECHANISM

2.1. DILUTED ANISOTROPIC J_1-J_2 ISING MODEL

We start with the well-known J_1-J_2 Ising model on a square lattice of $N = L^2$ sites given by the Hamiltonian

$$H_0 = -J_1 \sum_{\langle ij \rangle} S_i S_j - J_2 \sum_{\langle\langle ij \rangle\rangle} S_i S_j \ . \tag{1}$$

Here, $S_i = \pm 1$ is a classical Ising spin, $\langle ij \rangle$ denotes pairs of nearest-neighbor sites coupled by the ferromagnetic interaction $J_1 > 0$, and $\langle\langle ij \rangle\rangle$ denotes next-nearest neighbor pairs coupled by the antiferromagnetic interaction $J_2 < 0$. The phases of this system are well-understood

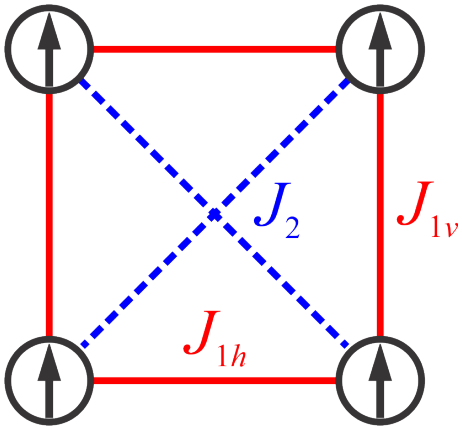

Figure 1. Interactions of the anisotropic J_1-J_2 model.

(see, e.g., Refs. [40, 41, 42, 43] and references therein). It displays paramagnetic behavior at high temperatures. As the temperature is lowered, two distinct long-range ordered phases appear. For $|J_2|/J_1 < 1/2$, the low-temperature phase is ferromagnetic; it breaks the Z_2 Ising spin symmetry but none of the real-space symmetries. For $|J_2|/J_1 > 1/2$, in contrast, the low-temperature phase features a stripe-like spin order that breaks not only the Ising spin symmetry but also the C_4 rotation symmetry of the square lattice.

To explore the combined influence of quenched disorder and spatial anisotropies on the stripe phase, we now introduce site dilution, and we allow the nearest-neighbor interaction to take different values J_{1h} and J_{1v} for horizontal and vertical bonds, respectively (see Fig. 1). The resulting Hamiltonian reads

$$\begin{aligned} H = \quad & -J_{1h} \sum_{\langle ij \rangle_h} \epsilon_i \epsilon_j S_i S_j - J_{1v} \sum_{\langle ij \rangle_v} \epsilon_i \epsilon_j S_i S_j \\ & -J_2 \sum_{\langle\langle ij \rangle\rangle} \epsilon_i \epsilon_j S_i S_j \ . \end{aligned} \tag{2}$$

The ϵ_i are quenched random variables that can take the values 0 (representing a vacancy) with probability p and 1 (occupied site) with probability $1-p$. We consider the ϵ_i at different sites statistically independent; the effects of (anti)correlations between the vacancies were

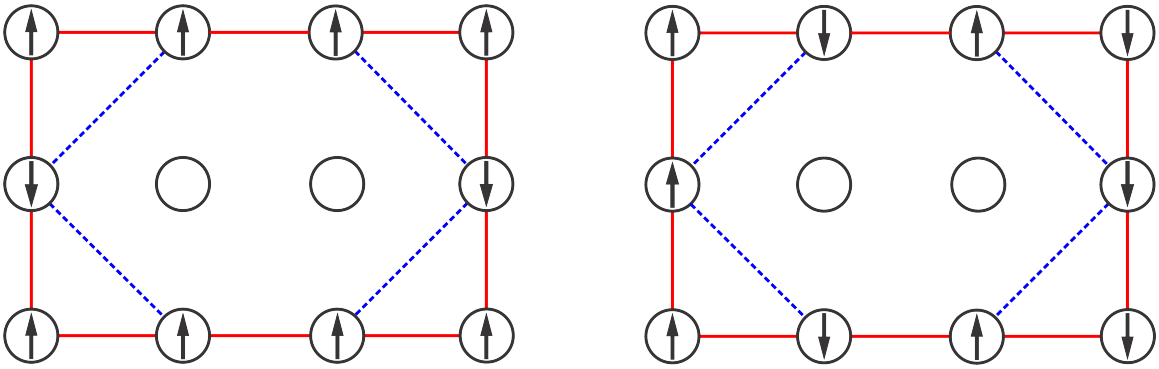

Figure 2. Random-field mechanism: A pair of vacancies on horizontal nearest-neighbor sites prefers horizontal stripes (left) over vertical stripes (right) by an energy difference of $2J_1$.

explored in Ref. [37]. We parameterize the nearest-neighbor interactions in terms of their average and difference, $J_{1h} = J_1 + \Delta J$, $J_{1v} = J_1 - \Delta J$. In the following, we focus on the parameter region that favors stripe order at low temperatures, i.e., on $|J_2|/J_1 > 1/2$.

2.2. RANDOM-FIELD DISORDER

While a single vacancy does not break the C_4 rotation symmetry of the lattice, spatial arrangements of several vacancies generally do break this symmetry locally, leading to the emergence of random-field disorder that locally prefers one stripe direction over the other (even in the absence of interaction anisotropies, i.e., for $\Delta J = 0$). Specifically, a pair of vacancies on horizontal nearest-neighbor sites prefers horizontal stripes over vertical stripes by an energy difference of $2J_1$, see Fig. 2 [32, 37]. Analogously, a vacancy pair on vertical nearest-neighbor sites prefers vertical stripes.

The typical random-field energy of a perfect (horizontal or vertical) stripe state in a system of $L \times L$ sites can be easily estimated in the limit of low dilution p when different vacancy pairs can be considered independent and arrangements of three or more vacancies on neighboring sites are suppressed. A system of $L \times L$ sites has $2L^2$ distinct nearest neighbor pairs (bonds), resulting in an average number of vacancy pairs of $2L^2p^2$. The

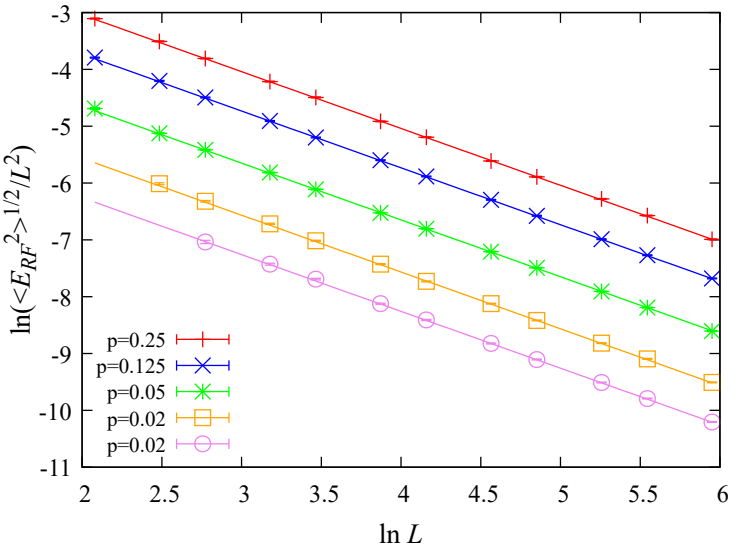

Figure 3. Root-mean-square random-field energy of a perfect stripe state per lattice site, $\langle E_{RF}^2 \rangle^{1/2}/L^2$, vs. linear system size L for several dilutions p. The data are determined by averaging the square of the energy difference between perfect horizontal and vertical stripe states over 20,000 disorder configurations. The solid lines represent relation (3) without adjustable parameters.

random-field energy $E_{RF}(L)$ is thus the sum of $2L^2p^2$ random contributions $\pm J_1$. The central limit theorem then gives

$$\langle E_{RF}^2(L) \rangle = 2L^2p^2J_1^2 = h_{\rm eff}^2 L^2 \tag{3}$$

with effective random field strength $h_{\rm eff} = \sqrt{2}pJ_1$ [1]. We have confirmed the relation (3) numerically for a range of dilutions and system sizes, as can be seen in Fig. 3. It holds (at least in very good approximation) for dilutions as high as $p = 1/4$.

[1]Note that the effective random-field strength is proportional to p rather than p^2 as one might have naively expected because the probability for finding a vacancy pair is proportional to p^2.

2.3. DOMAIN FORMATION

According to Imry and Ma [20], the fate of the symmetry-broken low-temperature phase is governed by the competition between the random-field energy gain due to the formation of domains of horizontal and vertical stripes that align with the local random field and the energy cost of a domain wall. The energy cost of a straight domain wall between horizontal and vertical stripes in the undiluted J_1-J_2 model is easily worked out, it equals $2J_2$ per lattice constant. This domain formation problem can be mapped onto a random-field Ising model with the Ising variable representing the difference between horizontal and vertical stripes in the J_1-J_2 model (2).

Let us first consider the case of isotropic interactions, $\Delta J = 0$ (which maps onto an unbiased random-field Ising model). In two dimensions, domains appear for arbitrarily weak random fields beyond the so-called breakup length scale L_0. For weak random fields, L_0 depends exponentially on the ratio between the domain wall energy scale J_2 and the random-field strength $h_{\rm eff}$,

$$L_0 = A \exp(cJ_2^2/h_{\rm eff}^2) \tag{4}$$

with A and c constants [22]. As horizontal and vertical stripe domains are equally likely for $\Delta J = 0$, the domain formation destroys the symmetry-broken low-temperature phase. (A rigorous proof that the Gibbs state in a two-dimensional random-field Ising model is unique was given by Aizenman and Wehr [4].) This agrees with the Monte Carlo simulation results of Ref. [37].

For anisotropic interactions, $\Delta J \neq 0$, the problem maps onto a biased random-field Ising model. In the case $\Delta J > 0$, horizontal stripes are preferred over vertical ones. Minority (vertical stripe) domains have a finite maximum size that decreases with increasing ΔJ [22]. At low temperatures, we thus expect the system to consist of finite-size vertical-stripe domains embedded in the bulk featuring horizontal stripes.

The domains of the two-dimensional random-field Ising model were further investigated by Seppälä et al. [44, 45] and by Stevenson and Weigel [46, 47]. They demonstrated that the domain structure in the unbiased case on length scales larger than L_0 resembles the fractal cluster structure of a critical percolation problem, at least for sufficiently weak random fields (i.e., sufficiently large L_0). Increasing bias ($\Delta J > 0$) drives the domain pattern away from percolation criticality, and a massive spanning cluster of the majority stripes forms. This transition in the domain structure is governed by the usual two-dimensional classical percolation exponents.

2.4. MAGNETIC PHASE TRANSITION

The random-field disorder in the diluted J_1-J_2 model locally breaks the C_4 rotation symmetry of the square lattice. However, it does not break the Z_2 Ising spin symmetry. This leaves open the possibility of a magnetic phase transition into a long-range ordered low-temperature phase that spontaneously breaks this remaining Z_2 symmetry [2]. This phase transition, if any, has to occur on the background of the stripe domain pattern discussed in Sec. 2.3.

In the absence of a global anisotropy (i.e., for $\Delta J = 0$), the magnetic phase transition is impossible because the domain structure resembles critical percolation. This implies that neither horizontal nor vertical domains form a massive cluster that covers a finite fraction of the lattice sites and can support long-range magnetic order. This conclusion agrees with the Monte Carlo results of Ref. [37].

In the presence of a global anisotropy, in contrast, the majority stripes (horizontal stripes for $\Delta J > 0$) form a massive infinite (spanning) cluster. The Ising spins on this cluster can therefore spontaneously break the Z_2 Ising symmetry and develop long-range order. To estimate the critical temperature T_c of the magnetic transition as function of the global

[2] Note that situation differs from the random-field Ising model where the random fields completely break the order parameter symmetry.

anisotropy ΔJ, we recall that the critical temperature of a diluted Ising model close to the percolation threshold p_c varies as $T_c \sim 1/|\ln(p - p_c)|$ with the distance $p - p_c$ from the threshold (see, e.g., [48, 49]). In our J_1-J_2 model (2), the distance of the stripe domain pattern from percolation criticality is controlled by ΔJ. We therefore expect the transition temperature into the stripe phase to vary as

$$T_c \sim 1/|\ln(\text{const}\,\Delta J)| \,. \tag{5}$$

In addition to random-field disorder, the vacancies also create random-mass disorder which is known to prevent first-order phase transitions in two dimensions [2, 3, 4]. We thus expect the transition into the stripe phase to be continuous. On symmetry grounds, its critical behavior should belong to the two-dimensional disordered Ising universality class as it spontaneously breaks the remaining Z_2 symmetry. This is a particularly interesting universality class because the clean two-dimensional Ising correlation length exponent takes the value $\nu = 1$ which makes it marginal with respect to the Harris criterion [5] $d\nu > 2$. Perturbative renormalization-group studies [50, 51, 52] predict that the critical behavior of the disordered Ising model is controlled by the clean Ising fixed point. Disorder, which is a marginally irrelevant operator, gives rise to universal logarithmic corrections to scaling. Early computer simulations [53, 54, 55], in contrast, found nonuniversal critical exponents that vary continuously with disorder strength. More recent large-scale simulations strongly support the logarithmic-corrections scenario (see Ref. [56] and references therein).

3. MONTE CARLO SIMULATIONS

In order to gain a quantitative understanding of the interplay between the random fields and the global anisotropy in the J_1-J_2 model, we perform extensive Monte Carlo simulations of the Hamiltonian (2). As we are interested in the fate of the stripe low-temperature phase, we fix the interaction energies at the values $J_1 = J_2 = 1$ for which the

undiluted isotropic system enters the stripe phase at a temperature of about 2.08 [42]. The dilution is fixed at $p = 0.25$. This relatively strong disorder leads to moderate domain sizes that actually fit into the sample sizes we are able to simulate. The global interaction anisotropy ΔJ is varied between 0 and 0.2.

In the parameter region $J_1 > 0, J_2 < 0$, the interactions of the J_1-J_2 model are frustrated. Therefore, cluster algorithms such as the Wolff [57] and Swendsen-Wang [58] algorithms do not improve the efficiency of the simulations [59]. We therefore combine conventional single-spin-flip Metropolis updates [60] with "corner" updates that exchange the two spins on the diagonal corners of a 2×2 plaquette of sites. These corner updates locally turn horizontal stripes into vertical ones and vice versa. Specifically, a full Monte Carlo sweep consists of a Metropolis sweep over the full lattice followed by two corner sweeps (one attempting to exchange the top right and bottom left sites of each plaquette, the other doing the same for the top left and bottom right sites).

As both Monte Carlo moves are local, equilibration is slow, and the problem is further exacerbated by the random-field effects at nonzero dilution. This is illustrated in Fig. 4 which shows how the energy approaches its equilibrium value (for a prototypical set of parameters). The data demonstrate that the relaxation is slower than exponential, it approximately follows a power law over at least two orders of magnitude in Monte Carlo time.

Consequently, long equilibration periods are required in the simulations, as well as long measurement periods to ensure that the measurements do not remain correlated over the simulation run. This severely limits the system sizes we can study. We employ equilibration periods ranging from 30,000 full sweeps for the smallest systems (linear size $L = 16$) to 10^6 sweeps for the largest systems studied ($L = 192$). The corresponding measurement periods range from 30,000 to 2×10^6 full sweeps, with a measurement taken after each sweep. We also change the temperature in small steps and use the final spin configuration for one temperature as the initial configuration for the next. To check whether the observables truly

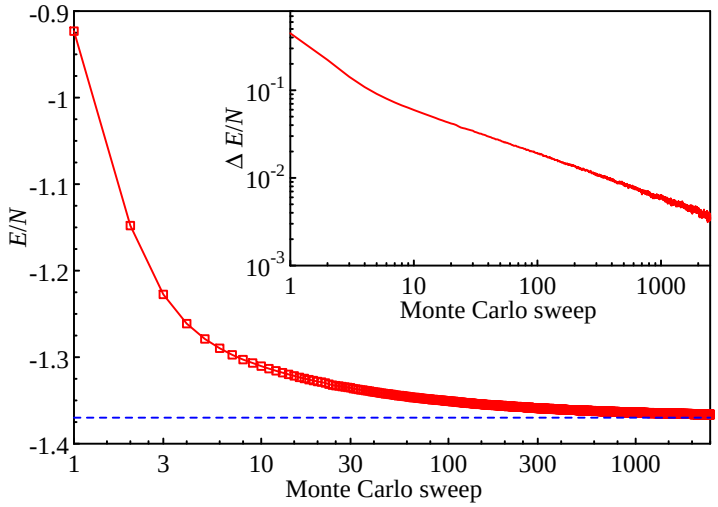

Figure 4. Energy per site E/N vs. Monte Carlo sweep for a system of linear size $L = 96$, $\Delta J = 0$ and temperature $T = 1.15$. The data are averages over 3000 runs, each with a different disorder configuration. The simulations start from a random configuration of spins (hot start). The dashed line marks the equilibrium value of E/N. Inset: Log-log plot of the deviation ΔE from the equilibrium value vs. Monte Carlo sweep.

reach their equilibrium values (within the statistical errors), we compare the results of runs with "hot" starts (spins have independent random values initially) and "cold" starts (spins are in perfect stripe state initially). An example of such a comparison is shown in Fig. 5. All data are averaged over 3,000 to 100,000 disorder (vacancy) configurations, depending on system size and temperature range.

During the simulations, we compute a number of observables including the total energy per site $[\langle e\rangle]_{\rm dis}$ and the specific heat $C = (N/T^2)[\langle e^2\rangle - \langle e\rangle^2]_{\rm dis}$. Here, $e = E/N$ stands for an individual energy measurement, $\langle \ldots \rangle$ is the canonical thermodynamic average (which is approximated by the Monte Carlo average) and $[\ldots]_{\rm dis}$ is the average over the disorder configurations. We also calculate the two-component stripe order parameter $\psi = (\psi_h, \psi_v)$ with

$$\psi_h = \frac{1}{N}\sum_i (-1)^{y_i}\epsilon_i S_i \ , \quad \psi_v = \frac{1}{N}\sum_i (-1)^{x_i}\epsilon_i S_i \ . \tag{6}$$

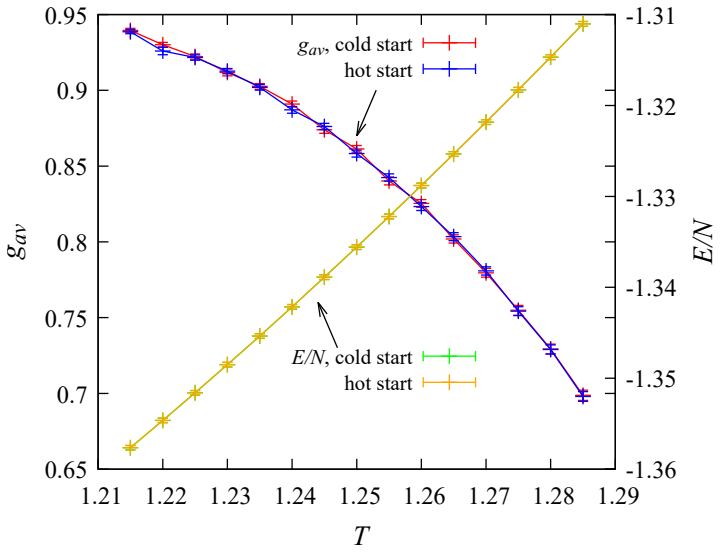

Figure 5. Comparison of simulations with hot starts (random initial spin configuration, run starts at highest temperature) and cold starts (spins initially in perfect stripe state, run starts at lowest temperature). Shown are the average Binder cumulant $g_{\rm av}$ and the total energy per site E/N as function of temperature T for a system with $L = 96$, $\Delta J = 0.01$. The data are averages over 5000 runs, each with a different disorder configuration, using 3×10^5 equilibration sweeps and 4×10^5 measurement sweeps.

Here, the indices h and v denote horizontal and vertical stripe order, respectively, and x_i and y_i are the (integer) coordinates of site i. The corresponding stripe susceptibility reads $\chi_s = (N/T)[\langle|\psi|^2\rangle - \langle|\psi|\rangle^2]_{\rm dis}$. Dimensionless observables are particularly useful for finding the phase transition temperature and analyzing the critical behavior. We therefore also determine the average and global Binder cumulants

$$g_{\rm av} = \left[2 - \frac{\langle|\psi|^4\rangle}{\langle|\psi|^2\rangle^2}\right]_{\rm dis}, \quad g_{\rm gl} = 2 - \frac{[\langle|\psi|^4\rangle]_{\rm dis}}{[\langle|\psi|^2\rangle]^2_{\rm dis}} \tag{7}$$

With increasing system size, these Binder cumulants are expected to approach the values 0 in the disordered phase and 1 in the stripe-ordered phase, and curves of the Binder cumulants vs. temperature for different system sizes cross at the phase transition temperature. $g_{\rm av}$ and $g_{\rm gl}$ capture similar information and are expected to have identical scaling behaviors, but they differ in how the disorder average is performed. For the average Binder cumulant $g_{\rm av}$, an

individual Binder cumulant is computed for each disorder configuration. These individual values are then averaged to yield g_{av}. To obtain the global Binder cumulant g_{gl}, in contrast, the second and fourth moment of the stripe order parameter are averaged over the disorder configurations, and the cumulant is then constructed from these disorder-averaged values.

4. RESULTS

4.1. ISOTROPIC INTERACTIONS, $\Delta J = 0$

To test our simulation and data analysis techniques, we first consider $\Delta J = 0$, i.e., equal exchange interactions J_{1h} and J_{1v} in the horizontal and vertical directions, respectively. This case can be compared with Ref. [37] and serves as the reference case for studying the effects of anisotropic interactions.

Figure 6 presents the Monte Carlo simulation results for the average stripe Binder cumulant g_{av} as a function of temperature T for several system sizes L at dilution $p = 1/4$ and $J_1 = J_2 = 1$. The curves for different L do not cross, instead g_{av} approaches zero with increasing L. The global Binder cumulant g_{gl} behaves analogously. This implies that there is no phase transition, and the system does not enter a long-range ordered stripe phase. This agrees with the expectation of domain formation according to the Imry-Ma argument discussed in Sec. 2.3 and with the results of Ref. [37].

The domains can be seen explicitly in a snapshot of the local nematic order parameter η_i in Fig. 7. It is defined via a sum over all bonds from site i to its nearest neighbors, $\eta_i = \sum_j' \epsilon_i \epsilon_j S_i S_j f_{ij}$ where $f_{ij} = 1$ for horizontal bonds and -1 for vertical bonds. (This means that $\eta_i = 4$ for perfect horizontal stripe order and -4 for perfect vertical stripe order.)

The figure indicates that horizontal and vertical stripes are equally likely for $\Delta J = 0$, as expected in the isotropic case. It also suggests a breakup length L_0 in the range between about 50 and 100 lattice constants. It is interesting to compare this estimate with the random-field Ising model result (4). Using the values $A \approx 6.1$ and $c \approx 1.9$ found numerically by

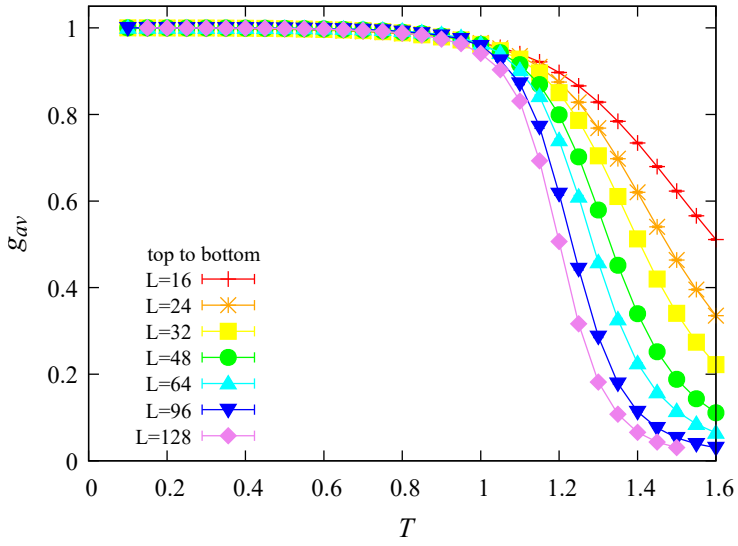

Figure 6. Average Binder cumulant $g_{\rm av}$ vs. temperature T for isotropic interactions $\Delta J = 0$ and several system sizes L. $p = 1/4$, $J_1 = J_2 = 1$. The data are averages over 3000 to 5000 disorder configurations. The resulting statistical errors are smaller than the symbol size.

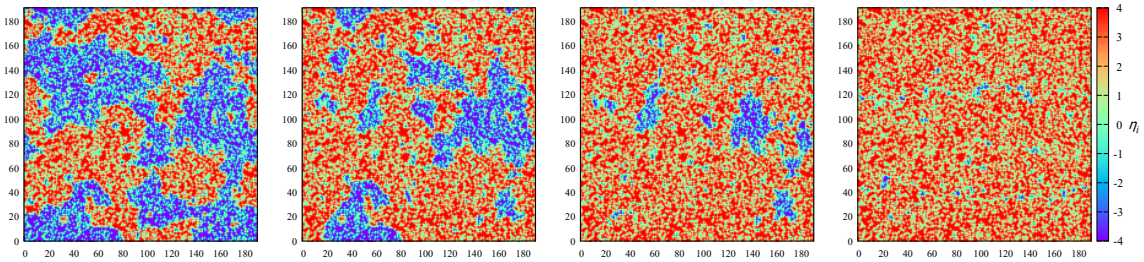

Figure 7. Snapshots of the local nematic order parameter η_i of one particular disorder configuration for several anisotropies: $\Delta J = 0$, 0.002, 0.01, 0.05 (left to right). The data are taken a temperature $T = 0.1$ reached via simulated annealing from high temperatures. $L = 192$, $p = 1/4$, $J_1 = J_2 = 1$.

Seppälä et al. [44, 45], eq. (4) yields a breakup length of about 2×10^7 for $p = 1/4$, much larger than the length identified in Fig. 7. We believe that this stems from the fact that the domain wall energy in the diluted system is significantly smaller than the value $2J_2$ per unit cell in the undiluted system because the domain wall can make use of the vacancies to reduce the number of unfulfilled bonds. In fact, assuming that the vacancies reduce the domain wall energy by a factor of 2 to 3, eq. (4) yields breakup length values comparable to the sizes seen in Fig. 7.

Thus, the vacancies play a complex role in the destruction of the stripe order: They generate random fields, they renormalize the domain wall energy, and they create random-mass disorder.

4.2. ANISOTROPIC INTERACTIONS, $\Delta J > 0$

We now turn to the main topic of this manuscript, the effects of a weak global interaction anisotropy ΔJ. To this end, we perform Monte Carlo simulations for $\Delta J = 0.002$, 0.005, 0.01, 0.02, 0.05, 0.1, and 0.2. Snapshots of the resulting local nematic order parameter η_i at low temperatures are presented in Fig. 7 for a few characteristic ΔJ values. As expected from the discussion in Sec. 2.3, the snapshots show that horizontal stripes proliferate with increasing ΔJ and form an infinite spanning cluster while vertical stripes are restricted to finite-size clusters. Already at $\Delta J = 0.05$, vertical stripe domains have essentially vanished.

To investigate whether or not the systems feature a phase transition into a long-range ordered stripe phase, we analyze the average Binder cumulant $g_{\rm av}$. For all $\Delta J \geq 0.005$, we find that the stripe Binder cumulant curves for different system sizes L cross at a nonzero temperature, indicating the existence of the phase transition. Examples of the average Binder cumulant data are presented in Figs. 8 and 9. The global Binder cumulant behaves analogously. The curves for $\Delta J = 0.2$ (Fig. 8) display a nearly perfect crossing for all considered system sizes, demonstrating that corrections to scaling are weak. For

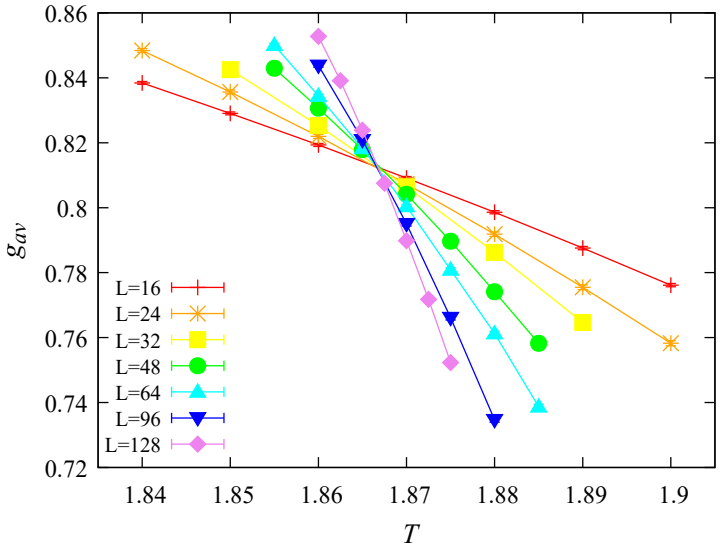

Figure 8. Average Binder cumulant $g_{\rm av}$ vs. temperature T for anisotropic interactions with $\Delta J = 0.2$ and several system sizes L. $p = 1/4$, $J_1 = J_2 = 1$. The data are averages over 30,000 to 100,000 disorder configurations. The resulting statistical errors are much smaller than the symbol size.

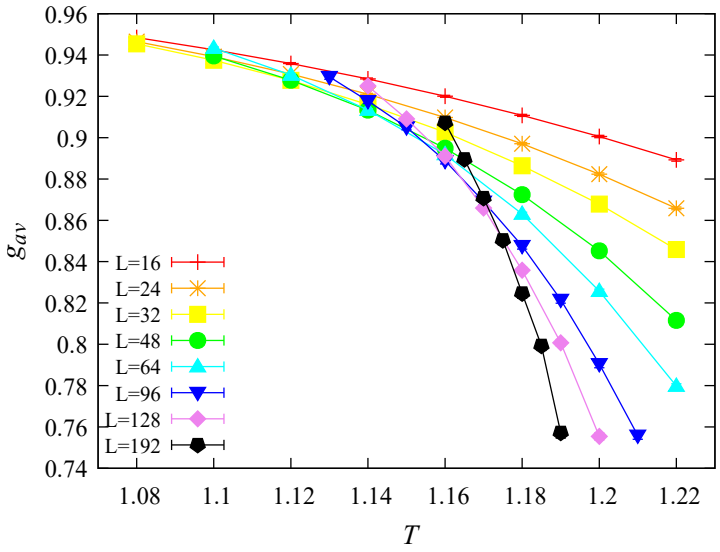

Figure 9. Average Binder cumulant $g_{\rm av}$ vs. temperature T for anisotropic interactions with $\Delta J = 0.005$ and several system sizes L. $p = 1/4$, $J_1 = J_2 = 1$. The data are averages over 10,000 to 20,000 disorder configurations. The statistical errors are smaller than the symbol size.

$\Delta J = 0.005$ (Fig. 9), in contrast, the curves for smaller system sizes ($L < 64$) do not cross and resemble the isotropic $\Delta J = 0$ case. The curves for larger systems cross but the crossing temperature of consecutive curves shifts systematically to higher values with increasing L. This indicates that the data for the studied system sizes have not quite reached the asymptotic critical regime.

The fact that the Binder cumulant curves for smaller sizes do not cross for weak anisotropy is readily understood by comparing the random field energy at a given system size with the energy gain for horizontal stripes due to ΔJ. According to eq. (3), the typical energy gain due to aligning a domain of size L with the local random fields is $h_{\rm eff} L = \sqrt{2} p J_1 L$ whereas the anisotropy favors horizontal stripes by the energy $\Delta J L^2$. A weak anisotropy can thus only suppress vertical domains of sizes larger than $L_{\Delta J} \approx \sqrt{2} p J_1 / \Delta J$ [3]. For $\Delta J = 0.005$, this estimate gives $L_{\Delta J} \approx 70$ in agreement with the observation that crossings start to appear for $L \geq 64$. For $\Delta J = 0.002$, the smallest domain that the anisotropy can flip has a size of about $L \approx 175$. As our system sizes are restricted to $L \leq 192$, this explains why we do not observe clear crossings of the Binder cumulant curves for $\Delta J = 0.002$. In other words, identifying the phase transition for $\Delta J \leq 0.002$ requires simulations of significantly larger systems.

We now analyze how the transition temperature T_c into the stripe-ordered phase varies with the interaction anisotropy ΔJ. To this end, we determine the crossing temperature for each ΔJ value. This is unambiguous for the larger ΔJ for which the crossing is "sharp", i.e., the curves all cross at the same temperature within their statistical errors. For the smaller ΔJ, where the crossing shifts with increasing L, we estimate T_c from the crossing of the largest two system sizes [4].

Figure 10 presents the resulting dependence of T_c on ΔJ. The data show that T_c

[3] Note that is a very rough estimate as it assumes compact domains which only holds on scales below L_0. On larger length scales the cluster structure is fractal, see Sec. 2.3.

[4] A systematic extrapolation of the crossing temperature to infinite system size, as performed, e.g., in Ref. [56], would require significantly lower statistical errors and is thus beyond our current computational capabilities.

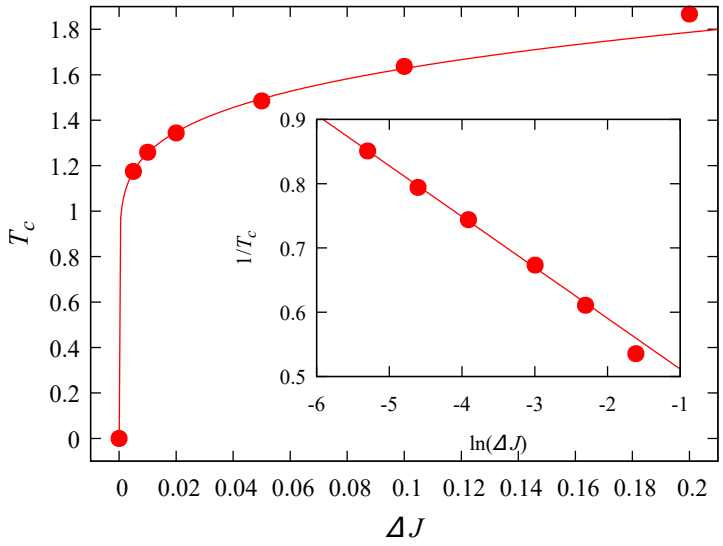

Figure 10. Transition temperature T_c into the long-range stripe ordered phase vs. interaction anisotropy ΔJ for $p = 1/4$, $J_1 = J_2 = 1$. The solid line is a fit of the data for $\Delta J < 0.2$ to the logarithmic dependence (5). Inset: Data replotted as $1/T_c$ vs. $\ln \Delta J$ such that (5) leads to a straight line.

rises very rapidly as ΔJ increases from zero implying that a small global anisotropy is sufficient to stabilize a robust stripe phase. The figure also demonstrates that T_c follows the logarithmic dependence (5) on ΔJ predicted in Sec. 2.4 for all $\Delta J \leq 0.1$.

It is interesting to compare the critical temperatures in Fig. 10 with the corresponding value $T_{c0} \approx 2.08$ [42] for the undiluted isotropic system at the same parameter values ($J_1 = J_2 = 1$). Our simulations show that a weak anisotropy of $\Delta J = 0.005$ already produces a T_c of more than half of the undiluted value. Moreover, a large part of the reduction can be attributed to the random-mass effects of the dilution in our system and not the random-field physics. Thus, a better comparison may be the diluted system with anticorrelated impurities studied in Ref. [37]. In that system, the random-field physics is completely eliminated by the vacancy anticorrelations. Its critical temperature of $T_c \approx 1.17$ (for $p = 1/4$ and $J_1 = J_2 = 1$) is comparable to the critical temperatures in Fig. 10 for anisotropies ΔJ that have largely suppressed the effects of the random-field disorder.

4.3. CRITICAL BEHAVIOR

According to the discussion in Sec. 2.4, we expect the transition into the long-range stripe-ordered phase to be continuous and to belong to the two-dimensional disordered Ising universality class. A perturbative renormalization group approach [50, 51, 52] predicts its critical behavior to be controlled by the clean Ising fixed point while the disorder gives rise to universal logarithmic corrections to scaling. This leads to the following finite-size scaling behavior [61, 62, 63]. The specific heat at the critical temperature diverges as

$$C \sim \ln\ln L \tag{8}$$

with system size L. The order parameter and its susceptibility at T_c behave as

$$\psi \sim L^{-\beta/\nu}\left[1 + O(1/\ln L)\right], \tag{9}$$

$$\chi_s \sim L^{\gamma/\nu}\left[1 + O(1/\ln L)\right], \tag{10}$$

with $\beta/\nu = 1/8$ and $\gamma/\nu = 7/4$ as in the clean two-dimensional Ising model. Any quantity R of scale dimension zero (such as the Binder cumulants g_{av} and g_{gl}) and its temperature derivative scale as

$$R = R^* + O(1/\ln L), \tag{11}$$

$$dR/dT \sim L^{1/\nu}(\ln L)^{-1/2}\left[1 + O(1/\ln L)\right] \tag{12}$$

with the clean Ising value $\nu = 1$.

Identifying logarithmic corrections in numerical simulations and distinguishing them from power laws with small exponents requires high-quality data over a significant system-size range. Here, we therefore focus on $\Delta J = 0.2$ for which the system reaches the

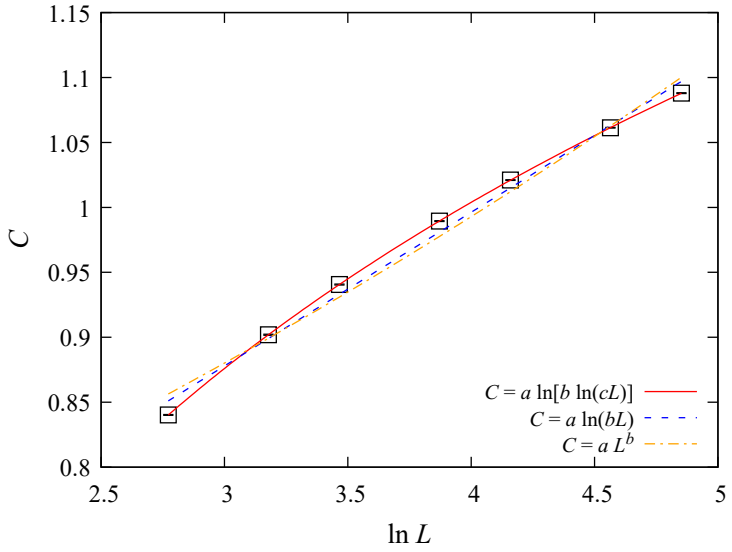

Figure 11. Semilog plot of the specific heat C vs. system size L at the critical temperature $T_c = 1.8670$ for $\Delta J = 0.2$, $J_1 = J_2 = 1$, $p = 1/4$. The data are averages over 30,000 to 100,000 disorder configurations. The resulting statistical errors are much smaller than the symbol size. The solid line represents a fit with $C = a \ln[b \ln(cL)]$. The dashed and dash-dotted lines represent a simple logarithmic fit $C = a \ln(bL)$ and a power-law fit $C = a L^b$, respectively.

asymptotic critical regime for smaller L than for weaker anisotropies (see Figs. 8 and 9). We also simulate more disorder configurations for $\Delta J = 0.2$ than for the other ΔJ to further reduce the statistical errors.

To test the theoretical predictions (8) to (12), we analyze the system-size dependence of C, ψ, χ_s, and $dg_{\rm av}/dT$ at the critical temperature $T_c = 1.8670$. (We use polynomial interpolations in T to determine these values from the simulation data.) Figure 11 presents a semilogarithmic plot of the specific heat C vs. the system size L. The figure clearly shows that the specific heat grows slower than logarithmic with L. It can be fitted well with the

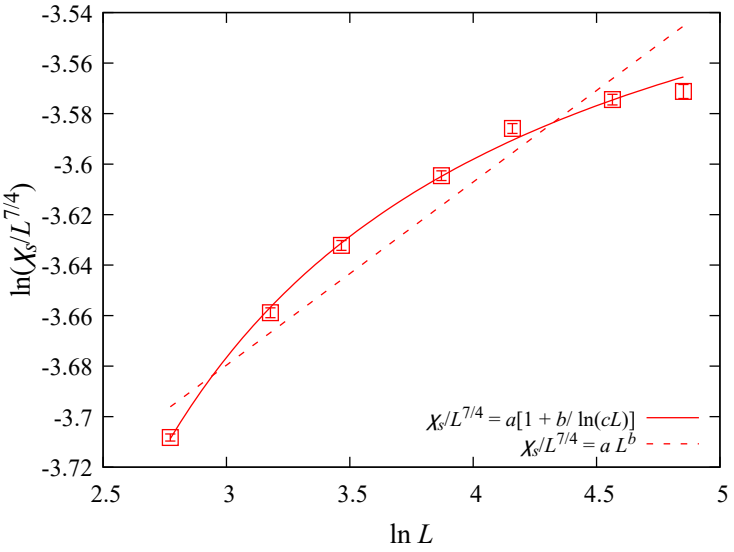

Figure 12. Double logarithmic plot of $\chi_s L^{-7/4}$ vs. system size L at the critical temperature $T_c = 1.8670$ for $\Delta J = 0.2$, $J_1 = J_2 = 1$, $p = 1/4$. The data are averages over 30,000 to 100,000 disorder configurations. The solid line represents a fit with $a[1 + b/\ln(cL)]$. The dashed line represents a simple power-law fit with the functional form $a\, L^b$.

double-logarithmic form $a \ln[b \ln(cL)]$ suggested by eq. (8), giving a reduced error sum $\bar{\chi}^2$ below unity [5]. In contrast, both a simple logarithmic fit $C = a \ln(bL)$ and a power-law fit $C = a\, L^b$ lead to unacceptably large reduced $\bar{\chi}^2$ values of about 800 and 1600, respectively.

To test the predicted behavior (10) of the stripe susceptibility, we divide out the clean Ising power law and plot $\chi_s L^{-7/4}$ vs. L in Fig. 12. The figure demonstrates that $\chi_s L^{-7/4}$ increases more slowly than a power law with L. The data can be fitted reasonably well with the form $a[1 + b/\ln(cL)]$, yielding a reduced error sum of $\bar{\chi}^2 \approx 2.9$. (The reduced error sum drops to about 1.3 if the smallest system size, $L = 16$, is discarded.) A power-law fit produces a unacceptably large $\bar{\chi}^2$ of about 60. The stripe order parameter can be treated analogously, i.e., by analyzing $\psi L^{1/8}$. However, the corrections to the clean Ising behavior

[5] For fitting n data points (x_i, y_i) to a function $f(x)$ containing q fit parameters, the reduced error sum is defined as

$$\bar{\chi}^2 = \frac{1}{n-q} \sum_i \frac{(y_i - f(x_i))^2}{\sigma_i^2} \tag{13}$$

where σ_i^2 is the variance of y_i. The fits are considered to be of good quality if $\bar{\chi}^2 \lessapprox 2$.

for ψ are much weaker than those for χ_s, they only lead to a relative variation of $\psi L^{1/8}$ by about 1% over the size range from $L = 16$ to 128. Within the given statistical errors, both (9) and a power law $\psi \sim L^{-\beta/\nu}$ with $\beta/\nu \approx 0.120$ fit the data.

Finally, we analyze the system-size dependence of the slopes $dg_{\rm av}/dT$ of the Binder cumulant curves at criticality. Within the statistical errors of our data and the uncertainty of T_c, we cannot discriminate between Eq. (12) and simple power law $dg_{\rm av}/dT \sim L^{1/\nu}$ (which gives $\nu \approx 1.12$). Both functional forms fit the data reasonably well.

Taken together, the analyses of C, ψ, χ_s, and $dg_{\rm av}/dT$ provide strong evidence for the critical behavior to belong to the two-dimensional disordered Ising universality class, characterized by the clean Ising exponents with universal logarithmic corrections. To confirm that this behavior also holds for smaller anisotropies, we have studied the system size dependence of the specific heat at criticality for the other simulated ΔJ values. For all $\Delta J > 0.01$, the specific heat data can be fitted well with the double logarithmic form (8), giving reduced error sums around unity. Even for the smallest $\Delta J = 0.01$ and 0.005, the double logarithmic form fits much better than a simple logarithmic dependence or a power law. However, the fit quality is noticeably worse ($\bar{\chi}^2 \approx 3$ and 6, respectively). This can be attributed to the fact that the systems with $\Delta J \leq 0.01$ have not reached the asymptotic critical regime in the size range $L = 16$ to 128 (see Fig. 9).

5. CONCLUSION

To summarize, we have investigated the combined influence of spinless impurities and a spatial interaction anisotropy on the low-temperature stripe phase in the frustrated square-lattice J_1-J_2 Ising model. The impurities reduce the effective interaction strength and thus create random-mass disorder. They also locally break the C_4 rotation symmetry of the lattice, and thus create effective random fields coupling to the nematic order parameter that distinguishes the two possible stripe directions. In the absence of a global anisotropy, these random fields destroy the stripe phase via domain formation.

A global interaction anisotropy that explicitly breaks the C_4 lattice symmetry competes with the random fields and restores the stripe phase at sufficiently low temperatures. By combining percolation theory and results about the domain structure of a biased random-field Ising model, we have predicted that the transition temperature T_c into the stripe phase varies as $T_c \sim 1/|\ln(\Delta J)|$ with the interaction anisotropy ΔJ. This means very small ΔJ are sufficient to restore a robust stripe phase.

We have also studied the resulting phase transition into the stripe phase. Our Monte Carlo results provide strong numerical evidence for the transition to be continuous and to belong to the disordered two-dimensional Ising universality class which is characterized by the clean Ising exponents and universal logarithmic corrections.

Our explicit calculations have implemented the global anisotropy via a difference between the nearest-neighbor interactions in the two lattice directions. Other sources of global anisotropies that break the symmetry between the two stripe directions are expected to have analogous effects. For example, a global anisotropy in the impurity distribution that favors impurity pairs on, say, horizontal nearest neighbor sites over pairs on vertical nearest neighbor sites introduces a bias into the random field distribution. Horizontal stripe domains thus proliferate and form a massive spanning cluster, just as in our case.

Let us also comment on the possibility of a nematic phase. In the absence of a global anisotropy, ($\Delta J = 0$), the phase transition between the paramagnetic high-temperature phase and the stripe low-temperature phase, if any, could in principle split into two separate transitions, the first breaking the C_4 lattice symmetry, producing nematic order, and the second breaking the Ising spin symmetry. In the clean J_1-J_2 Ising model, a nematic phase has not been observed, and same holds for the diluted model studied in Ref. [37] in which the random-field physics is suppressed by impurity anti-correlations. The J_1-J_2 Heisenberg model, in contrast, hosts a nematic phase [64]. We emphasize that a nematic phase transition

cannot occur in principle in the presence of of a nonzero anisotropy $\Delta J \neq 0$. The anisotropy breaks the C_4 lattice symmetry explicitly, spontaneous breaking of this symmetry is thus impossible [6].

Our results have demonstrated that the random-field effects generated by spinless impurities (and, by analogy, bond dilution or other types of quenched randomness) on an order parameter that breaks a real-space symmetry are very sensitive to weak global spatial anisotropies. This may complicate the experimental observation of the random-field physics, for example if the samples feature residual strain. A systematic variation of the anisotropy to test the predictions of the present paper may be achieved, e.g., by applying uniaxial pressure.

We note that the interplay and feedback between the random-field induced domain formation and the magnetic degrees of freedom leads to enhanced fluctuations and slow dynamics even in the absence of a global anisotropy, as was recently demonstrated by mapping the J_1-J_2 Hamiltonian on an Ashkin-Teller model in a random Baxter field [65].

It is interesting to compare our results to those for the square-lattice J_1-J_2 Heisenberg model. Even though magnetic long-range order at nonzero temperatures is impossible in the Heisenberg case due to the Mermin-Wagner theorem [66], the clean J_1-J_2 Heisenberg model features vestigial nematic order [64] associated with the unrealized stripe phase (for $|J_2| > J_1/2$). Impurities create random fields for the nematic order just as in the Ising case, destroying the nematic phase [33]. However, the phase replacing it, a spin-vortex-crystal glass, is more complex than in the Ising case [39].

Impurity-induced random fields also emerge in three-dimensional frustrated magnets. For example, in XY pyrochlore magnets, they have recently been shown to destroy long-range order beyond a critical disorder strength, leading to the formation of a cluster-glass state [38].

[6] This argument does not preclude more complicated scenarios such as a meta-nematic transition in analogy to a meta-magnetic transition in a ferromagnet.

The use of strain to manipulate and "engineer" phases and properties of many-particle systems has recently attracted considerable attention. For instance, it was realized that strain can lift the degeneracy of the ground state manifold of a frustrated Heisenberg antiferromagnet on a Kagome lattice, tuning the system through a sequence of unconventional phases [67]. Our results can be understood as an example of using strain engineering to restore the stripe phase.

ACKNOWLEDGEMENTS

The work in Missouri has been supported in part by the National Science Foundation under Grant Nos. DMR-1828489 and OAC-1919789. The simulations were performed on the Pegasus and Foundry clusters at Missouri S&T. RN acknowledges funding from the Center for Quantum Information Theory in Matter and Spacetime, IIT Madras, and from the Department of Science and Technology, Govt. of India, under Grant No. DST/ICPS/QuST/Theme-3/2019/Q69. We also thank Rafael Fernandes and Joe Meese for helpful discussions.

REFERENCES

[1] Thomas Vojta. Disorder in quantum many-body systems. *Ann. Rev. Condens. Mat. Phys.*, 10:233–252, 2019. doi: 10.1146/annurev-conmatphys-031218-013433.

[2] Yoseph Imry and Michael Wortis. Influence of quenched impurities on first-order phase transitions. *Phys. Rev. B*, 19:3580–3585, Apr 1979. doi: 10.1103/PhysRevB.19.3580.

[3] Kenneth Hui and A. Nihat Berker. Random-field mechanism in random-bond multicritical systems. *Phys. Rev. Lett.*, 62:2507–2510, May 1989. doi: 10.1103/PhysRevLett.62.2507.

[4] Michael Aizenman and Jan Wehr. Rounding of first-order phase transitions in systems with quenched disorder. *Phys. Rev. Lett.*, 62:2503–2506, May 1989. doi: 10.1103/PhysRevLett.62.2503.

[5] A. B. Harris. Effect of random defects on the critical behaviour of Ising models. *J. Phys. C*, 7:1671, 1974. doi: 10.1088/0022-3719/7/9/009.

[6] Daniel S. Fisher. Random transverse field ising spin chains. *Phys. Rev. Lett.*, 69: 534–537, Jul 1992. doi: 10.1103/PhysRevLett.69.534.

[7] D. S. Fisher. Critical behavior of random transverse-field Ising spin chains. *Phys. Rev. B*, 51:6411, 1995. doi: 10.1103/PhysRevB.51.6411.

[8] O. Motrunich, S. C. Mau, D. A. Huse, and D. S. Fisher. Infinite-randomness quan-tum Ising critical fixed points. *Phys. Rev. B*, 61:1160, 2000. doi: 10.1103/Phys-RevB.61.1160.

[9] J. A. Hoyos, C. Kotabage, and T. Vojta. Effects of dissipation on a quantum crit-ical point with disorder. *Phys. Rev. Lett.*, 99:230601, 2007. doi: 10.1103/Phys-RevLett.99.230601.

[10] T. Vojta, C. Kotabage, and J. A. Hoyos. Infinite-randomness quantum critical points induced by dissipation. *Phys. Rev. B*, 79:024401, 2009. doi: 10.1103/Phys-RevB.79.024401.

[11] Thomas Vojta. Disorder-induced rounding of certain quantum phase transitions. *Phys. Rev. Lett.*, 90:107202, Mar 2003. doi: 10.1103/PhysRevLett.90.107202.

[12] José A. Hoyos and Thomas Vojta. Theory of smeared quantum phase transitions. *Phys. Rev. Lett.*, 100:240601, Jun 2008. doi: 10.1103/PhysRevLett.100.240601.

[13] R. B. Griffiths. Nonanalytic behavior above the critical point in a random Ising ferromagnet. *Phys. Rev. Lett.*, 23:17, 1969. doi: 10.1103/PhysRevLett.23.17.

[14] M. Thill and D. A. Huse. Equilibrium behaviour of quantum Ising spin glass. *Physica A*, 214:321, 1995. doi: 10.1016/0378-4371(94)00247-Q.

[15] H. Rieger and A. P. Young. Griffiths singularities in the disordered phase of a quantum ising spin glass. *Phys. Rev. B*, 54:3328, 1996. doi: 10.1103/PhysRevB.54.3328.

[16] A. P. Young and H. Rieger. Numerical study of the random transverse-field ising spin chain. *Phys. Rev. B*, 53:8486–8498, Apr 1996. doi: 10.1103/PhysRevB.53.8486. URL https://link.aps.org/doi/10.1103/PhysRevB.53.8486.

[17] T. Vojta. Rare region effects at classical, quantum, and non-equilibrium phase transi-tions. *J. Phys. A*, 39:R143, 2006. doi: 10.1088/0305-4470/39/22/R01.

[18] T. Vojta. Quantum Griffiths effects and smeared phase transitions in metals: theory and experiment. *J. Low Temp. Phys.*, 161:299, 2010. doi: 10.1007/s10909-010-0205-4.

[19] Thomas Vojta. Phases and phase transitions in disordered quantum systems. *AIP Conference Proceedings*, 1550(1):188–247, 2013. doi: 10.1063/1.4818403. URL https://aip.scitation.org/doi/abs/10.1063/1.4818403.

[20] Yoseph Imry and Shang-keng Ma. Random-field instability of the ordered state of continuous symmetry. *Phys. Rev. Lett.*, 35:1399–1401, Nov 1975. doi: 10.1103/Phys-RevLett.35.1399.

[21] R. Harris, M. Plischke, and M. J. Zuckermann. New model for amorphous magnetism. *Phys. Rev. Lett.*, 31:160–162, Jul 1973. doi: 10.1103/PhysRevLett.31.160. URL https://link.aps.org/doi/10.1103/PhysRevLett.31.160.

[22] K. Binder. Random-field induced interface widths in ising systems. *Z. Phys. B*, 50: 343, 1983.

[23] V. J. Emery, S. A. Kivelson, and J. M. Tranquada. Stripe phases in high-temperature superconductors. *Pro. Nat. Acad. Sci.*, 96(16):8814–8817, 1999. ISSN 00278424. URL http://www.jstor.org/stable/48226.

[24] S. A. Kivelson, I. P. Bindloss, E. Fradkin, V. Oganesyan, J. M. Tranquada, A. Kapitulnik, and C. Howald. How to detect fluctuating stripes in the high-temperature superconductors. *Rev. Mod. Phys.*, 75:1201–1241, Oct 2003. doi: 10.1103/RevModPhys.75.1201. URL https://link.aps.org/doi/10.1103/RevModPhys.75.1201.

[25] Matthias Vojta. Lattice symmetry breaking in cuprate superconductors: stripes, nematics, and superconductivity. *Advances in Physics*, 58(6):699–820, 2009. doi: 10.1080/00018730903122242. URL https://doi.org/10.1080/00018730903122242.

[26] Eduardo Fradkin, Steven A. Kivelson, Michael J. Lawler, James P. Eisenstein, and Andrew P Mackenzie. Nematic Fermi fluids in condensed matter physics. *Ann. Rev. Condens. Mat. Phys.*, 1(1):153–178, 2010. doi: 10.1146/annurev-conmatphys-070909-103925.

[27] R. M. Fernandes, A. V. Chubukov, and J. Schmalian. What drives nematic order in iron-based superconductors? *Nature Physics*, 10:97, 2014. doi: 10.1038/nphys2877. URL http://dx.doi.org/10.1038/nphys2877.

[28] Eduardo Fradkin, Steven A. Kivelson, and John M. Tranquada. Colloquium: Theory of intertwined orders in high temperature superconductors. *Rev. Mod. Phys.*, 87:457–482, May 2015. doi: 10.1103/RevModPhys.87.457. URL https://link.aps.org/doi/10.1103/RevModPhys.87.457.

[29] N. Read and Subir Sachdev. Valence-bond and spin-peierls ground states of low-dimensional quantum antiferromagnets. *Phys. Rev. Lett.*, 62:1694–1697, Apr 1989. doi: 10.1103/PhysRevLett.62.1694. URL https://link.aps.org/doi/10.1103/PhysRevLett.62.1694.

[30] Matthieu Mambrini, Andreas Läuchli, Didier Poilblanc, and Frédéric Mila. Plaquette valence-bond crystal in the frustrated heisenberg quantum antiferromagnet on the square lattice. *Phys. Rev. B*, 74:144422, Oct 2006. doi: 10.1103/PhysRevB.74.144422. URL https://link.aps.org/doi/10.1103/PhysRevB.74.144422.

[31] Anders W. Sandvik. Evidence for deconfined quantum criticality in a two-dimensional heisenberg model with four-spin interactions. *Phys. Rev. Lett.*, 98:227202, Jun 2007. doi: 10.1103/PhysRevLett.98.227202. URL https://link.aps.org/doi/10.1103/PhysRevLett.98.227202.

[32] J. F Fernandez. Random fields generated by dilution in zero external field. *Europhysics Letters (EPL)*, 5(2):129–133, jan 1988. doi: 10.1209/0295-5075/5/2/007. URL https://doi.org/10.1209/0295-5075/5/2/007.

[33] Y V Fyodorov and E F Shender. Random-field effects in antiferromagnets with classically degenerate ground states. *J. Phys. Condens. Mat.*, 3(46):9123–9128, nov 1991. doi: 10.1088/0953-8984/3/46/013. URL https://doi.org/10.1088/0953-8984/3/46/013.

[34] E. W. Carlson, K. A. Dahmen, E. Fradkin, and S. A. Kivelson. Hysteresis and noise from electronic nematicity in high-temperature superconductors. *Phys. Rev. Lett.*, 96:097003, Mar 2006. doi: 10.1103/PhysRevLett.96.097003. URL http://link.aps.org/doi/10.1103/PhysRevLett.96.097003.

[35] Y. L. Loh, E. W. Carlson, and K. A. Dahmen. Noise predictions for stm in systems with local electron nematic order. *Phys. Rev. B*, 81:224207, Jun 2010. doi: 10.1103/PhysRevB.81.224207. URL https://link.aps.org/doi/10.1103/PhysRevB.81.224207.

[36] Laimei Nie, Gilles Tarjus, and Steven Allan Kivelson. Quenched disorder and vestigial nematicity in the pseudogap regime of the cuprates. *Proc. Nat. Acad. Sci.*, 111(22): 7980–7985, 2014. doi: 10.1073/pnas.1406019111.

[37] Shashikant Singh Kunwar, Arnab Sen, Thomas Vojta, and Rajesh Narayanan. Tuning a random-field mechanism in a frustrated magnet. *Phys. Rev. B*, 98:024206, Jul 2018. doi: 10.1103/PhysRevB.98.024206. URL https://link.aps.org/doi/10.1103/PhysRevB.98.024206.

[38] Eric C. Andrade, José A. Hoyos, Stephan Rachel, and Matthias Vojta. Cluster-glass phase in pyrochlore xy antiferromagnets with quenched disorder. *Phys. Rev. Lett.*, 120:097204, Mar 2018. doi: 10.1103/PhysRevLett.120.097204. URL https://link.aps.org/doi/10.1103/PhysRevLett.120.097204.

[39] Michel M. J. Miranda, Igor C. Almeida, Eric C. Andrade, and José A. Hoyos. Phase diagram of a frustrated heisenberg model: From disorder to order and back again. *Phys. Rev. B*, 104:054201, Aug 2021. doi: 10.1103/PhysRevB.104.054201. URL https://link.aps.org/doi/10.1103/PhysRevB.104.054201.

[40] Songbo Jin, Arnab Sen, and Anders W. Sandvik. Ashkin-teller criticality and pseudo-first-order behavior in a frustrated ising model on the square lattice. *Phys. Rev. Lett.*, 108:045702, Jan 2012. doi: 10.1103/PhysRevLett.108.045702. URL https://link.aps.org/doi/10.1103/PhysRevLett.108.045702.

[41] Songbo Jin, Arnab Sen, Wenan Guo, and Anders W. Sandvik. Phase transitions in the frustrated ising model on the square lattice. *Phys. Rev. B*, 87:144406, Apr 2013. doi: 10.1103/PhysRevB.87.144406. URL https://link.aps.org/doi/10.1103/PhysRevB.87.144406.

[42] Ansgar Kalz, Andreas Honecker, and Marion Moliner. Analysis of the phase transition for the ising model on the frustrated square lattice. *Phys. Rev. B*, 84:174407, Nov 2011. doi: 10.1103/PhysRevB.84.174407. URL https://link.aps.org/doi/10.1103/PhysRevB.84.174407.

[43] Ansgar Kalz and Andreas Honecker. Location of the potts-critical end point in the frustrated ising model on the square lattice. *Phys. Rev. B*, 86:134410, Oct 2012. doi: 10.1103/PhysRevB.86.134410. URL https://link.aps.org/doi/10.1103/PhysRevB.86.134410.

[44] E. T. Seppälä, V. Petäjä, and M. J. Alava. Disorder, order, and domain wall roughening in the two-dimensional random field ising model. *Phys. Rev E*, 58:R5217–R5220, Nov 1998. doi: 10.1103/PhysRevE.58.R5217. URL https://link.aps.org/doi/10.1103/PhysRevE.58.R5217.

[45] E. T. Seppälä and M. J. Alava. Susceptibility and percolation in two-dimensional random field ising magnets. *Phys. Rev. E*, 63: 066109, May 2001. doi: 10.1103/PhysRevE.63.066109. URL https://link.aps.org/doi/10.1103/PhysRevE.63.066109.

[46] J. D. Stevenson and M. Weigel. Domain walls and schramm-loewner evolution in the random-field ising model. *EPL (Europhysics Letters)*, 95(4):40001, jul 2011. doi: 10.1209/0295-5075/95/40001. URL https://doi.org/10.1209/0295-5075/95/40001.

[47] Jacob D. Stevenson and Martin Weigel. Percolation and schramm-loewner evolution in the 2d random-field ising model. *Comp. Phys. Commun.*, 182(9):1879–1882, 2011. ISSN 0010-4655. doi: https://doi.org/10.1016/j.cpc.2010.11.028. URL https://www.sciencedirect.com/science/article/pii/S0010465510004790.

[48] D. Stauffer and A. Aharony. *Introduction to Percolation Theory*. CRC Press, Boca Raton, 1991.

[49] J. Cardy. *Scaling and renormalization in statistical physics*. Cambridge University Press, Cambridge, 1996.

[50] Viktor S. Dotsenko and Vladimir S. Dotsenko. Critical behaviour of the phase transition in the 2d ising model with impurities. *Adv. Phys.*, 32(2):129–172, 1983. doi: 10.1080/00018738300101541.

[51] B. N. Shalaev. *Fiz. Tverd. Tela (Leningrad)*, 36:3002, 1984. [Sov. Phys.– Solid State **26**, 1811 (1984)].

[52] R. Shankar. Exact critical behavior of a random bond two-dimensional ising model. *Phys. Rev. Lett.*, 58:2466–2469, Jun 1987. doi: 10.1103/PhysRevLett.58.2466.

[53] M. Fähnle, T. Holey, and J. Eckert. Monte carlo renormalization group calculations of critical exponents in site-diluted 2d and 3d ising systems. *J. of Magn. Magn. Mater.*, 104–107(0):195–196, 1992. doi: http://dx.doi.org/10.1016/0304-8853(92)90762-D. URL http://www.sciencedirect.com/science/article/pii/030488539290762D.

[54] Jae-Kwon Kim and Adrian Patrascioiu. Critical behavior of the specific heat in the two dimensional site diluted ising system. *Phys. Rev. Lett.*, 72:2785–2788, Apr 1994. doi: 10.1103/PhysRevLett.72.2785. URL http://link.aps.org/doi/10.1103/PhysRevLett.72.2785.

[55] Reimer Kühn. Critical behavior of the randomly spin diluted 2d ising model: A grand ensemble approach. *Phys. Rev. Lett.*, 73:2268–2271, Oct 1994. doi: 10.1103/PhysRevLett.73.2268.

[56] Qiong Zhu, Xin Wan, Rajesh Narayanan, José A. Hoyos, and Thomas Vojta. Emerging criticality in the disordered three-color ashkin-teller model. *Phys. Rev. B*, 91:224201, Jun 2015. doi: 10.1103/PhysRevB.91.224201.

[57] Ulli Wolff. Collective monte carlo updating for spin systems. *Phys. Rev. Lett.*, 62:361–364, Jan 1989. doi: 10.1103/PhysRevLett.62.361. URL https://link.aps.org/doi/10.1103/PhysRevLett.62.361.

[58] Robert H. Swendsen and Jian-Sheng Wang. Nonuniversal critical dynamics in monte carlo simulations. *Phys. Rev. Lett.*, 58:86–88, Jan 1987. doi: 10.1103/PhysRevLett.58.86.

[59] A. Kalz, A. Honecker, S. Fuchs, and T. Pruschke. Phase diagram of the ising square lattice with competing interactions. *Eur. Phys. J. B*, 65:533, 2008. doi: 10.1140/epjb/e2008-00359-6.

[60] Nicholas Metropolis, Arianna W. Rosenbluth, Marshall N. Rosenbluth, Augusta H. Teller, and Edward Teller. Equation of state calculations by fast computing machines. *J. Chem. Phys.*, 21(6):1087–1092, 1953. doi: 10.1063/1.1699114. URL https://doi.org/10.1063/1.1699114.

[61] Giorgio Mazzeo and Reimer Kühn. Critical behavior of the two-dimensional spin-diluted ising model via the equilibrium ensemble approach. *Phys. Rev. E*, 60:3823–3836, Oct 1999. doi: 10.1103/PhysRevE.60.3823.

[62] Martin Hasenbusch, Francesco Parisen Toldin, Andrea Pelissetto, and Ettore Vicari. Universal dependence on disorder of two-dimensional randomly diluted and random-bond $\pm J$ ising models. *Phys. Rev. E*, 78:011110, Jul 2008. doi: 10.1103/PhysRevE.78.011110.

[63] R. Kenna and J. J. Ruiz-Lorenzo. Scaling analysis of the site-diluted ising model in two dimensions. *Phys. Rev. E*, 78:031134, Sep 2008. doi: 10.1103/PhysRevE.78.031134.

[64] P. Chandra, P. Coleman, and A. I. Larkin. Ising transition in frustrated heisenberg models. *Phys. Rev. Lett.*, 64:88–91, Jan 1990. doi: 10.1103/PhysRevLett.64.88. URL https://link.aps.org/doi/10.1103/PhysRevLett.64.88.

[65] W.J. Meese, T. Vojta, and R.M. Fernandes. Enhanced fluctuations and correlations due to random strain disorder. unpublished, 2021.

[66] N. D. Mermin and H. Wagner. Absence of ferromagnetism or antiferromagnetism in one- or two-dimensional isotropic heisenberg models. *Phys. Rev. Lett.*, 17:1133–1136, Nov 1966. doi: 10.1103/PhysRevLett.17.1133. URL https://link.aps.org/doi/10.1103/PhysRevLett.17.1133.

[67] Mary Madekynn Nayga and Matthias Vojta. Strain tuning of highly frustrated magnets: Order and disorder in the distorted kagome heisenberg antiferromagnet. unpublished, 2021.

II. CONTACT PROCESS WITH SIMULTANEOUS SPATIAL AND TEMPORAL DISORDER

Xuecheng Ye

Department of Physics, Missouri University of Science and Technology, Rolla, MO 65409, USA

Thomas Vojta

Department of Physics, Missouri University of Science and Technology, Rolla, MO 65409, USA

ABSTRACT

We study the absorbing-state phase transition in the one-dimensional contact process under the combined influence of spatial and temporal random disorders. We focus on situations in which the spatial and temporal disorders decouple. Couched in the language of epidemic spreading, this means that some spatial regions are, at all times, more favorable than others for infections, and some time periods are more favorable than others independent of spatial location. We employ a generalized Harris criterion to discuss the stability of the directed percolation universality class against such disorder. We then perform large-scale Monte Carlo simulations to analyze the critical behavior in detail. We also discuss how the Griffiths singularities that accompany the nonequilibrium phase transition are affected by the simultaneous presence of both disorders.

1. INTRODUCTION

Macroscopic systems far from thermal equilibrium can undergo abrupt transformations between different steady states when their external conditions are varied. These nonequilibrium phase transitions share many features with thermodynamic (equilibrium) phase transitions including collective behavior and large-scale fluctuations. They can be found, for example, in interface growth, chemical reactions, granular flow, and in biological problems such as population dynamics or epidemic spreading (for reviews, see, e.g., Refs. [1, 2, 3, 4, 5]).

When a nonequilibrium phase transition separates an active fluctuating steady state from an inactive absorbing state in which fluctuations completely stop, it is called an absorbing state transition. Experimental realizations of absorbing state transitions have been observed, for example, in turbulent liquid crystals [6], periodically driven suspensions [7, 8], bacteria colony biofilms [9, 10], and the dynamics of superconducting vortices [11]. Janssen and Grassberger [12, 13] conjectured that all absorbing-state transitions with a scalar order parameter and short-range interactions belong to the directed percolation (DP) universality class [14], provided they do not feature extra symmetries or conservation laws.

Many realistic systems undergoing absorbing state transitions feature random spatial inhomogeneities (i.e., spatial disorder) or random variations of their external parameters with time (i.e., temporal disorder). The question of how disorder affects absorbing state transitions (and the DP universality class in particular) has attracted significant attention during the last two decades or so. According to the Harris criterion [15], the DP critical point is unstable against spatial disorder because its correlation length exponent $\nu_\perp$ violates the inequality $d\nu_\perp > 2$ in all physical dimensions, $d = 1, 2$, and 3. The DP critical point is also unstable against temporal disorder because its correlation time exponent $\nu_\parallel = z\nu_\perp$ violates Kinzel's generalization [16] $\nu_\parallel > 2$ of the Harris criterion (see Ref. [17] for an extension of the Harris criterion to general spatio-temporal disorder).

Spatial disorder has been demonstrated to have dramatic effects on the DP universality class. Hooyberghs et al. [18, 19] developed a strong-disorder renormalization group (RG) [20, 21] method and predicted the transition to be governed by an unconventional infinite-randomness critical point. It is accompanied by strong power-law Griffiths singularities [22, 23, 24] in the parameter region close to the transition. The infinite-randomness critical point scenario was confirmed by large-scale Monte Carlo simulations in one, two, and three space dimensions [25, 26, 27, 28]. Similar critical behavior was also observed in diluted systems near the percolation threshold [29, 30] and in systems featuring aperiodic order [31].

More recently, the effects of temporal disorder on the DP universality class were analyzed by means of a real-time "strong-noise" RG [32]. This method predicts that the disorder strength diverges with increasing time scale at criticality, and the probability distribution of the density becomes infinitely broad, even on a logarithmic scale. This infinite-noise critical behavior can be understood as the temporal counterpart of infinite-randomness critical behavior in spatially disordered systems, but with exchanged roles of space and time. The RG predictions were later confirmed by Monte Carlo simulations [33, 34]. In addition, Vazquez et al. [35] identified a temporal analog of the Griffiths phase in spatially disordered systems that features an unusual power-law relation between lifetime and system size on the active side of the phase transition.

Although the effects of pure spatial disorder and pure temporal disorder have been studied in some detail, their simultaneous influence on absorbing state transitions has received much less attention. This is likely due to the fact that uncorrelated spatiotemporal disorder is an irrelevant perturbation at the clean DP critical point and thus not expected to change the critical behavior (see, e.g., Ref [2]). However, many experimental applications do not lead to uncorrelated spatiotemporal disorder. Consider, for example, an epidemic spreading in an inhomogeneous environment under conditions that fluctuate with time. If the locations of favorable spatial regions do not change with time, and if favorable conditions in

time apply uniformly to the entire population, the resulting spatiotemporal disorder features infinite-range correlations and is thus expected to be a relevant perturbation at the clean DP critical point.

In the present paper, we combine generalizations of the Harris criterion, optimal fluctuation arguments, and large-scale Monte Carlo simulations to investigate the fate of the nonequilibrium phase transition in the contact process [36] under the influence of such spatiotemporal disorder. We find that adding weak temporal disorder to a spatially disordered system does not change the infinite-randomness critical behavior. Analogously, adding weak spatial disorder to a temporally disordered system does not affect the infinite-noise critical behavior. We also explore the fate of the transitions of both disorders are strong. In addition, we demonstrate that the functional form of the Griffiths singularities changes in the simultaneous presence of both disorders.

Our paper is organized as follows. The contact process and our implementation of the spatiotemporal disorder are introduced in Sec. 2. Section 3 briefly summarizes, what is known about the phase transition in the clean contact process, the spatially disordered contact process, and the temporally disordered contact process. The effects of rare regions and the resulting Griffiths singularities in the contact process with purely spatial or purely temporal disorder are summarized in Sec. 4. The computer simulations methods are introduced in Sec. 5. Sections 6 and 7 are devoted to our results for the contact process in the presence of spatiotemporal disorder. We conclude in Sec. 8.

2. CONTACT PROCESS

The non-equilibrium phase transition in the clean contact process is well studied and belongs to the DP universality class [36]. We consider a d-dimensional hypercubic lattice in which each site can be either active (infected) or inactive (healthy). As the time progresses, an active site can either infect its lattice neighbors or spontaneously become inactive. More specifically, the time evolution of the contact process is a continuous-time Markov process

during which the infected sites heal at rate μ, and infect their inactive neighbors at infection rate λ. Thus an inactive site become active at rate $\lambda n/2d$. Here, n stands for the number of active neighbors. The long-time fate of the contact process is determined by the ratio between the infection rate λ and the healing rate μ. (Since only the ratio matters, μ can be set to unity without loss of generality.)

For small infection rate λ, the healing process is favored. Because of the lack of new infections, all active sites will heal eventually. The system thus ends up in the absorbing healthy state. This is called the inactive phase. For large infection rate λ, the active sites proliferate and never die out. This is called the active phase. The active and inactive phases are separated by a transition in the DP universality class.

We now introduce spatial and temporal disorder into the infection rate λ by defining the local infection rate $\lambda(x,t)$ at lattice site x and time t with a multiplicative structure,

$$\lambda(x,t) = \lambda_0 f(x) g(t). \tag{1}$$

Here, the random variables $f(x)$ and $g(t)$ are nonnegative and independent of each other. They are characterized by the averages

$$\langle f(x)\rangle = \bar{f}\,, \quad \langle g(t)\rangle = \bar{g} \tag{2}$$

and short-range correlations

$$\langle f(x) f(x')\rangle - \bar{f}^2 = \sigma_f^2 \delta(x-x')\,, \tag{3}$$

$$\langle g(t) g(t')\rangle - \bar{g}^2 = \sigma_g^2 \delta(t-t') \tag{4}$$

The multiplicative structure implies that favorable (for the infection) spatial regions do not change with time, and favorable time intervals apply to the whole system. In other words, the disorder contains infinite-range correlations in space and time. This is reflected in the

covariance function of $\lambda(x,t)$ which reads

$$\begin{aligned} G(x-x',t-t') &= \langle\lambda(x,t)\lambda(x',t')\rangle - \langle\lambda(x,t)\rangle\langle\lambda(x',t')\rangle \\ &= \lambda_0^2\sigma_f^2\sigma_g^2\delta(x-x')\delta(t-t') \\ &\quad +\lambda_0^2\sigma_f^2\bar{g}^2\delta(x-x') \\ &\quad +\lambda_0^2\sigma_g^2\bar{f}^2\delta(t-t') \ . \end{aligned} \tag{5}$$

Here the first term represents uncorrelated spatiotemporal disorder, the second term is perfectly correlated in time, and the last term is perfectly correlated in space. Purely spatial disorder can be understood as a special case of (1) with g = const. Analogously, purely temporal disorder emerges for f = const.

3. SCALING SCENARIOS

In this section, we briefly summarize what is known about the critical behavior of the nonequilibrium phase transitions in the clean contact process, the contact process with purely spatial disorder, and the contact process with purely temporal disorder.

3.1. CLEAN CONTACT PROCESS: CONVENTIONAL POWER-LAW CRITICAL BEHAVIOR

The (clean) DP universality class features three independent critical exponents which can be chosen to be β, $\nu_\perp$, and z (see, e.g., Ref. [2]). The order parameter exponent β controls how the steady state density $\rho_{\rm stat}$ varies as the infection rate λ approaches its critical value λ_c from the active side of the transition,

$$\rho_{\rm stat} \sim (\lambda-\lambda_c)^\beta \sim r^\beta \ , \tag{6}$$

with $r = (\lambda - \lambda_c)/\lambda_c$ the dimensionless distance from criticality. The correlation length exponent $\nu_\perp$ controls the divergence of the (spatial) correlation length $\xi_\perp$,

$$\xi_\perp \sim |r|^{-\nu_\perp} , \tag{7}$$

and the dynamical exponent z relates the correlation time $\xi_\parallel$ to the correlation length,

$$\xi_\parallel \sim \xi_\perp^z . \tag{8}$$

The density ρ of active sites as a function of the distance r from criticality, the time t, and the system size L fulfills the homogeneity relation

$$\rho(r, t, L) = \ell^{\beta/\nu_\perp} \rho(r\ell^{-1/\nu_\perp}, t\ell^z, L\ell) \tag{9}$$

where ℓ is an arbitrary dimensionless length scale factor. The survival probability P_s is the probability that an active cluster survives to time t if the epidemic starts at time 0 from a single infected site in an otherwise inactive lattice. In the DP universality class, P_s has the same scaling form as the density of active sites (9) [7],

$$P_s(\Delta, t, L) = \ell^{\beta/\nu_\perp} P_s(\Delta\ell^{-1/\nu_\perp}, t\ell^z, L\ell) . \tag{10}$$

The pair connectedness function $C(x, t)$ is given by the probability that site x is infected at time t when the time evolution starts from a single infected site at $x = 0$ and time $t = 0$. The scale dimension of C is $2\beta/\nu_\perp$ because it involves a product of two densities [8]. This

[7] This stems from a special time reversal symmetry [14]. At general absorbing state transitions, e.g., with several absorbing states, the survival probability scales with an exponent β' which may be different from β (see, e.g., [2]).

[8] This relation relies on hyperscaling; it is only valid below the upper critical dimension d_c^+, which is four for directed percolation.

implies the scaling form

$$C(r, x, t, L) = \ell^{2\beta/\nu_\perp} C(r\ell^{-1/\nu_\perp}, x\ell, t\ell^z, L\ell) \ . \tag{11}$$

The number N_s of sites in an active cluster growing from a single seed can be calculated by integrating C over all x,

$$N_s(r, t, L) = \ell^{2\beta/\nu_\perp - d} N_s(r\ell^{-1/\nu_\perp}, t\ell^z, L\ell) \ . \tag{12}$$

Because the mean-square radius R of this active cluster has the dimension of a length, its scaling form reads

$$R(r, t, L) = \ell^{-1} R(r\ell^{-1/\nu_\perp}, t\ell^z, L\ell) \ . \tag{13}$$

The time dependencies of ρ, P_s, N_s and R at the critical point $r = 0$ and in the thermodynamic limit $L \to \infty$ can be easily derived from Eqs. (9) to (13) by setting the scale factor ℓ to suitable values. In the long-time limit, the density of infected sites and the survival probability are expected to follow the relations

$$\rho(t) \sim t^{-\delta}, \qquad P_s(t) \sim t^{-\delta} \tag{14}$$

with $\delta = \beta/(\nu_\perp z)$. The mean-square radius and the number of sites of an active cluster starting from a single seed site behave as

$$R(t) \sim t^{1/z}, \qquad N_s(t) \sim t^{\Theta} \ . \tag{15}$$

Here, $\Theta = d/z - 2\beta/(\nu_\perp z)$ is the critical initial slip exponent. These results imply that Θ, δ, and z are not independent, they fulfill the hyperscaling relation $\Theta + 2\delta = d/z$.

Highly accurate estimates of the critical exponents for the clean DP universality class in $d = 1$ dimensions were computed by series expansions [37]: $\beta = 0.276486$, $\nu_\perp = 1.096854$, $z = 1.580745$, $\delta = 0.159464$, and $\Theta = 0.313686$.

The clean correlation length exponent violates Harris' inequality $d\nu_\perp > 2$ [15]. Analogously, the exponent combination $\nu_\parallel = z\nu_\perp$ violates the corresponding inequality $\nu_\parallel > 2$ for temporal disorder [16]. Consequently, the clean DP critical behavior is unstable against both purely spatial disorder and purely temporal disorder.

3.2. SPATIALLY DISORDERED CONTACT PROCESS: INFINITE-RANDOMNESS CRITICAL BEHAVIOR

Hooyberghs et al. [18, 19] employed a strong-disorder renormalization group (RG) [20, 21] method to demonstrate that the nonequilibrium phase transition in the spatially disordered contact process is governed by an exotic infinite-randomness critical point in the same universality class as the random transverse-field Ising model [38, 39]. This was later verified by Monte-Carlo simulations in one, two, and three space dimensions [25, 26, 27, 28].

A key difference between a conventional critical point and an infinite-randomness critical point is the replacement of the power-law relation (8) between correlation length and time by an exponential (activated) one,

$$\ln(\xi_\parallel/t_0) \sim \xi_\perp^\psi \, . \tag{16}$$

Here ψ is the so-called tunneling exponent, and t_0 is a microscopic time scale. This exponential relation implies that the dynamical exponent z is formally infinite at an infinite-randomness critical point. In contrast, the static scaling relations remain of power-law type, i.e., eqs. (6) and (7) remain valid.

The scaling forms of disorder-averaged observables can be obtained by simply substituting the variable combination $\ln(t/t_0)\ell^{\psi}$ for $t\ell^{z}$ in the arguments of the scaling functions, yielding

$$\rho(r, \ln(t/t_0), L) = \ell^{\beta/\nu_\perp} \rho(r\ell^{-1/\nu_\perp}, \ln(t/t_0)\ell^{\psi}, L\ell) \; , \tag{17}$$

$$P_s(r, \ln(t/t_0), L) = \ell^{\beta/\nu_\perp} P_s(r\ell^{-1/\nu_\perp}, \ln(t/t_0)\ell^{\psi}, L\ell) \; , \tag{18}$$

$$N_s(r, \ln(t/t_0), L) = \ell^{2\beta/\nu_\perp - d} N_s(r\ell^{-1/\nu_\perp}, \ln(t/t_0)\ell^{\psi}, L\ell) \; , \tag{19}$$

$$R(r, \ln(t/t_0), L) = \ell^{-1} R(r\ell^{-1/\nu_\perp}, \ln(t/t_0)\ell^{\psi}, L\ell) \; . \tag{20}$$

The resulting critical time dependencies of ρ, P_s, N_s, and R are logarithmic (in the thermodynamic limit),

$$\rho(t) \sim [\ln(t/t_0)]^{-\bar{\delta}}, \qquad P_s(t) \sim [\ln(t/t_0)]^{-\bar{\delta}} \; , \tag{21}$$

$$R(t) \sim [\ln(t/t_0)]^{1/\psi}, \qquad N_s(t) \sim [\ln(t/t_0)]^{\bar{\Theta}} \; , \tag{22}$$

with $\bar{\delta} = \beta/(\nu_\perp \psi)$ and $\bar{\Theta} = d/\psi - 2\beta/(\nu_\perp \psi)$.

Within the strong-disorder renormalization group approach, the critical exponents of the spatially disordered one-dimensional contact process can be calculated exactly. Their numerical values are $\beta = 0.38197$, $\nu_\perp = 2$, $\psi = 0.5$, $\bar{\delta} = 0.38197$, and $\bar{\Theta} = 1.2360$.

3.3. TEMPORALLY DISORDERED CONTACT PROCESS: INFINITE-NOISE CRITICAL BEHAVIOR

To attack the problem of temporal disorder in the contact process, Vojta and Hoyos [32] developed a real-time strong-noise renormalization group that can be understood as the temporal counterpart of the strong-disorder renormalization group for spatially disordered systems. This renormalization group predicts (in any finite dimensionality d) a Kosterlitz-

Thouless [40] type transition at which the critical fixed point is the end point of a line of fixed points that describe the ordered phase. Consequently, observables at criticality show the same qualitative behavior as in the active phase, except for logarithmic corrections. This can be expressed in the following heuristic scaling theory [33].

The density of active sites fulfills the scaling form

$$\rho(r,t,L) = (\ln \ell)^{-\beta/\bar{\nu}_\perp} \rho(r(\ln \ell)^{1/\bar{\nu}_\perp}, t\ell^{-z}, L\ell^{-1}) \tag{23}$$

with order parameter exponent $\beta = 1/2$, correlation length exponent $\bar{\nu}_\perp = 1/2$, and dynamical exponent $z = 1$. The scaling combination $r(\ln \ell)^{1/\bar{\nu}_\perp}$ reflects the exponenial dependence of the correlation length $\xi_\perp$ on the distance r from criticality. Because the time reversal symmetry of DP [14] is still valid in the presence of temporal disorder, the survival probability has the same scaling form,

$$P_s(r,t,L) = (\ln \ell)^{-\beta/\bar{\nu}_\perp} P_s(r(\ln \ell)^{1/\bar{\nu}_\perp}, t\ell^{-z}, L\ell^{-1}) \ . \tag{24}$$

The cloud of active sites originating from a single infected seed site spreads ballistically, apart from logarithmic corrections, yielding the scaling forms

$$N_s(r,t,L) = \ell^d (\ln \ell)^{-y_N} N_s(r(\ln \ell)^{1/\bar{\nu}_\perp}, t\ell^{-z}, L\ell^{-1}) \ , \tag{25}$$

$$R(r,t,L) = \ell (\ln \ell)^{-y_R} R(r(\ln \ell)^{1/\bar{\nu}_\perp}, t\ell^{-z}, L\ell^{-1}) \ . \tag{26}$$

The exponents y_N and y_R that govern the logarithmic corrections are not independent of each other. Because $N_s \sim P_s \rho R^d$, they must fulfill the relation $y_N = 2\beta/\bar{\nu}_\perp + d y_R$.

Setting $L = \infty$, $r = 0$, and $\ell = t^{1/z} = t$ in the scaling forms (23) to (26) gives the time dependencies of the observables at criticality,

$$\rho(t) \sim (\ln t)^{-\bar{\delta}}, \qquad P_s(t) \sim (\ln t)^{-\bar{\delta}} \tag{27}$$

$$R(t) \sim t^{1/z}(\ln t)^{-y_R}, \quad N_s(t) \sim t^{\Theta}(\ln t)^{-y_N} \tag{28}$$

with $\bar{\delta} = \beta/\bar{\nu}_{||} = 1$ and $\Theta = d/z = d$.

This scaling theory was confirmed by large-scale Monte Carlo simulations of the contact process with temporal disorder in one and two space dimensions [33]. The simulations resulted in the estimates $y_N = 3.6(4)$ and $y_R = 1.7(3)$ for the exponents governing the logarithmic corrections in one dimension [9].

4. RARE EVENTS AND GRIFFITHS SINGULARITIES

Spatial and temporal disorder do not only destabilize the DP critical behavior, rare strong disorder fluctuations also lead to unusual singularities, the Griffiths singularities [22, 41] in an entire parameter region around the transition. This section briefly summarizes the rare region effects in the contact process with purely spatial disorder, and in the contact process with purely temporal disorder.

4.1. SPATIAL DISORDER

The inactive phase of a spatially disordered contact process can generally be divided into two regions. Far away from criticality (i.e., for sufficiently small infection rate), the system approaches the absorbing state exponentially fast in time, just as in the absence of disorder. This is the conventional inactive phase. For infection rates closer to the disordered critical point, the system may feature large spatial regions that are locally in the active phase even though the system as a whole is still inactive. Because these regions are of finite size,

[9] The numbers in brackets indicate the errors of the last digits.

they cannot support a nonzero steady-state density, but their density decay is very slow since it requires a rare density fluctuation of the entire region [23, 24]. The range in parameter space for which such rare locally active spatial regions exist is called the (inactive) Griffith phase.

The contribution $\rho_{RR}(t)$ of the rare regions to system's density can be easily estimated as

$$\rho_{RR}(t) \sim \int dL_{RR}\, L_{RR}^{d}\, w(L_{RR}) \exp\left[-t/\tau(L_{RR})\right] \ , \tag{29}$$

where $w(L_{RR})$ is the probability for finding a rare region of linear size L_{RR}, and $\tau(L_{RR})$ is its decay time. For uncorrelated or short-range correlated disorder, the rare region probability is given by $w(L_{RR}) \sim \exp(-bL_{RR}^{d})$ (up to pre-exponential factors). The decay time reads $\tau(L_{RR}) \sim \exp(aL_{RR}^{d})$ because a coordinated fluctuation of the entire rare region is required to take it to the absorbing state.

In the long-time limit, the integral (29) can be evaluated using the saddle point method, yielding an anomalous power-law decay of the density in the Griffiths phase,

$$\rho(t) \sim t^{-b/a} = t^{-d/z'} \ , \tag{30}$$

rather then the exponential decay in the conventional inactive phase. Here $z' = da/b$ is the *nonuniversal* Griffiths dynamical exponent. The survival probability P_s shows exactly the same time dependence. The behavior of z' close to the infinite-randomness critical point λ_c follows from the strong-disorder renormalization group [19, 39],

$$z' \sim |\lambda - \lambda_c|^{-\psi\nu_\perp} \ , \tag{31}$$

where ψ and $\nu_\perp$ are the critical exponents of the infinite-randomness critical point. Similar rare region effects also exist in the active phase where they govern the approach to the nonzero steady-state density.

4.2. TEMPORAL DISORDER

The temporal Griffiths phase, introduced by Vazquez et al. [35], is the part of the active phase in which the life time τ_L of a finite-size sample shows an anomalous (non-exponential) dependence on the system size L.

The temporal Griffiths behavior is the result of rare, long time intervals during which the system is temporarily on the inactive side of the transition. The probability of finding such a time interval of length T_{RR} depends exponentially on its length, $w(T_{RR}) \sim \exp(-bT_{RR})$ (neglecting pre-exponential factors). During T_{RR}, the density of active sites decays exponentially as $\rho \sim \exp(-at)$. Because the typical life time of a system of linear size L can be estimated as time when the density reaches the value L^{-d}, a system of size L will die during a rare time interval of length $T_{RR} \sim (d/a) \ln L$. The characteristic time it takes for such a rare time interval to appear is given by $\tau \sim w^{-1}(T_{RR}) \sim \exp(bT_{RR})$. Consequently, the life time τ of a finite-size system in the temporal Griffiths phase shows a power-law dependence on its size L,

$$\tau(L) \sim L^{db/a} = L^{d/\kappa} \ . \tag{32}$$

The infinite-noise renormalization group [32, 33] predicts that the Griffiths exponent $\kappa = a/b$ take the value $\kappa_c = d$ right at criticality. κ decreases with increasing distance from criticality and is expected to vanish at the boundary between the temporal Griffiths phase and the conventional active phase (in which the life time increases exponentially with system size). The temporal Griffiths behavior has been confirmed by Monte Carlo simulations of the contact process with temporal disorder in one and two space dimensions [33].

5. SIMULATIONS METHODS

Our computer simulations focus on the case of one space dimension. The numerical implementation of the one-dimension contact process follows the method developed by Dickman [42]. We start at $t = 0$ from a system with at least one active site. For each time step, we follow this sequence: First, an active site is randomly chosen from all N_a active sites. Then we randomly let this site infect one of its neighbors with probability $\lambda(x,t)/[\lambda(x,t)+1]$ or become inactive with probability $1/[\lambda(x,t)+1]$. If the infection process is chosen, only a single neighbor is infected, chosen randomly. The time increment associated with this sequence is $1/N_a$.

As discussed in Sec. 2, the local infection rates take the form $\lambda(x,t) = \lambda_0 f(x) g(t)$, where λ_0 is the control parameter used to tune the phase transition, and $f(x)$ and $g(t)$ are independent random variables. (In the following, we will drop the subscript 0 from λ_0 if the meaning is clear.) For the computer simulations, we employ the binary probability distribution

$$P(f) = (1-p)\delta(f-1) + p(f-c) \;, \tag{33}$$

with $0 < c \leq 1$. This means the local infection rate is reduce by a factor c with probability p. $g(t)$ is piecewise constant over short time intervals of length $\Delta t = 6$, i.e., $g(t) = g_n$ for $t_{n+1} > t > t_n$ with $t_n = n\Delta t$. The g_n follow a binary probability distribution

$$P(g_n) = (1-p_t)\delta(g_n-1) + p_t(g_n - c_t) \;. \tag{34}$$

We study two sequences of parameters. The first sequence starts from (strong) purely spatial disorder, adding an increasing amount of temporal disorders ($p = 0.3$, $c = 0.2$, $p_t = 0.2$ and c_t varying from 1.0 to 0.12). The other sequence starts from (strong) purely temporal disorder and adds an increasing amount of spatial disorder ($p_t = 0.2$, $c_t = 0.05$, $p = 0.2$ and c varying from 1.0 to 0.05).

For each parameter set λ_0, p, c, p_t and c_t, the results are averaged over many disorder realizations (between 700 and 5×10^5). We employ two types of simulation runs, (i) decay simulations in which the system starts with all sites being active. In this case, we perform one simulation run per disorder configuration and observe the active site density $\rho(t)$. (ii) Spreading simulation start with a single active seed site only. In this case, we perform 5 to 10^5 runs per disorder configuration and analyze the survival probability $P_s(t)$, the average number of active sites $N_s(t)$ and the (mean-square) radius $R(t)$ of the active cloud. In order to eliminate the finite-size effects for spreading runs, the system size is chosen to be much larger than the maximum active cloud size.

6. RESULTS: CRITICAL BEHAVIOR

6.1. GENERALIZED HARRIS CRITERION

The Harris criterion $d\nu > 2$ controls the stability of a clean critical point against uncorrelated (or short-range correlated) purely spatial disorder. Analogously, the inequality $\nu_\parallel > 2$ governs the stability against uncorrelated purely temporal disorder [16]. As pointed out in Sec. 3.1, the clean DP critical point is unstable against both purely spatial disorder and purely temporal disorder because its critical exponents violate both inequalities.

The effects of general spatiotemporal disorder can be ascertained by means of the generalized Harris criterion [17]. It predicts that a critical point is (perturbatively) stable against weak spatiotemporal disorder, if the disorder covariance function $G(x,t)$ fulfills the condition

$$\xi_\perp^{2/\nu_\perp - d} \xi_\parallel^{-1} \int_{-\xi_\perp/2}^{\xi_\perp/2} d^d x \int_{-\xi_\parallel/2}^{\xi_\parallel/2} dt\, G(x,t) \to 0 \tag{35}$$

as the critical point is approached, i.e, for $\xi_\perp, \xi_\parallel \to \infty$ with the appropriate scaling relation between $\xi_\perp$ and $\xi_\parallel$. For power-law dynamical scaling this means $\xi_\parallel \sim \xi_\perp^z$, and for activated scaling $\ln(\xi_\parallel / t_0) \sim \xi_\perp^\psi$.

For completely uncorrelated spatiotemporal disorder with $G(x,t) \sim \delta(x)\delta(t)$, the l.h.s. of Eq. (35) behaves as $\xi_\perp^{2/\nu_\perp - d}\xi_\parallel^{-1}$. The resulting stability criterion thus reads $(d + z)\nu_\perp > 2$ in the case of power law dynamical scaling. The clean DP critical exponents fulfill this inequality implying that uncorrelated spatiotemporal disorder is not a relevant perturbation, as was already pointed out in the literature (see, e.g., Ref. [2]).

Let us now apply the generalized Harris criterion to the disorder (1) studied in this paper. Inserting the covariance function (5), $G(x,t) = \lambda_0^2\sigma_f^2\sigma_g^2\delta(x)\delta(t) + \lambda_0^2\sigma_f^2\bar{g}^2\delta(x) + \lambda_0^2\sigma_g^2\bar{f}^2\delta(t)$, into Eq. (35) produces three contributions. The first term (which represents uncorrelated disorder) goes to zero in the critical limit $\xi_\perp \to \infty$ provided the critical exponents fulfill the inequality $(d + z)\nu_\perp > 2$. The second term vanishes for $d\nu_\perp > 2$, and the third term vanishes for $z\nu_\perp > 2$. Because the DP critical exponents violate the latter two inequalities, the disorder (1) is a relevant perturbation at the clean DP critical point and expected to modify the critical behavior.

The generalized Harris criterion can also be used to analyze the addition of weak temporal disorder to the already spatially disordered contact process. For purely temporal disorder, $G(x,t) \sim \delta(t)$. The l.h.s. of (35) thus behaves as $\xi_\perp^{2/\nu_\perp}\xi_\parallel^{-1}$. Because the correlation time $\xi_\parallel$ depends exponentially on the correlation length $\xi_\perp$ at the infinite-randomness critical point of the spatially disordered contact process (See Eq. (16)), $\xi_\perp^{2/\nu_\perp}\xi_\parallel^{-1}$ vanishes as criticality is approached, $\xi_\perp \to \infty$. Thus, the infinite-randomness critical point is expected to be stable against weak temporal disorder. The same result also follows from Kinzel's inequality $z\nu > 2$ because z is formally infinite at the infinite-randomness critical point.

To study the stability of the infinite-noise critical point of the temporally disordered contact process against weak spatial disorder, we insert $G(x,t) \sim \delta(x)$ into Eq. (35). The l.h.s. then takes the form $\xi_\perp^{2/\nu_\perp - d}$ leading to the usual Harris inequality $d\nu_\perp > 2$. As the infinite-noise critical point features Kosterlitz-Thouless critical behavior with $\ln \xi_\perp \sim |r|^{-1/2}$, the exponent $\nu_\perp$ is formally infinite. This implies that weak spatial disorder is not a relevant perturbation at the infinite-noise critical point.

The generalized Harris criterion thus predicts that adding weak temporal disorder does not modify the critical behavior of the spatially disordered contact process and vice versa. This raises the interesting question of what happens if both disorders are of comparable strength. We will return to this question in Sec. 6.4.

6.2. ADDING WEAK SPATIAL DISORDER TO THE TEMPORAL DISORDERED CONTACT PROCESS

After the discussion of the generalized Harris criterion, we turn to computer simulation results. We start by adding weak spatial disorder to an already temporally disordered contact process. To this end, we simulate a sequence of systems with fixed strong temporal disorder, $p_t = 0.2$, $c_t = 0.05$ and $\Delta t = 6$ and increasing spatial disorder, $p = 0.2$, c varying from 1.0 to 0.05. The case of purely temporal disorder ($c = 1.0$) corresponds to the parameters studied in detail in Ref. [33]. Based on the generalized Harris criterion, we anticipate that the critical behavior for sufficiently weak spatial disorder remains identical to the pure temporal disorder case, albeit with a shift of the critical infection rate λ_c.

We therefore analyze the simulation data based on Eqs. (27) and (28). Figure 1 presents the inverse survival probability $1/P_s$ of spreading runs as a function of $\ln t$ for the weakest nonzero spatial disorder ($c = 0.8$). The figure shows that the data for $\lambda = 28.4$ follow the predicted logarithmic behavior (27) over almost five orders in magnitude in t. The data points with higher or lower λ curve away from the straight line as expected. We therefore identify $\lambda_c = 28.4$ as the critical value for $c = 0.8$. For comparison, the critical value for the case of purely temporal disorder is $\lambda_c = 27.27$ [33]. Figure 1 thus provides evidence that adding weak spatial disorder does not change the strong-noise critical behavior of the purely temporally disordered system.

To further confirm this, we test Eqs. (28) by analyzing the number of active sites N_s and the cloud radius R at criticality as functions of time in Fig. 2. To make the logarithmic corrections visible, we modify N_s and R by dividing out the leading term t. We then plot

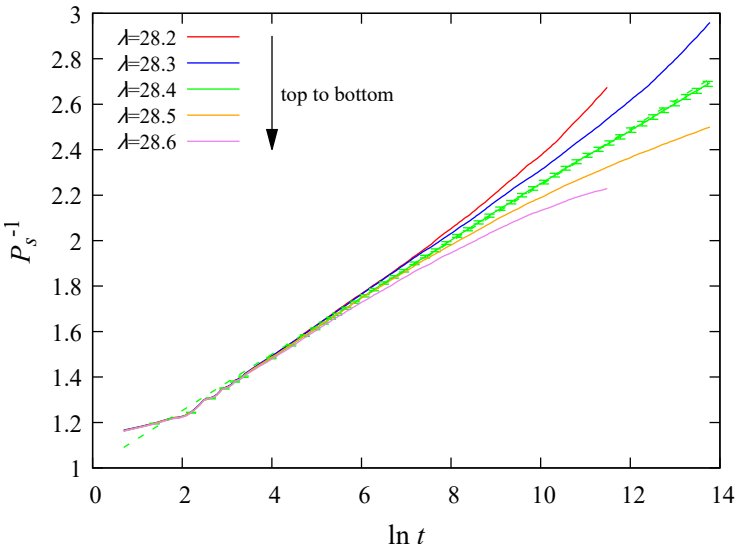

Figure 1. Inverse survival probability $1/P_s$ vs ln t close to criticality. The data are averages over 10000 to 20000 disorder configurations, with 5 runs per configuration ($p_t = 0.2$, $c_t = 0.05$, $\Delta t = 6$, $p = 0.2$ and $c = 0.8$). The statistical errors of every fifth data point of the critical curve are shown. The dashed line is a linear fit of the data from ln $t = 4.9$ to ln $t = 13.8$ (reduced $\chi^2 \approx 0.9$)

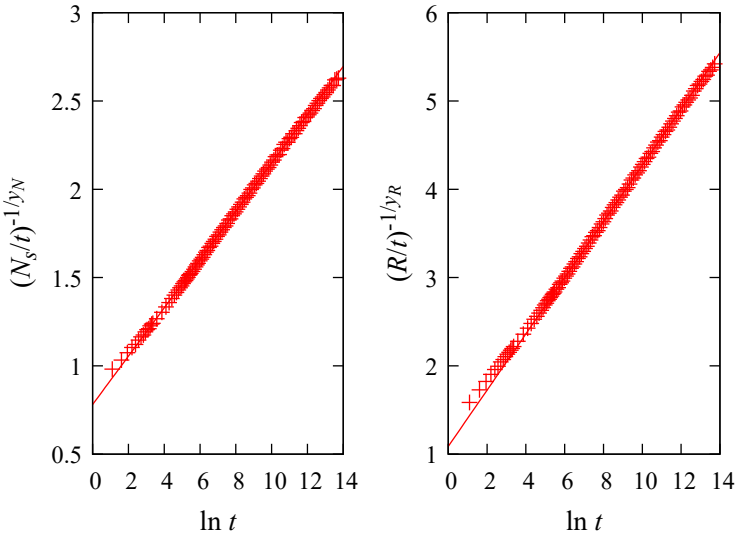

Figure 2. $(N_s/t)^{-1/y_N}$ and $(R/t)^{-1/y_R}$ vs ln t at criticality, $\lambda_c = 28.4$ for $p_t = 0.2$, $c_t = 0.05$, $\Delta t = 6$, $p = 0.2$ and $c = 0.8$. The data are averages over 20000 disorder configurations with 5 runs for each. The exponents $y_N = 3.6$ and $y_R = 1.7$ are fixed at the values found for purely temporal disorder [33]. The straight lines are fits of the data from ln $t = 6.5$ to ln t =13.8 with Eqs. (28).

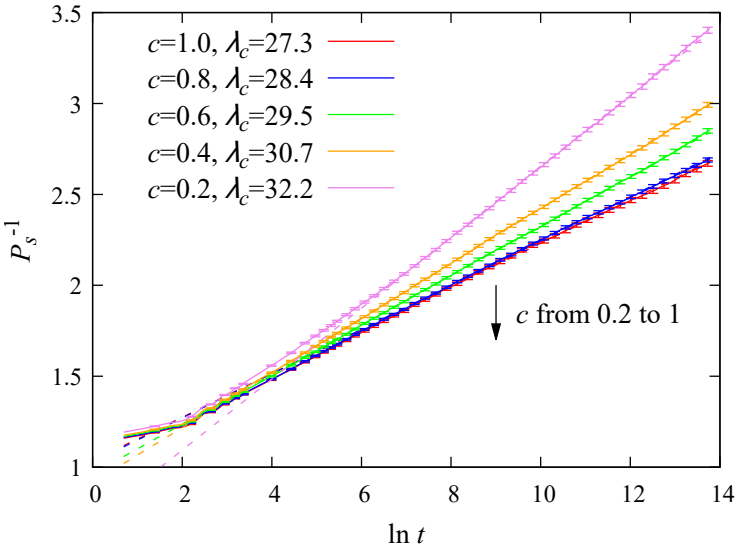

Figure 3. Inverse survival probability $1/P_s$ vs ln t at criticality for different c and $p_t = 0.2$, $c_t = 0.05$, $\Delta t = 6$, $p = 0.2$. The data are averages over 20000 disorder configurations with 5 runs for each. The statistical errors of every fifth data point is shown. The dashed lines are linear fits of the data.

$(N_s/t)^{-1/y_N}$ and $(R/t)^{-1/y_R}$ vs ln t, using the exponents $y_N = 3.6$ and $y_R = 1.7$ found for the case of purely temporal disorder [33]. The data follow straight lines, confirming that Eqs. (28) are also fulfilled.

Now, we extend the simulations to stronger spatial disorder (decreasing c towards 0). For $c = 0.6, 0.4$ and 0.2, the critical behavior can be fitted well with the infinite-noise functional forms Eqs. (27) and (28). This can be seem in Fig. 3 that shows the inverse survival probability as a function of ln t of the critical curves for $c = 1, 0.8, 0.6, 0.4$ and 0.2. All data follow straight lines for more than three orders of magnitude in t, confirming Eq. (27). The resulting values for λ_c are presented in Fig. 4. When the spatial disorder is further increased, the critical behavior deviates from the infinite-noise critical behavior (27) and (28). We will discuss this case in Sec. 6.4.

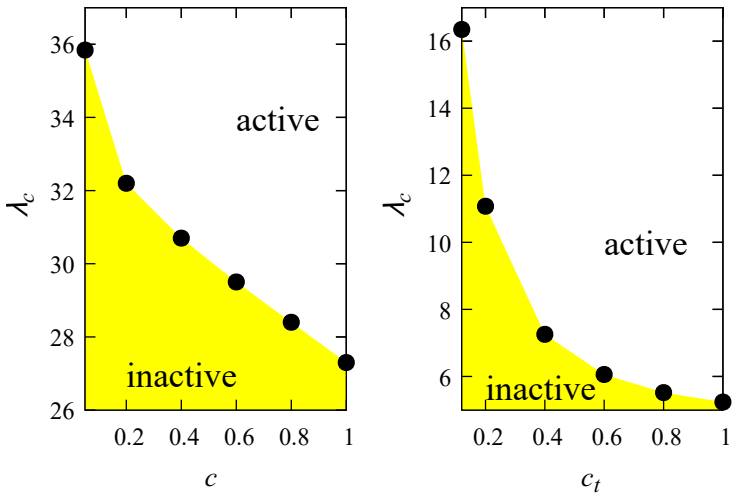

Figure 4. Left: Critical infection rate λ_c as a function of spatial disorder strength c for $p_t = 0.2$, $c_t = 0.05$, $p = 0.2$. Right: Critical λ_c as a function of temporal disorder strength c_t for $p = 0.3$, $c = 0.2$, $p_t = 0.2$.

6.3. ADDING WEAK TEMPORAL DISORDER TO SPATIAL DISORDER CASE

We now simulate a sequence of systems with fixed strong spatial disorder $p = 0.3$, $c = 0.2$, to which we add increasing temporal disorder with $p_t = 0.2$ and c_t varying from 1.0 to 0.12. The starting point of this sequence, the purely spatially disordered system with $c_t = 1$, corresponds to the parameters studied in Ref. [25].

For weak temporal disorder, $c_t = 0.8$, we anticipate the system to show the infinite-randomness critical behavior discussed in Sec. 3.2. This is tested in Figs. 5 and 6 which present the results of spreading simulations. Fig. 5 shows a plot of $P_s^{-1/\delta}$ vs ln t. The predicted critical behavior (21) corresponds to a straight line in this plot. The figure demonstrates that the data for $\lambda = 5.52$ follow (21) for almost five order of magnitude in t. This yields evidence for the infinite-randomness critical behavior. Similarly, Fig. 6 shows that the number of active sites sites N_s and the cloud radius R fulfill Eqs. (22) for almost four orders of magnitude in t. We conclude that the system is still controlled by infinite-randomness critical behavior.

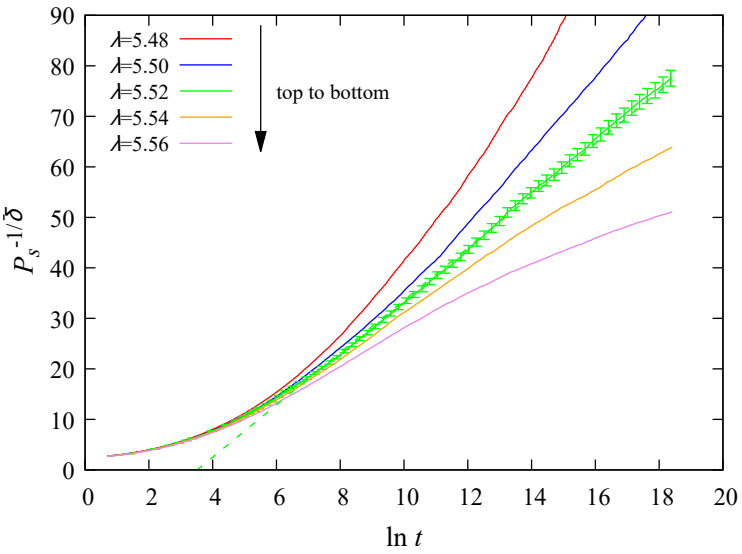

Figure 5. Survival probability vs time plotted as $P_s^{-1/\bar{\delta}}$ vs ln t close to criticality, where $\bar{\delta} = 0.38197$ ($p_t = 0.2$, $c_t = 0.8$, $\Delta t = 6$, $p = 0.3$ and $c = 0.2$). The data are averages over 700 disorder configurations with 100 runs per configuration. The statistical errors of every fifth data point of the critical curve are marked. The dashed line is a linear fit of the data for ln $t = 6.5$ to 18.4 (reduced $\chi^2 \approx 0.9$)

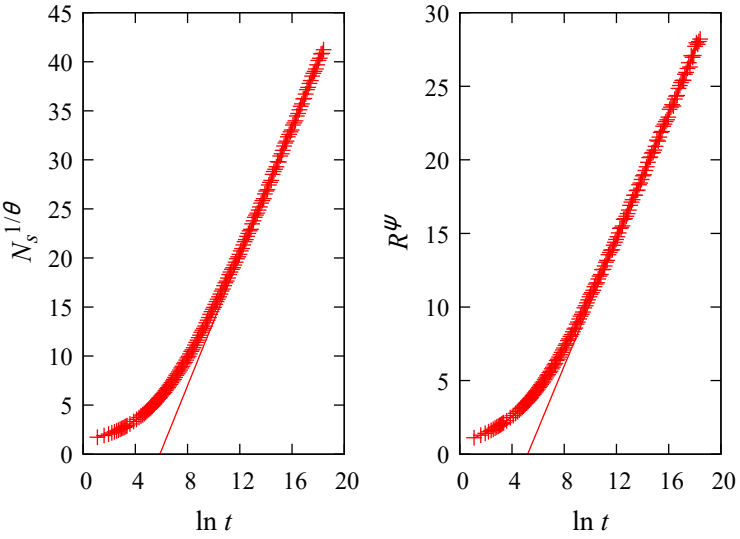

Figure 6. $(N_s)^{1/\Theta}$ and $(R)^{\psi}$ vs ln t at criticality $\lambda_c = 5.52$ for $p_t = 0.2$, $c_t = 0.8$, $\Delta t = 6$, $p = 0.3$, and $c = 0.2$. The data are averages over 700 disorder configurations with 100 runs per configuration. The values of the initial slip exponent Θ and the tunneling exponent ψ are fixed at the values of the infinite randomness critical point, $\Theta = 1.2360$, $\psi = 0.5$. The solid lines represents fits to Eqs. (22) from ln $t = 12.7$ to 18.4.

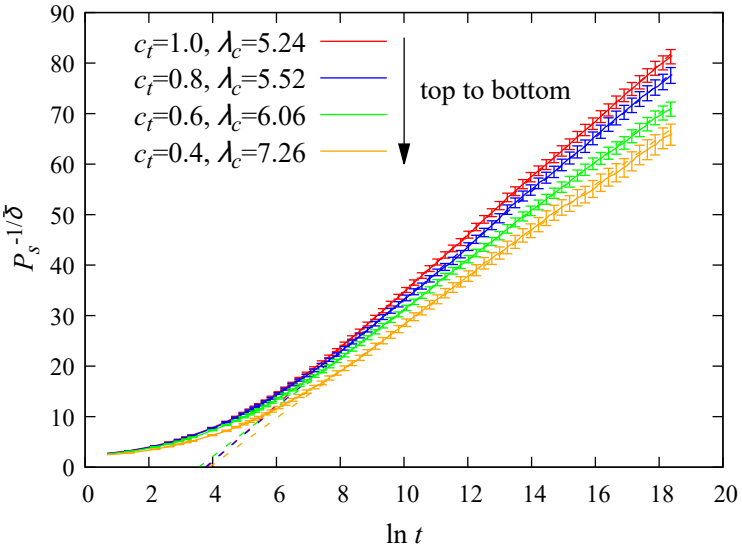

Figure 7. Survival probability vs time plotted as $P_s^{-1/\bar{\delta}}$ vs ln t at criticality for different c_t, where $\bar{\delta} = 0.38197$ ($p_t = 0.2$, $\Delta t = 6$, $p = 0.3$ and $c = 0.2$). The data are averages over 700 to 1000 disorder configurations with 30 to 100 runs for each. The statistical errors of every fifth data point are marked. The dashed lines are linear fits of the data.

We repeat this analysis for systems with stronger temporal disorder. For $c_t = 0.6$ and 0.4, we find that the critical behavior can be fitted well with the infinite-randomness expressions (21) and (22). This can be seen in Fig. 7, which shows $P_s^{-1/\delta}$ vs ln t at criticality for $c_t = 1, 0.8, 0.6, 0.4$. The data feature straight-line behavior for more than four orders of magnitude in t, confirming (22). The critical infection rates λ_c resulting from these simulations are shown in the phase diagram in Fig. 4.

For even stronger temporal disorder, the critical behavior deviates from the infinite-randomness criticality of Sec. 3.2, as will be discussed in the next section.

6.4. SPATIAL AND TEMPORAL DISORDER OF COMPARABLE STRENGTH

In Sec. 6.2, we have demonstrated that the infinite-noise critical point of the temporally disordered contact process is stable against the addition of weak spatial disorder. Analogously, the infinite-randomness critical point of the spatially disordered contact pro-

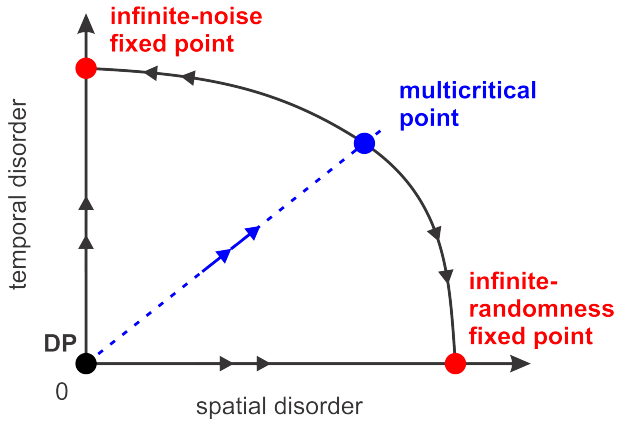

Figure 8. Schematic renormalization group flow on the critical manifold spanned by the spatial and temporal disorder strengths. (DP marks the direct percolation fixed point of the clean contact process.)

cess is stable against the addition of weak temporal disorder, as shown in Sec. 6.3. Since the infinite-noise and infinite-randomness critical behaviors differ qualitatively from each other, novel behavior is expected to emerge if the spatial and temporal disorders are of comparable strength.

The arguably simplest scenario corresponds to the schematic renormalization group flow diagram sketched in Fig. 8 which contains a multicritical point separating the infinite-noise and infinite-randomness regimes. If the ratio of the spatial and temporal disorder strengths is fine-tuned to be exactly on the separatrix (dashed line) in Fig. 8, the system flows to the multicritical point under coarse graining. The nonequilibrium phase transition then features novel multicritical behavior. If the system is not exactly on the dashed line, it will eventually flow either to the infinite-noise critical point or to the infinite-randomness critical point. However, if the system is close to (but not exactly on) the dashed line, it will flow towards the multicritical point for a long time before eventually approaching one of the other fixed points. This means the system will show multicritical behavior over a wide transient time interval before eventually crossing over to either infinite-randomness or infinite-noise critical behavior.

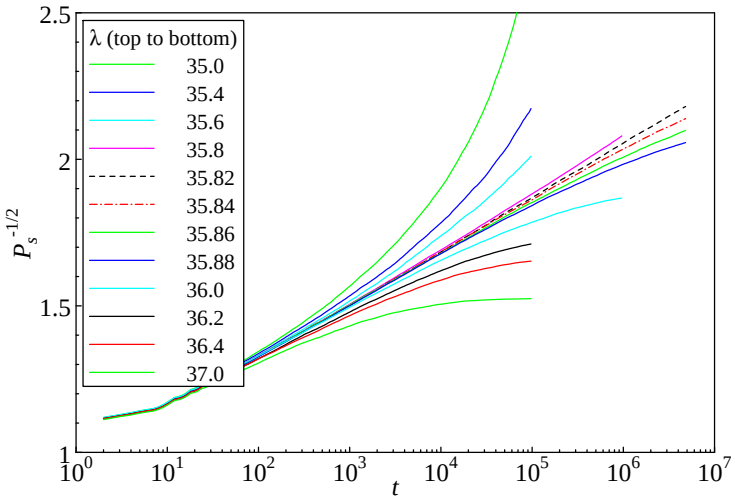

Figure 9. Survival probability vs time for $p_t = 0.2$, $c_t = 0.05$ $p = 0.2$, $c = 0.05$, and $\Delta t = 6$) The data are averages over 20000 disorder configurations with 5 runs per configuration.

Studying the regime where the spatial and temporal disorders are of comparable strength is extremely challenging numerically because the logarithmically slow dynamics makes it difficult to distinguish the asymptotic behavior from slow crossovers during the achievable simulation times. In the following, we demonstrate that our numerical data are compatible with the multi-critical point scenario. We emphasize however, that the unequivocal determination of the fate of the contact process in this regime is beyond our current computational capabilities.

To identify a multicritical system, we start from the sequence of systems studied in Sec. 6.2 and further increase the spatial disorder by reducing c, aiming at identifying a disorder strength for which the (asymptotic) critical behavior differs from both the infinite-randomness and the infinite-noise behavior. As the functional forms of the observables at the multicritical point are not known, we employ Dickman's [43] heuristic criterion of λ_c being the smallest λ supporting asymptotic growth of $N_s(t)$ to identify the phase transition. Figures 9 and 10 show that the system with $p_t = 0.2$, $c_t = 0.05$, $p = 0.2$, $c = 0.05$ approximately fulfills these conditions. The data at an infection rate of about 35.82 to

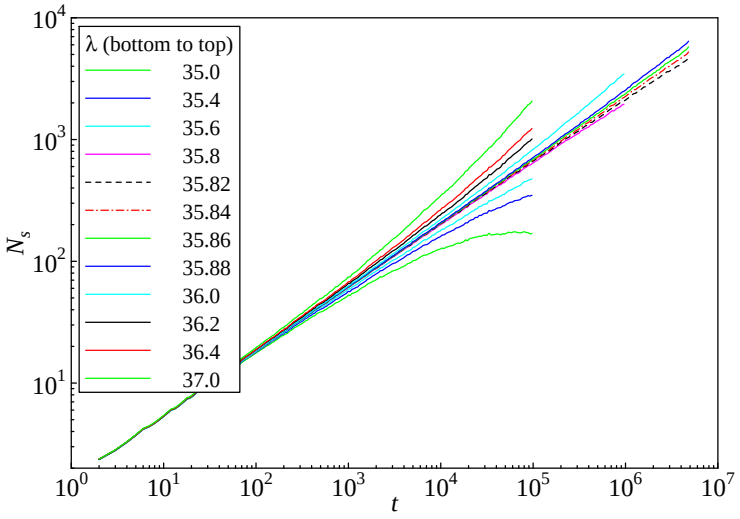

Figure 10. Number of active sites vs time for $p_t = 0.2$, $c_t = 0.05$ $p = 0.2$, $c = 0.05$, and $\Delta t = 6$) The data are averages over 20000 disorder configurations with 5 runs per configuration.

35.84 follow the functional forms

$$P_s \sim \ln^{-2}(t)\,, \qquad N_s \sim t^{\theta} \tag{36}$$

with $\theta \approx 0.5$ for almost six orders of magnitude in time. These functional forms differ from the behavior in the bulk phases as well as from the infinite-randomness and infinite-noise critical behaviors. This suggests that the parameters $p_t = 0.2$, $c_t = 0.05$, $p = 0.2$, $c = 0.05$ put the system very close to the separatrix in Fig. 8, and (36) approximately represents the multicritical behavior. Small deviations at late times can be attributed to the fact that the system is likely not exactly on the separatrix. To check the consistency of the analysis, we have confirmed that N_s/R behaves as $\ln^{-4}(t)$ as expected from the relation $N_s \sim P_s \rho R^d$.

The multicritical point can also be reached (approximately) by starting from the sequence of systems in Sec. 6.3 and further increasing the temporal disorder. The system with $p_t = 0.2$, $c_t = 0.12$, $p = 0.3$, $c = 0.2$ follows the same multicritical functional forms (36) at an infection rate of $\lambda \approx 16.35$.

It is interesting to note that the decay of P_s at the putative multicritical point, $P_s \sim \ln^{-2}(t)$ is faster than its decay at both the infinite-randomness critical point and the infinite-noise critical point (even though the P_s data are not compatible with an even faster power-law decay). This suggests that when the spatial and temporal disorders are of comparable strength, they weaken each other. The same phenomenon is also observed for the rare region effects and Griffiths singularities discussed in the next section.

7. RESULTS: RARE REGIONS AND GRIFFITHS SINGULARITIES

In this section, we discuss the effects of rare spatial regions and rare time intervals on the behavior of the contact process with the combined spatial and temporal disorder of the form $\lambda(x,t) = \lambda_0 f(x) g(t)$.

7.1. THEORY

Consider a spatial rare region with an above average $f(x)$. This region can be locally in the active phase even if the bulk system is still inactive. If f follows the binary distribution (33), the strongest rare regions consist of sites with $f = 1$ only. As in Sec. 4.1, the probability for finding such a region rare is given by $w(L_{RR}) \sim \exp(-bL_{RR}^d)$ (up to pre-exponential factors). However, the behavior of the lifetime $\tau(L_{RR})$ of such a region depends on the strength of the temporal disorder. If the temporal disorder is sufficiently weak such that the rare region is locally active for all times, $\tau(L_{RR}) \sim \exp(aL_{RR}^d)$ as in the case of purely spatial disorder. For stronger temporal disorder, in contrast, the rare region will still be mostly active, but inactive during rare time intervals. In this case, the lifetime $\tau(L_{RR})$ depends on L_{RR} via the power law $\tau(L_{RR}) \approx (aL_{RR}^d)^y$, as shown in Sec. 4.2.

Inserting $\tau(L_{RR})$ in (29) yields the following anomalous density decay in the Griffiths phase on the inactive side of the transition:

$$\rho(t) \sim t^{-b/a} = t^{-d/z'} \quad \text{weak temporal disorder ,} \tag{37}$$

$$\rho(t) \sim \exp(-bt^{1/y}/a) \quad \text{strong temporal disorder .} \tag{38}$$

The survival probability $P_s(t)$ in spreading runs behaves in the same manner as $\rho(t)$. Thus, for sufficiently strong temporal disorder, the power-law Griffiths singularities are weakened and replaced by stretched exponential behavior. The exponent y is non-universal and depends on how far in the inactive phase a rare region is during the "bad" (low $g(t)$) time periods. $1/y$ is expected to decrease to zero as the transition is approached from the inactive side.

Analogous arguments can be made for the Griffiths singularity in the lifetime τ_L of a finite-size system on the active side of the phase transition. Consider a system globally in the active phase. Temporal disorder can produce rare time intervals during which the system is temporarily on the inactive side of the transition. For the binary distribution (34), the strongest rare time intervals have $g(t) \equiv c_t$. The probability of finding such time intervals depends exponentially on their lengths, $w(T_{RR}) \sim \exp(-bT_{RR})$, as in Sec. 4.2. However, the time evolution of the density of active sites during these rare time intervals depends on the strength of the spatial disorder. For weak spatial disorder, the entire system will be in the inactive phase during these intervals, leading to an exponential density decay, $\rho \sim \exp(-at)$, as in the case of purely temporal disorder. For stronger spatial disorder, the system will have spatial regions that remain locally active during the rare time interval, leading to a slower power-law decay of the density $\rho \sim (at)^{-y}$,

Repeating the analysis of Sec. 4.2 for these two cases, we conclude that the life time τ of a finite-size system behaves as

$$\tau(L) \sim L^{db/a} = L^{d/\kappa} \quad \text{weak spatial disorder}, \tag{39}$$

$$\tau(L) \sim \exp(bL^{d/y}/a) \quad \text{strong spatial disorder} \tag{40}$$

with system size L in the Griffiths phase on the active side of the transition. This means for sufficiently strong spatial disorder, the power-law temporal Griffith singularities of Sec. 4.2 are weakened and replaced by stretched exponentials.

Note that the functional forms (38) and (40) have been derived assuming that the relevant rare regions and rare time intervals are uniform in space and time, respectively. This is justified for bounded disorder for which the strongest spatial rare regions have $f(x) \equiv f_{max}$ and the strongest rare time intervals have $g(t) \equiv g_{min}$. The asymptotic behavior of ρ and P_s for $t \to \infty$ is governed by the strongest rare regions and thus given by (38). Along the same lines, the asymptotic behavior of $\tau(L)$ for $L \to \infty$ is governed by the strongest rare time intervals and thus given by (40). The preasymptotic behavior has contributions from nonuniform rare regions that feature more complicated behavior, leading to nontrivial crossovers.

7.2. SIMULATION RESULTS

We first consider the survival probability P_s on the inactive side of the transition. To test the power-law Griffiths behavior (37), we consider a system with strong spatial disorder but weak temporal disorder ($p = 0.3$, $c = 0.2$, $p_t = 0.2$, $c_t = 0.8$ and $\Delta t = 6$). Figure 11 presents a double-log plot of P_s vs. t for several λ below the critical value $\lambda_c \approx 5.52$. The data indicate that the survival probability follows (37) for all shown $\lambda \geq 4.3$. Moreover, the

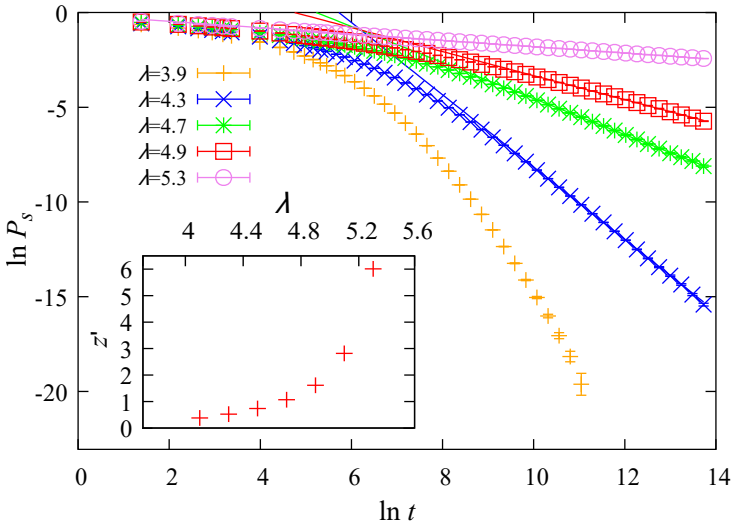

Figure 11. Main panel: ln P_s vs ln t for different λ below criticality $\lambda_c \approx 5.52$ for $p = 0.3$, $c = 0.2$, $p_t = 0.2$, $c_t = 0.8$ and $\Delta t = 6$. The data are averages over 1000 to 10000 disorder configurations with 100 to 10^5 runs per configuration. The solid lines are fits to (37). Inset: Resulting Griffiths exponent z' as a function of the infection rate λ.

Griffiths dynamical exponent z' diverges as the critical infection rate λ_c is approached, in agreement with the behavior for purely spatial disorder. For $\lambda = 3.9$, in contrast, the data continue to curve downward to the longest times.

To explain these results, consider the strongest spatial rare regions which consist of sites with $f \equiv 1$ only. The local infection rate on such a rare region is thus either λ or $c_t\lambda = 0.8\times\lambda$. For infections rates $\lambda > \lambda_c^0/c_t = 4.122$ (where $\lambda_c^0 = 3.298$ is the clean critical infection rate), the strongest rare regions are thus always on the active side of the clean critical point, explaining the power-law form of the Griffiths singularity. For $\lambda < \lambda_c^0/c_t$ the rare regions become inactive during the "bad" (low $g(t)$) time intervals, leading to a crossover from the power-law decay (37) to the stretched exponential decay (38).

To explore the novel stretched exponential Griffiths behavior (38) in more detail, we study a system with stronger temporal disorder, $c_t = 0.4$ rather than 0.8. The other parameters remain unchanged ($p = 0.3$, $c = 0.2$, $p_t = 0.2$, and $\Delta t = 6$). The critical infection rate for these parameters is $\lambda_c \approx 7.26$. To cover the entire (inactive) Griffiths

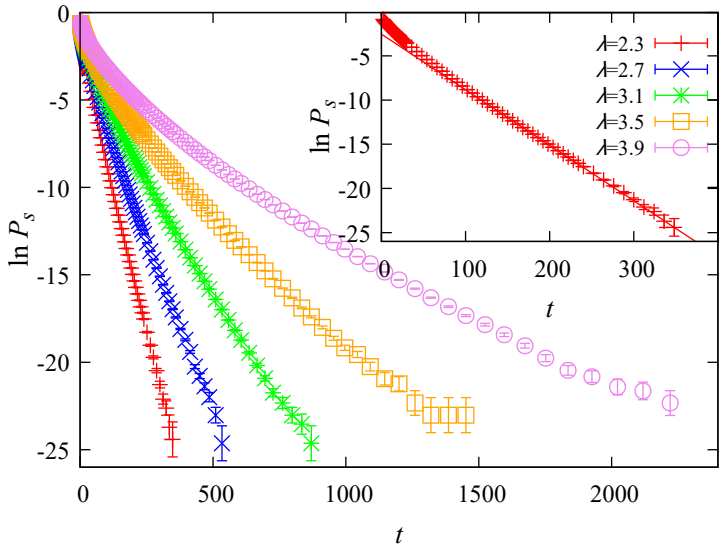

Figure 12. Main panel: $\ln P_s$ vs t for different λ between 2.3 and 3.9, far from criticality $\lambda_c \approx 7.26$ for $p = 0.3$ and $c = 0.2$, $p_t = 0.2$, $c_t = 0.4$ and $\Delta t = 6$). The data are averages over at least than 10^5 disorder configurations with 10^5 runs each. Inset: Enlarged plot for $\lambda = 2.3$; the linear fit (solid line) confirms a simple exponential decay.

phase, we perform simulations for infection rates ranging from 2.3 (below the clean critical value λ_c^0) to 6.9 close to the phase transition. A semi-log plot of the survival probability for infection rates between 2.3 and 3.9 is shown in Fig. 12. For λ below the clean critical value $\lambda_c^0 = 3.298$, the survival probability features a simple exponential decay, as expected in the conventional inactive phase in which there are no locally active rare regions. For $\lambda > \lambda_c^0$, the system enters the Griffiths phase, and the decay of P_s becomes slower than exponential. However, as is demonstrated via the double-log plot of P_s vs t in Fig. 13(a), the decay for all λ in the (inactive) Griffiths phase is faster than a power law. In fact, all data can be fitted very well with the stretched exponential form (38), as shown in Fig. 13(b) which replots the same data in the form $\ln P_s$ vs $t^{1/y}$ with y chosen such that the data fall onto straight lines. The resulting values of the exponent $1/y$ governing the stretched exponential evolve from unity at the clean critical infection rate λ_c^0 towards zero at the phase transition. Note that even the strongest rare regions ($f \equiv 1$) will be inactive during the "bad" time

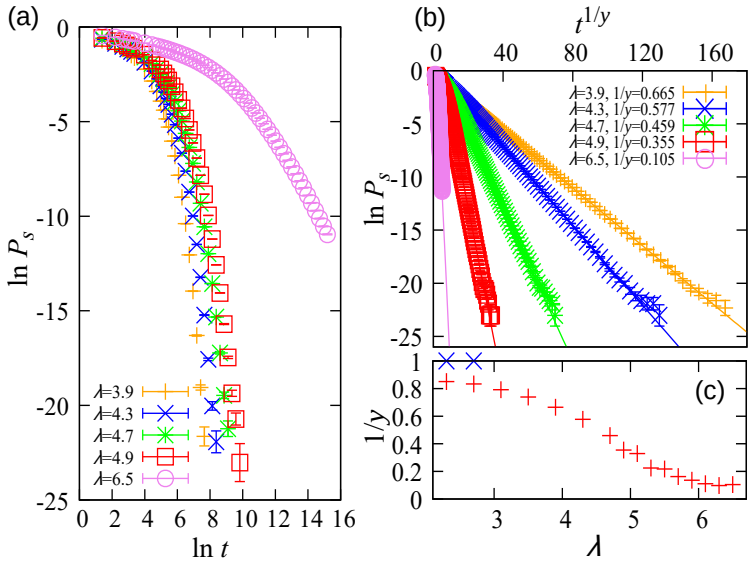

Figure 13. (a) $\ln P_s$ vs $\ln t$ for different λ below criticality $\lambda_c \approx 7.26$ for $p = 0.3$, $c = 0.2$, $p_t = 0.2$, $c_t = 0.4$ and $\Delta t = 6$). The data are averages over 10^4 to 10^5 disorder configurations with 10^4 to 10^5 runs per configuration. (b) $\ln P_s$ vs $t^{1/y}$ for the same data. The solid lines are linear fits. (c) Exponent $1/y$ of the stretched exponential (38) vs λ. For $\lambda < \lambda_c^0$, the data can be fitted well with $y = 1$, as expected in the conventional inactive phase even though an unrestricted fit yields $1/y$ values slightly below unity.

intervals everywhere in the Griffiths phase because $c_t\lambda_c < \lambda_c^0$. This explains why the decay of the survival probability takes the stretched exponential form for all infection rates with $\lambda_c^0 < \lambda < \lambda_c$.

We now turn to the behavior of the lifetime of a finite-size system on the active side of the transition. The goal is to test wether the power-law temporal Griffiths behavior (39) gets replaced by the stretched exponential (40) if sufficiently strong spatial disorder is added to the temporally disordered contact process. Figure 14(a) shows a double log plot of the lifetime vs system size for $p = 0.3$, $c = 0.2$, $p_t = 0.2$, $c_t = 0.2$, and $\Delta t = 6$ at infection rates slightly above the critical value $\lambda_c \approx 11.08$. The figure demonstrates that the increase is faster than a power law. The same data are replotted in Fig. 14(b) in the form $\ln \tau$ vs

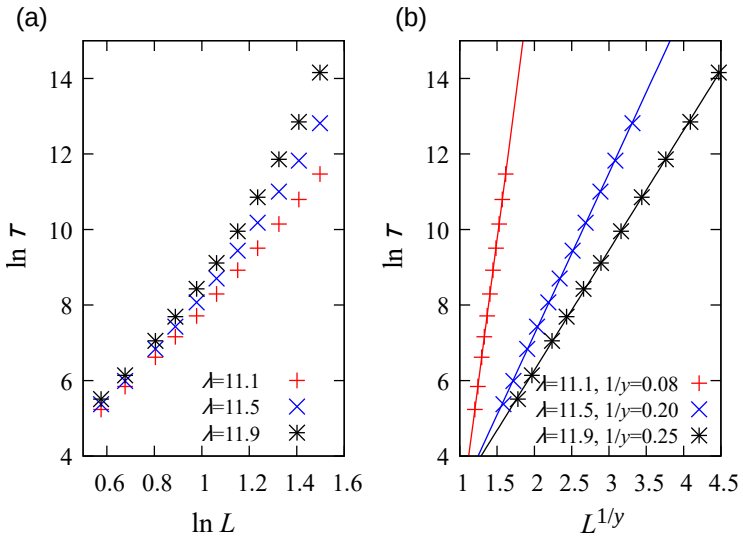

Figure 14. (a) Double-log plot of lifetime τ vs system size L for different λ above criticality $\lambda_c \approx 11.08$ for $p = 0.3$, $c = 0.2$, $p_t = 0.2$, $c_t = 0.2$ and $\Delta t = 6$. The data are determined from decay runs, averaged over 10240 disorder configurations (one run per configuration). (b) The same data plotted as $\ln \tau$ vs $L^{1/y}$, with y chosen such that the data fall onto straight lines.

$L^{1/y}$ motivated by Eq. (40). For properly chosen y-values, all data fall onto straight lines, confirming that the lifetime follows the stretched exponential Griffiths behavior (40). The exponent $1/y$ increases with increasing distance from criticality, as expected.

8. CONCLUSIONS

In summary, we have investigated the combined influence of spatial and temporal random disorder on the absorbing-state phase transition in the one-dimensional contact process. Specifically, we have studied the case of decoupled spatial and temporal disorders for which the local infection rates $\lambda(x,t)$ are the product of a purely spatial term and a purely temporal term, $\lambda(x,t) = \lambda_0 f(x) g(t)$. In contrast to completely uncorrelated spatiotemporal randomness, such disorder which contains infinite-range correlations in space and time is a relevant perturbation at the clean DP critical point.

We have employed a generalization of the Harris criterion [17] to predict that the infinite-randomness critical point of the spatially disordered contact process is stable against weak temporal disorder. Analogously, the criterion predicts that the infinite-noise critical point of the temporally disorder contact process is stable against weak spatial disorder. We have confirmed these predictions by extensive computer simulations. In the interesting parameter region where both disorders are of comparable strength, the critical behavior appears to differ from both the infinite-randomness and infinite-noise critical behaviors. Our simulation data are compatible with the simplest scenario in which a single multicritical point separates the infinite-randomness and infinite-noise regimes. However, due to the very slow dynamics of the contact process in the presence of both disorders, we cannot exclude more complicated scenarios that involve novel critical behavior in an extended parameter region. In the absence of theoretical predictions, the complete quantitative understanding of the (multi)critical behavior from simulations would require simulation times several orders of magnitude larger than what is achievable today. This problem thus remains a task for the future.

In addition to the nonequilibrium phase transition itself, we have also investigated the effects of rare regions and rare time intervals in the Griffiths phases near the transition. By means of optimal fluctuation arguments, we have shown that adding weak temporal disorder does not change the power-law Griffiths behavior of the density and survival probability of the spatially disordered contact process on the inactive side of the transition (at least sufficiently close to the transition). Stronger temporal disorder, in contrast, weakens the "spatial" Griffiths singularity in the density and survival probability, replacing the slow power-law decay with a faster stretched exponential. The behavior of the lifetime as a function of system size in the "temporal" Griffiths phase on the active side of the transition is completely analogous. Adding weak spatial disorder to the temporally disordered contact process does not change the power-law Griffiths behavior but sufficiently strong spatial disorder weakens the singularity from power-law to stretched exponential behavior. The

notion that the spatial and temporal disorders weaken each other is also consistent with the observation that the decay of the survival probability with time at the putative multicritical point is faster than the decay at either the infinite-randomness critical point or the infinite-noise critical point.

Our explicit computer simulation results are for one space dimension. However, the stability arguments based on the generalized Harris criterion apply equally to one, two, and three space dimensions. The same applies to the optimal fluctuation arguments governing the Griffiths singularities. We therefore expect most of our qualitative results to carry over from one to two and three space dimensions.

Clearcut experimental examples of absorbing-state transitions were missing for a long time [44]. By now, such transitions have been observed, however, in turbulent liquid crystals [6], driven suspensions [7, 8], growing bacteria colonies [9, 10], and in the dynamics of superconducting vortices [11]. Studying these systems under the combined influence of spatial disorder and external noise will permit experimental tests of our results. The influence of environmental fluctuations and inhomogeneities on the extinction of a biological population are attracting considerable attention today in the contexts of both epidemic spreading and of global warming and other large-scale environmental changes (see, e.g., Ref. [45]). In the laboratory, these questions could be analyzed, e.g., by growing bacteria or yeast populations in spatially inhomogeneous environments and fluctuating external conditions.

ACKNOWLEDGEMENTS

This work has been supported in part by the National Science Foundation under Grant Nos. DMR-1828489 and OAC-1919789. The simulations were performed on the Pegasus and Foundry clusters at Missouri S&T.

REFERENCES

[1] J. Marro and R. Dickman. *Nonequilibrium Phase Transitions in Lattice Models*. Cambridge University Press, Cambridge, 1999.

[2] H. Hinrichsen. Nonequilibrium critical phenomena and phase transitions into absorb-ing states. *Adv. Phys.*, 49:815, 2000. doi: 10.1080/00018730050198152.

[3] G. Odor. Universality classes in nonequilibrium lattice systems. *Rev. Mod. Phys.*, 76: 663, 2004. doi: 10.1103/RevModPhys.76.663.

[4] M. Henkel, H. Hinrichsen, and S. Lübeck. *Non-equilibrium phase transitions. Vol 1: Absorbing phase transitions*. Springer, Dordrecht, 2008.

[5] Uwe C. Täuber. *Critical dynamics*. Cambridge University Press, Cambridge, 2014.

[6] Kazumasa A. Takeuchi, Masafumi Kuroda, Hugues Chaté, and Masaki Sano. Directed percolation criticality in turbulent liquid crystals. *Phys. Rev. Lett.*, 99:234503, Dec 2007. doi: 10.1103/PhysRevLett.99.234503. URL http://link.aps.org/doi/10.1103/PhysRevLett.99.234503.

[7] L. Corte, P. M. Chaikin, J. P. Gollub, and D. J. Pine. Random organization in periodically driven systems. *Nature Physics*, 4:420, 2008. doi: 10.1038/ nphys891.

[8] Alexandre Franceschini, Emmanouela Filippidi, Elisabeth Guazzelli, and David J. Pine. Transverse alignment of fibers in a periodically sheared suspension: An absorb-ing phase transition with a slowly varying control parameter. *Phys. Rev. Lett.*, 107: 250603, Dec 2011. doi: 10.1103/PhysRevLett.107.250603.

[9] K. S. Korolev and David R. Nelson. Competition and cooperation in one-dimensional stepping-stone models. *Phys. Rev. Lett.*, 107: 088103, Aug 2011. doi: 10.1103/PhysRevLett.107.088103. URL http://link.aps.org/doi/10.1103/PhysRevLett.107.088103.

[10] K. S. Korolev, Joao B. Xavier, David R. Nelson, and Kevin R. Foster. A quantitative test of population genetics using spatiogenetic patterns in bacterial colonies. *The American Naturalist*, 178:538, 2011. doi: 10.1086/661897.

[11] S. Okuma, Y. Tsugawa, and A. Motohashi. Transition from reversible to irreversible flow: Absorbing and depinning transitions in a sheared-vortex system. *Phys. Rev. B*, 83:012503, Jan 2011. doi: 10.1103/PhysRevB.83.012503.

[12] H. K. Janssen. *Z. Phys. B*, 42:151, 1981. doi: 10.1007/BF01319549.

[13] P. Grassberger. *Z. Phys. B*, 47:365, 1982. doi: 10.1007/BF01313803.

[14] P. Grassberger and A. de la Torre. *Ann. Phys. (NY)*, 122:373, 1979. doi: 10.1016/0003-4916(79)90207-0.

[15] A. B. Harris. Effect of random defects on the critical behaviour of Ising models. *J. Phys. C*, 7:1671, 1974. doi: 10.1088/0022-3719/7/9/009.

[16] W. Kinzel. Phase transitions of cellular automata. *Z. Phys. B*, 58:229, 1985. doi: 10.1007/BF01309255.

[17] Thomas Vojta and Ronald Dickman. Spatiotemporal generalization of the harris criterion and its application to diffusive disorder. *Phys. Rev. E*, 93:032143, Mar 2016. doi: 10.1103/PhysRevE.93.032143.

[18] J. Hooyberghs, F. Iglói, and C. Vanderzande. Strong-disorder fixed point in absorbing-state phase transitions. *Phys. Rev. Lett.*, 90:100601, 2003. doi: 10.1103/Phys-RevLett.90.100601.

[19] J. Hooyberghs, F. Iglói, and C. Vanderzande. Absorbing state phase transitions with quenched disorder. *Phys. Rev. E*, 69:066140, 2004. doi: 10.1103/Phys-RevE.69.066140.

[20] S. K. Ma, C. Dasgupta, and C. K. Hu. Random antiferomagnetic chain. *Phys. Rev. Lett.*, 43:1434, 1979.

[21] F. Igloi and C. Monthus. Strong disorder renormalization group approach of random systems. *Phys. Rep.*, 412:277, 2005.

[22] R. B. Griffiths. Nonanalytic behavior above the critical point in a random Ising ferromagnet. *Phys. Rev. Lett.*, 23:17, 1969. doi: 10.1103/PhysRevLett.23.17.

[23] André J. Noest. New universality for spatially disordered cellular automata and directed percolation. *Phys. Rev. Lett.*, 57:90–93, Jul 1986. doi: 10.1103/PhysRevLett.57.90. URL http://link.aps.org/doi/10.1103/PhysRevLett.57.90.

[24] André J. Noest. Power-law relaxation of spatially disordered stochastic cellular automata and directed percolation. *Phys. Rev. B*, 38: 2715–2720, Aug 1988. doi: 10.1103/PhysRevB.38.2715. URL http://link.aps.org/doi/10.1103/PhysRevB.38.2715.

[25] T. Vojta and M. Dickison. Critical behavior and Griffiths effects in the disordered contact process. *Phys. Rev. E*, 72:036126, 2005. doi: 10.1103/PhysRevE.72.036126.

[26] M. M. de Oliveira and S. C. Ferreira. Universality of the contact process with random dilution. *J. Stat. Mech.*, 2008:P11001, 2008.

[27] T. Vojta, A. Farquhar, and J. Mast. Infinite-randomness critical point in the two-dimensional disordered contact process. *Phys. Rev. E*, 79:011111, 2009. doi: 10.1103/PhysRevE.79.011111.

[28] Thomas Vojta. Monte carlo simulations of the clean and disordered contact pro-cess in three dimensions. *Phys. Rev. E*, 86:051137, Nov 2012. doi: 10.1103/Phys-RevE.86.051137.

[29] Thomas Vojta and Man Young Lee. Nonequilibrium phase transition on a ran-domly diluted lattice. *Phys. Rev. Lett.*, 96:035701, Jan 2006. doi: 10.1103/Phys-RevLett.96.035701.

[30] Man Young Lee and Thomas Vojta. Absorbing-state phase transitions on percolating lattices. *Phys. Rev. E*, 79:041112, Apr 2009. doi: 10.1103/PhysRevE.79.041112. URL http://link.aps.org/doi/10.1103/PhysRevE.79.041112.

[31] Hatem Barghathi, David Nozadze, and Thomas Vojta. Contact process on generalized fibonacci chains: Infinite-modulation criticality and double-log periodic oscillations. *Phys. Rev. E*, 89:012112, Jan 2014. doi: 10.1103/PhysRevE.89.012112.

[32] Thomas Vojta and José A. Hoyos. Infinite-noise criticality: Nonequilibrium phase transitions in fluctuating environments. *EPL (Europhysics Letters)*, 112(3):30002, 2015. doi: 10.1209/0295-5075/112/30002.

[33] Hatem Barghathi, Thomas Vojta, and José A. Hoyos. Contact process with temporal disorder. *Phys. Rev. E*, 94:022111, Aug 2016. doi: 10.1103/PhysRevE.94.022111.

[34] Hatem Barghathi, Skye Tackkett, and Thomas Vojta. Extinction phase transitions in a model of ecological and evolutionary dynamics. *Eur. Phys. J. B*, 90:129, 2017. doi: 10.1140/epjb/e2017-80220-7.

[35] Federico Vazquez, Juan A. Bonachela, Cristóbal López, and Miguel A. Muñoz. Temporal griffiths phases. *Phys. Rev. Lett.*, 106:235702, Jun 2011. doi: 10.1103/Phys-RevLett.106.235702.

[36] T. E. Harris. Contact interactions on a lattice. *Ann. Prob.*, 2:969, 1974. doi: doi:10.1214/aop/1176996493.

[37] I. Jensen. Low-density series expansions for directed percolation: I. a new efficient algorithm with applications to the square lattice. *J. Phys. A*, 32:5233, 1999.

[38] Daniel S. Fisher. Random transverse field ising spin chains. *Phys. Rev. Lett.*, 69: 534–537, Jul 1992. doi: 10.1103/PhysRevLett.69.534.

[39] D. S. Fisher. Critical behavior of random transverse-field Ising spin chains. *Phys. Rev. B*, 51:6411, 1995. doi: 10.1103/PhysRevB.51.6411.

[40] J. M. Kosterlitz and D. J. Thouless. *J. Phys. C*, 6:1181, 1973.

[41] T. Vojta. Rare region effects at classical, quantum, and non-equilibrium phase transi-tions. *J. Phys. A*, 39:R143, 2006. doi: 10.1088/0305-4470/39/22/R01.

[42] Ronald Dickman. Reweighting in nonequilibrium simulations. *Phys. Rev. E*, 60:R2441–R2444, Sep 1999. doi: 10.1103/PhysRevE.60.R2441. URL https://link.aps.org/doi/10.1103/PhysRevE.60.R2441.

[43] A. G. Moreira and R. Dickman. Critical dynamics of the contact process with quenched disorder. *Phys. Rev. E*, 54:R3090, 1996.

[44] H. Hinrichsen. On possible experimental realizations of directed percolation. *Braz. J. Phys.*, 30:69, 2000.

[45] Otso Ovaskainen and Baruch Meerson. Stochastic models of population extinction. *Trends in Ecology & Evolution*, 25:643 – 652, 2010. doi: http://dx.doi.org/10.1016/j.tree.2010.07.009.

III. UNCONVENTIONAL JOSEPHSON JUNCTIONS WITH TOPOLOGICAL KONDO INSULATOR WEAK LINKS

Xuecheng Ye

Department of Physics and Materials Research Center, Missouri University of Science and Technology, Rolla, MO 65409

Jacob Cook

Department of Physics and Materials Research Center, Missouri University of Science and Technology, Rolla, MO 65409

Erik D. Huemiller

Department of Physics and Materials Research Laboratory, University of Illinois at Urbana-Champaign, Urbana, Illinois 61801

Aaron D. K. Finck

IBM T. J. Watson Research Center, Yorktown Heights, NY 10598

Pouyan Ghaemi

Physics Department, City College of the City University of New York, New York, NY 10031

Thomas Vojta

Department of Physics, Missouri University of Science and Technology, Rolla, MO 65409

Vivekananda Adiga

IBM T. J. Watson Research Center, Yorktown Heights, NY 10598

Shanta R. Saha

Department of Physics, University of Maryland, College Park, MD

Johnpierre Paglione

Department of Physics, University of Maryland, College Park, MD

Cihan Kurter

Current Affiliation: IBM T. J. Watson Research Center, Yorktown Heights, NY 10598

Department of Physics and Materials Research Center, Missouri University of Science and Technology, Rolla, MO 65409

ABSTRACT

Proximity-induced superconductivity in three dimensional (3D) topological insulators forms a new quantum phase of matter and accommodates exotic quasiparticles such as Majorana bound states. One of the biggest drawbacks of the commonly studied 3D topological insulators is the presence of conducting bulk that obscures both surface states and low energy bound states. Introducing superconductivity in topological Kondo insulators such as SmB_6, however, is promising due to their true insulating bulk at low temperatures. In this work, we develop an unconventional Josephson junction by coupling superconducting Nb leads to the surface states of a SmB_6 crystal. We observe a robust critical current at low temperatures that responds to the application of an out-of-plane magnetic field with significant deviations from usual Fraunhofer patterns. The appearance of Shaphiro steps under microwave radiation gives further evidence of a Josephson effect. Moreover, we explore the effects of Kondo breakdown in our devices, such as ferromagnetism at the surface and anomalous temperature dependence of supercurrent. Particularly, the magnetic diffraction patterns show an anomalous hysteresis with the field sweep direction suggesting the coexistence of magnetism with superconductivity at the SmB_6 surface. The experimental work will advance the current understanding of topologically nontrivial superconductors and emergent states associated with such unconventional superconducting phases.

PACS numbers: 85.25.Dq; 74.45.+c; 74.90.+n

1. INTRODUCTION

Topological superconductivity [1] is expected to be a unique platform to generate and manipulate zero energy modes, referred to as Majorana bound states [2, 3, 4, 5, 6, 7]. One way to get a topological superconductor is engineering Josephson junctions on the surfaces of 3D topological insulators [8, 9, 10, 11, 12, 13, 14, 15, 16, 17]. In such devices, the quantum interference of electron and hole-like excitations will form low energy Andreev bound states whose spectrum is sensitive to the relative phase difference between the superconducting leads and the microscopic details of the barrier. Proximity-induced supercurrent flowing through the topological insulator segment of the junction is carried by such states.

Initially, Josephson junctions incorporating Bi-based 3D topological insulators were favored for experimental searches for signatures of Majorana modes. However, significant bulk and trivial surface state contribution to the electronic transport complicated the interpretation of such experiments. Although electrostatic gating can alleviate the problem [16, 18, 19], the quest for finding a proper platform for such modes is still ongoing.

Topological Kondo insulators [20, 21] such as SmB_6 are promising candidates for solving the problems caused by trivial transport channels. At high temperatures, these materials are metallic with a dense array of magnetic moments from f-electrons. However, at sufficiently low temperatures, such moments strongly couple to conduction electrons leading to the formation of singlets. This hybridization opens up a narrow gap in the electronic band structure [22]. Point contact tunneling measurements confirmed the formation of such a gap below 60 K [23]. At even lower temperatures (below 3-5 K), an anomalous saturation of sample resistance was observed [24], which has been attributed to the presence of topological surface states [25, 26, 27]. Recent low temperature transport studies with SmB_6 have revealed various anomalies such as thickness independence of Hall voltage, suggesting that transport is dominated by surface states [28]. There has been an evidence of helical nature of such states based on electrical detection of surface spin polarization [29].

Moreover, the observation of a perfect Andreev reflection in a Au-SmB_6/YB_6 structure has been claimed due to the topologically protected surface states as well as the absence of a bulk conduction channel [30]. In addition, photoemission [31] and STM [32] studies supported the presence of in-gap surface states that are topologically protected.

2. EXPERIMENTAL

We studied a set of single lateral Josephson junctions on the surface of mechanically polished SmB_6 crystals. In this paper we will show results from four different junctions labelled as junction-1 through junction-4. The junction lengths vary from 50 nm to 200 nm. The cubic crystal structure of SmB_6 does not permit exfoliation to obtain atomically thin flakes. Here, the entire circuit of the devices (junctions and contact leads/pads) is fabricated on the surface of the mechanically polished single crystals.

An SEM picture of one of the studied devices, junction-1 is shown in Fig. 1(a). Two superconducting Nb leads that are about 100 nm apart have been defined by electron beam lithography and $\sim$ 60-70 nm Nb deposition via magnetron sputtering. Prior to Nb deposition an in-situ Ar milling was applied to lightly etch the top surface of the crystal and to ensure good interface between SmB_6 and the superconductor.

All of our devices were thermally anchored to the mixing chamber of a cryogen-free dilution refrigerator with a base temperature of 10 mK and equipped with filtered wiring. The transport measurements were done with standard lock-in techniques at different temperatures and magnetic fields. Figure 1(b) shows the temperature dependence of current-voltage (IV) characteristics of the junction-1, demonstrating a clear induced supercurrent at 10 mK. Similar to other samples, there is no significant change in the supercurrent up to $\sim$ 300-400 mK. This suggests that Kondo hybridization is strong in this temperature regime where we believe that the singlets formed on the surface states predominantly carry the supercurrent. Beyond that regime, we see a monotonic drop in the critical current (I_c) until all signs of induced superconductivity vanishes. For most of the devices, supercurrent

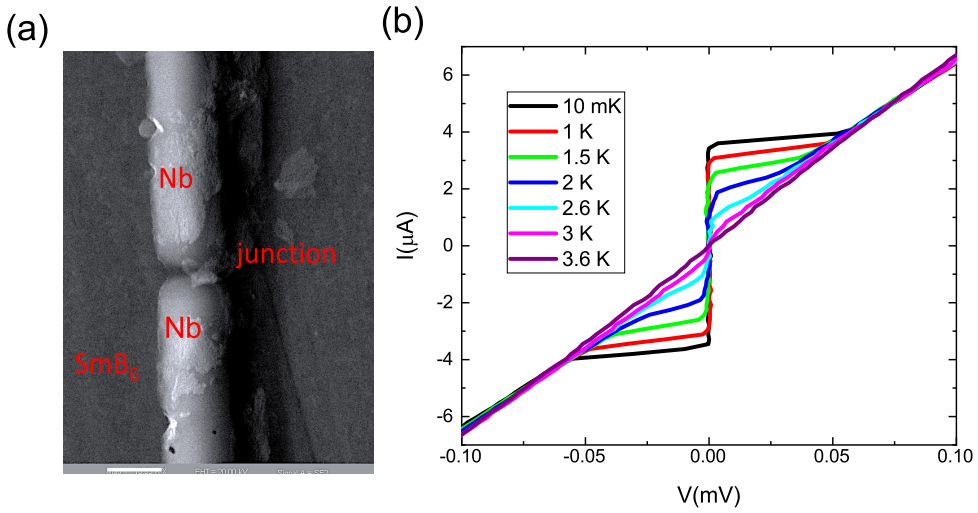

Figure 1. (Color online) (a) Scanning electron microscopy SEM image of one of the studied devices, junction-1, made with two Nb leads ~ 100 nm apart on a polished crystal of SmB_6. (b) Current-voltage I-V characteristics of the junction-1 for a set of temperatures. The supercurrent persists up to 3.6 K.

survives up to 3-6 K [33]. This differs in proximity-induced Nb/Bi_2Se_3 devices where superconductivity often is suppressed well below the T_c of the Niobium, approximately beyond 1 K [11, 12].

To confirm the presence of the Josephson effect in our junctions, we performed AC Josephson effect measurements by means of microwave irradiation. For a junction with 2π periodic Josephson relation, microwaves applied at a frequency of f gives rise to stair-like features in the IV characteristics with voltage spacing of $\Delta V = hf/2e$. These features are known as Shaphiro steps and correspond to minima in differential resistance vs bias current measurements [34].

To observe Shaphiro steps, the junctions are irradiated by microwaves by means of a coaxial cable whose center pin is about 1 mm vertically away from the surface of the sample. Figure 2(a) shows IV characteristics for a set of microwave power values for junction-1. As the microwave power is increased, the Shaphiro steps start to appear beyond 4 dBm that survive up to 3 K as seen from the temperature dependence measurements of dV/dI of the

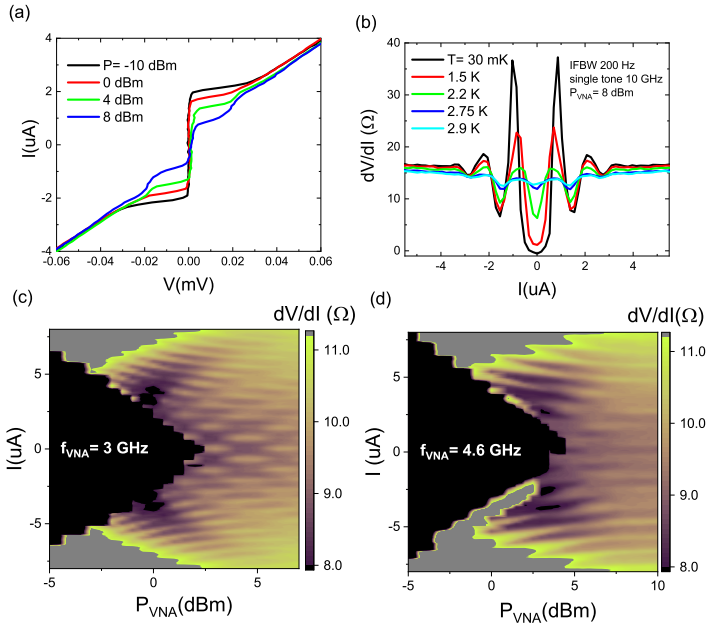

Figure 2. (Color online) (a) AC Josephson effect giving rise to Shaphiro steps in IV and (b) corresponding peaks in differential resistance for another sample, junction-1. (c) and (d) Color plots demonstrating such steps for junction-2 at two different frequencies.

same junction in Fig. 2(b). The voltage spacing of the Shaphiro steps is 20 μV as expected from the applied 10 GHz microwave tone, signifying that the current-phase relationship is 2π periodic.

We observed Shaphiro steps in multiple devices; Figs. 2(c) and (d) show color plots of dV/dI vs bias current and microwave power for junction-2 at two different frequencies, 3 and 4.6 GHz respectively. Upon increasing microwave power, the I_c monotonously decreases and finally vanishes at roughly 2.5 dBm for 3 GHz and 5 dBm for 4.6 GHz. Beyond these power levels I_c starts to oscillate with higher power supporting the 2π periodic AC Josephson effect further.

Now we turn to the out-of plane magnetic field response of the supercurrent. Figure 3(a) shows magnetic field oscillations of the I_c for the junction-3 at 10 mK that is similar to a Fraunhofer pattern. This pattern is another characteristic of the Josephson effect and is

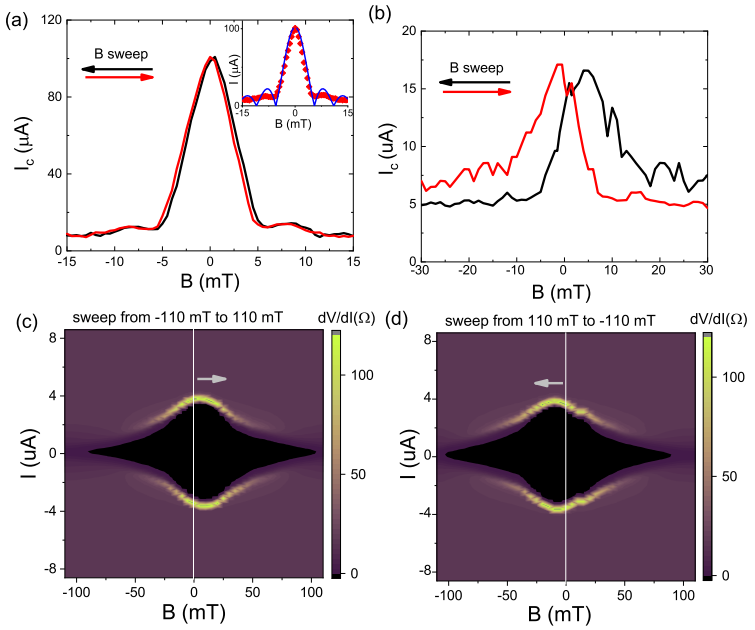

Figure 3. (Color online) (a), (b) Magnetic diffraction patterns of the I_c for the junction-3 and the junction-2 as the out of plane magnetic field is swept in forward and reverse directions. (c) and (d) Color plots of dV/dI vs bias current as a function of perpendicular magnetic field for the junction-1, clearly showing a discernible shift of I_c with respect to the sweep direction.

generated by quantum interference from phase winding induced by the magnetic flux within the junction. When a perpendicular field is applied to a conventional junction the phase will vary along the barrier, thus the supercurrent through the barrier will modulate with flux according to $I_c(\Phi) = I_c(0)\ |(\sin(\pi\Phi)/\Phi_0)/(\pi\Phi)/\Phi_0)|$ where Φ_0 is magnetic flux quantum. The inset of the Fig. 3(a) shows a theoretical Fraunhofer pattern plotted with the measured data acquired with increasing magnetic field sweep, demonstrating a reasonable agreement between the two.

The magnetic field response of I_c is quite different for junction-2, as shown Fig 3(b). First, there is a distinct lack of side lobes in the diffraction pattern demonstrating significant deviations from a conventional Fraunhofer pattern. Second, the maximum critical current occurs at about ± 5 mT instead of zero field. We attribute this shift in applied field axis with respect to the ideal Fraunhofer diffraction pattern to the existence of magnetization

in the SmB_6 surface states, which generates additional flux that must be cancelled out by an applied magnetic field in order to observe maximal critical current. The origin of such magnetism will be discussed later in the text. Although the direction where the central peak of diffraction pattern shifts is unexpected, similar hysteresis was observed in Sr_2RuO_4 due to multiple, dynamical domains of order parameter generating chiral supercurrents [35].

As we were performing these hysteresis measurements, we observed discernible suppressed supercurrent at zero field when the magnetic field is ramped down from a positive value. To check whether such suppression might be due to flux trapping or vortex entry, the fridge was warmed up to 20 K, well above the critical temperature of Nb and the superconducting magnet and then cooled back down to base temperature again. Before applying any magnetic field, we observed similar suppressed critical current at zero field which confirmed that the hysteresis in our diffraction patterns is not due to trapped vortices but possibly due to ferromagnetic behavior of surface states in SmB_6. The maximum critical current was only revived after sweeping the magnet in the opposite polarity.

The color plots of dV/dI vs bias current and applied magnetic field for junction-1 at 10 mK are shown in Fig. 3(c) and (d). Once again the diffraction pattern lacks side lobes. However, here the shift is in the opposite direction as for junction-2. Previously, superconductor-ferromagnet-superconductor (SFS) Josephson junctions showed anomalous Fraunhofer patterns with hysteretic behavior similar to data shown in Fig. 3(c) and (d); demonstrating maximal supercurrent occurring at nonzero applied field [36]. More recently, hysteretic magnetotransport has been observed in topological systems such as magnetically doped Bi_2Se_3 [37] and SmB_6, which have been also associated with ferromagnetic domain walls in surface states [27].

At low temperatures, we expect the formation of Kondo singlets in SmB_6 without magnetic behavior. We can explain the appearance of ferromagnetic behavior by invoking a Kondo breakdown [38, 39], which liberates a large number of randomly oriented magnetic moments that were previously coupled to conduction electrons inside Kondo singlets. When

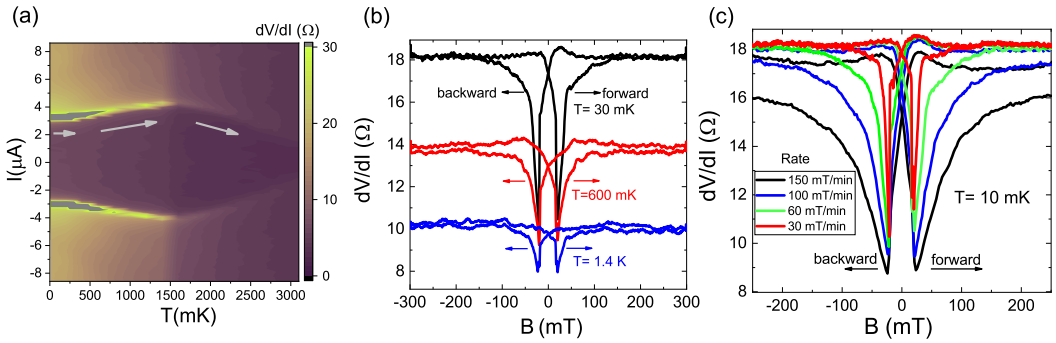

Figure 4. (Color online) (a) Color plot of dV/dI vs bias current as a function of temperature for junction-4. (b) Temperature evolution of hysteresis in normal state resistance with sweep direction for junction-4. (c) Rate dependence of magnetic field hysteresis in normal state resistance of junction-4.

we have a significant population of f-electrons, the material can have magnetic behavior even at mK temperatures. The breakdown of the Kondo effect at the layers close to the boundary of the sample stems from the reduced screening of the local moments due to broken translational symmetry at the outmost layers. This leads to a major modification in the band structure and reduces the Kondo temperature significantly.

When the Kondo hybridization is strong and the surface states are not subject to Kondo breakdown, we obtain more conventional magnetic diffraction patterns with no sensitivity to field sweep direction as shown in Fig. 3(a). As the spins are freed from the Kondo singlets due to the breakdown, they can form ferromagnetic domains on the surface generating negative or positive flux within the junction barrier. This will lead to modifications in Fraunhofer patterns with the shifts of the maximum supercurrent towards either positive or negative magnetic field. Similar phenomenon was observed in Ref [35].

Finally, in junction-4 we observe an anomalous temperature dependence of the I_c that can also be explained by a Kondo breakdown. Figure 4(a) shows a color plot of dV/dI vs temperature and bias current demonstrating the full evolution of I_c as the sample is heated. Critical current shows distinctive behavior in three different temperature regimes. For very low temperatures (i.e. below 300 mK), it exhibits almost no change. In this

regime, we expect that Kondo hybridization is strong and that the supercurrent is carried purely by the protected surface states. Then the I_c gradually increases between 300 mK and 1.6 K. Although this observation is unexpected from a usual Josephson junction, it could be consistent with the thermal population of trivial carriers either in the bulk or surface at higher temperatures that can carry additional supercurrent in parallel with the topological surface states (Kondo singlets) in SmB_6 triggered by the Kondo breakdown. Indeed, we observe the normal state resistance monotonically decreases with increasing temperature, as trivial states are being thermally activated. Furthermore, it is reported that especially the (001) surface of SmB_6 is polar [40] which gives rise to various modifications of the surface states, such as band bending, formation of 2D electron gases and quantum well confinements [41]. It is conceivable that different conditions at the surface could be caused by uncontrolled variations of the nanofabrication or sample/crystal preparation such as polishing. Beyond 1.6 K the critical current monotonously declines until the induced superconductivity is destroyed beyond 3-4 K. In this regime, the free magnetic moments due to Kondo breakdown are possibly too dominant to be screened by the Kondo singlets. Thermal dephasing of such moments can explain the rapid decrease in supercurrent.

In the same junction we also observe unusual properties of the normal state. Normal state conductance has been studied by applying a bias current that is much larger than the critical current. The longitudinal magnetoresistance data at low temperatures and low fields exhibits a sharp suppression in normal state resistance (R_N) near zero field as seen in Fig. 4(b). Intriguingly, when we change the sweep direction of the magnetic field, we observe a butterfly-shaped hysteretic behavior of magnetoresistance [42] with two separate minima at B_{min} = ± 24 mT. This feature was previously attributed elsewhere to edge channels between ferromagnetic domains in SmB_6 [27]. However, one must also consider trivial explanations for such magnetic hysteresis, including magnetocaloric effects or magnetic impurity scattering on the surface of the material [43]. As we increase the temperature, the hysteretic signal gets weaker as the ferromagnetism is suppressed by thermal fluctuations.

The dip feature is reminiscent of data that appears at zero field magnetoresistance in spin-orbit coupled materials due to weak antilocalization effect, which is a correction to classical magnetoresistance arising from quantum interference of scatted electron waves. The clear hysteresis of the dips and magnetic sweep rate dependent R_N as seen in Fig. 4(c) suggest that the features emerging in low temperature magnetoresistance are not due to a weak antilocalization effect.

3. CONCLUSION

In conclusion, we created and studied an unconventional Josephson junction using the surface states of a Kondo insulator as a weak link between superconducting leads. The observed critical temperature of the induced supercurrent is much higher compared to other proximity-induced topological Josephson devices [33, 44]. With the microwave irradiation of the junctions, we obtained clear Shaphiro steps in IV characteristics and dV/dI oscillations beyond the suppression of the supercurrent which are manifestations of the AC Josephson effect. The junctions demonstrated hysteretic response to out-of-plane magnetic field. The ferromagnetism at the surface at low temperatures can be attributed to a Kondo breakdown which generates free magnetic spins by breaking the Kondo singlets. Similar hysteresis was also observed in the normal state magnetoresistance supporting the claims about magnetic properties of the outmost layers further.

ACKNOWLEDGEMENTS

CK acknowledges funding by UMRB. For the device fabrication, we used the facilities of Missouri S&T Materials Research Center. We would like to thank Corey Buris and Clarisa Wisner for their assistance in device preparation. We thank David Pomerenke for microwave amplifiers, and Dale Harlingen for his ion beam facilities. We appreciate the discussions with Onur Erten and Joseph Glick.

REFERENCES

[1] Masatoshi Sato and Yoichi Ando. Topological superconductors: a review. *Reports on Progress in Physics*, 80(7):076501, 2017. URL http://stacks.iop.org/0034-4885/80/i=7/a=076501.

[2] E. Majorana. A symmetric theory of electrons and positrons. *Nuovo Cimento*, 14:171, 1937.

[3] F. Wilczek. Majorana returns. *Nat. Phys.*, 5:614, 2009. doi: 10.1038/nphys1380.

[4] J. Alicea. New directions in the pursuit of Majorana fermions in solid state systems. *Rep. Prog. Phys.*, 75(7):076501, 2012.

[5] C.W.J. Beenakker. Search for Majorana fermions in superconductors. *Annu. Rev. Con. Mat. Phys.*, 4:113, 2013. doi: 10.1146/annurev-conmatphys-030212-184337.

[6] Eytan Grosfeld and Ady Stern. Observing Majorana bound states of Josephson vortices in topological superconductors. *Proceedings of the National Academy of Sciences*, 108(29):11810–11814, 2011. doi: 10.1073/pnas.1101469108. URL http://www.pnas.org/content/108/29/11810.abstract.

[7] Martin Leijnse and Karsten Flensberg. Introduction to topological superconductivity and Majorana fermions. *Semicond. Sci. and Technol.*, 27(12):124003, 2012.

[8] Liang Fu and C. L. Kane. Superconducting Proximity Effect and Majorana Fermions at the Surface of a Topological Insulator. *Phys. Rev. Lett.*, 100:096407, Mar 2008. doi: 10.1103/PhysRevLett.100.096407.

[9] J. R. Williams, A. J. Bestwick, P. Gallagher, Seung Sae Hong, Y. Cui, Andrew S. Bleich, J. G. Analytis, I. R. Fisher, and D. Goldhaber-Gordon. Unconventional Josephson Effect in Hybrid Superconductor-Topological Insulator Devices. *Phys. Rev. Lett.*, 109:056803, Jul 2012. doi: 10.1103/PhysRevLett.109.056803. URL http://link.aps.org/doi/10.1103/PhysRevLett.109.056803.

[10] Cihan Kurter, Aaron D. K. Finck, Yew San Hor, and Dale J. Van Harlingen. Evidence for an anomalous current–phase relation in topological insulator Josephson junctions. *Nat. Commun.*, 6:7130, 2015.

[11] Martin P. Stehno, Vladimir Orlyanchik, Christopher D. Nugroho, Pouyan Ghaemi, Matthew Brahlek, Nikesh Koirala, Seongshik Oh, and Dale J. Van Harlingen. Signature of a topological phase transition in the Josephson supercurrent through a topological insulator. *Phys. Rev. B*, 93:035307, 2016.

[12] Sungjae Cho, Brian Dellabetta, Alina Yang, John Schneeloch, Zhijun Xu, Tonica Valla, Genda Gu, Matthew J. Gilbert, and Nadya Mason. Symmetry protected Josephson supercurrents in three-dimensional topological insulators. *Nat. Commun.*, 4:1689, 2013. URL http://dx.doi.org/10.1038/ncomms2701.

[13] Jian Wang, Cui-Zu Chang, Handong Li, Ke He, Duming Zhang, Meenakshi Singh, Xu-Cun Ma, Nitin Samarth, Maohai Xie, Qi-Kun Xue, and M. H. W. Chan. Interplay between topological insulators and superconductors. *Phys. Rev. B*, 85:045415, Jan 2012. doi: 10.1103/PhysRevB.85.045415. URL http://link.aps.org/doi/10.1103/PhysRevB.85.045415.

[14] M. Veldhorst, M. Snelder, M. Hoek, T. Gang, V. K. Guduru, X. L. Wang, U. Zeitler, W. G. van der Wiel, A. A. Golubov, H. Hilgenkamp, and A. Brinkman. Josephson supercurrent through a topological insulator surface state. *Nat. Mater.*, 11:417, 2012. URL dx.doi.org/10.1038/nmat3255.

[15] Fanming Qu, Fan Yang, Jie Shen, Yue Ding, Jun Chen, Zhongqing Ji, Guangtong Liu, Jie Fan, Xiunian Jing, Changli Yang, and Li Lu. Strong Superconducting Proximity Effect in Pb-Bi_2Te_3 Hybrid Structures. *Sci. Rep.*, 2:339, 2012. URL http://dx.doi.org/10.1038/srep00339.

[16] Benjamin Sacépé, Jeroen B. Oostinga, Jian Li, Alberto Ubaldini, Nuno J.G. Couto, Enrico Giannini, and Alberto F. Morpurgo. Gate-tuned normal and superconducting transport at the surface of a topological insulator. *Nat. Commun.*, 2:575, 2011. URL http://dx.doi.org/10.1038/ncomms1586.

[17] Duming Zhang, Jian Wang, Ashley M. DaSilva, Joon Sue Lee, Humberto R. Gutierrez, Moses H. W. Chan, Jainendra Jain, and Nitin Samarth. Superconducting proximity effect and possible evidence for Pearl vortices in a candidate topological insulator. *Phys. Rev. B*, 84:165120, Oct 2011. doi: 10.1103/PhysRevB.84.165120. URL http://link.aps.org/doi/10.1103/PhysRevB.84.165120.

[18] Hadar Steinberg, Dillon R. Gardner, Young S. Lee, and Pablo Jarillo-Herrero. Surface State Transport and Ambipolar Electric Field Effect in Bi_2Se_3 Nanodevices. *Nano Lett.*, 10(12):5032–5036, 2010. doi: 10.1021/nl1032183. URL http://dx.doi.org/10.1021/nl1032183.

[19] C. Kurter, A. D. K. Finck, P. Ghaemi, Y. S. Hor, and D. J. Van Harlingen. Dynamical gate-tunable supercurrents in topological Josephson junctions. *Phys. Rev. B*, 90:014501, Jul 2014. doi: 10.1103/PhysRevB.90.014501. URL http://link.aps.org/doi/10.1103/PhysRevB.90.014501.

[20] Maxim Dzero, Kai Sun, Victor Galitski, and Piers Coleman. Topological Kondo Insulators. *Phys. Rev. Lett.*, 104: 106408, Mar 2010. doi: 10.1103/PhysRevLett.104.106408. URL https://link.aps.org/doi/10.1103/PhysRevLett.104.106408.

[21] Maxim Dzero, Kai Sun, Piers Coleman, and Victor Galitski. Theory of topological Kondo insulators. *Phys. Rev. B*, 85: 045130, Jan 2012. doi: 10.1103/PhysRevB.85.045130. URL https://link.aps.org/doi/10.1103/PhysRevB.85.045130.

[22] Maxim Dzero, Jing Xia, Victor Galitski, and Piers Coleman. Topological Kondo Insulators. *Annual Review of Condensed Matter Physics*, 7(1): 249–280, 2016. doi: 10.1146/annurev-conmatphys-031214-014749. URL https://doi.org/10.1146/annurev-conmatphys-031214-014749.

[23] Xiaohang Zhang, N. P. Butch, P. Syers, S. Ziemak, Richard L. Greene, and Johnpierre Paglione. Hybridization, Inter-Ion Correlation, and Surface States in the Kondo Insulator SmB_6. *Phys. Rev. X*, 3:011011, Feb 2013. doi: 10.1103/PhysRevX.3.011011. URL https://link.aps.org/doi/10.1103/PhysRevX.3.011011.

[24] J. W. Allen, B. Batlogg, and P. Wachter. Large low-temperature Hall effect and resistivity in mixed-valent SmB_6. *Phys. Rev. B*, 20:4807–4813, Dec 1979. doi: 10.1103/PhysRevB.20.4807. URL https://link.aps.org/doi/10.1103/PhysRevB.20.4807.

[25] D. J. Kim, J. Xia, and Z. Fisk. Topological surface state in the kondo insulator samarium hexaboride. *Nature Mater.*, 13:466, 2014.

[26] M. Neupane, N. Alidoust, S.-Y. Xu, T. Kondo, Y. Ishida, D. J. Kim, Chang Liu, I. Belopolski, Y. J. Jo, T.-R. Chang, H.-T. Jeng, T. Durakiewicz, L. Balicas, H. Lin, A. Bansil, S. Shin, Z. Fisk, and M. Z. Hasan. Surface electronic structure of the topo-logical Kondo-insulator candidate correlated electron system SmB_6. *Nature Commun.*, 4:2991, 2013.

[27] Yasuyuki Nakajima, Paul Syers, Renxiong Wang, Xiangfeng abd Wang, and Johnpierre Paglione. One-dimensional edge state transport in a topological Kondo insulator. *Nature Phys.*, 12:213, 2016.

[28] D. J. Kim, S. Thomas, T. Grant, J. Botimer, Z. Fisk, and Jing Xia. Surface Hall Effect and Nonlocal Transport in SmB_6: Evidence for Surface Conduction. *Sci. Rep.*, 3: 3150, 2013.

[29] Jehyun Kim, Chaun Jang, Xiangfeng Wang, Johnpierre Paglione, Seokmin Hong, and Dohun Kim. Electrical detection of surface spin polarization of candidate topological kondo insulator smb_6. *arXiv:1809.04977*, 2018.

[30] S. Lee, V. Stanev, X. Zhang, D. Stasak, J. Flowers, J. S. Higgins, S. Dai, T. Blum, X. Pan, V. M. Yakovenko, J. Paglione, R. L. Greene, V. Galitski, and I. Takeuchi. Perfect andreev reflection due to the klein paradox in a topological superconducting state. *Nature*, 570:344–348, 2019.

[31] N. Xu, P. K. Biswas, J. H. Dil, R. S. Dhaka, G. Landolt, S. Muff, C. E. Matt, X. Shi, N. C. Plumb, M. Radovic, E. Pomjakushina, K. Conder, A. Amato, S. V. Borisenko,

R. Yu, H. M. Weng, Z. Fang, X. Dai, J. Mesot, H. Ding, and M. Shi. Direct observation of the spin texture in strongly correlated SmB_6 as evidence of the topological Kondo insulator. *Nat. Commun.*, 5:4566, 2014.

[32] Wei Ruan, Cun Ye, Minghua Guo, Fei Chen, Xianhui Chen, Guang-Ming Zhang, and Yayu Wang. Emergence of a Coherent In-Gap State in the SmB_6 Kondo Insulator Revealed by Scanning Tunneling Spectroscopy. *Phys. Rev. Lett.*, 112:136401, Mar 2014. doi: 10.1103/PhysRevLett.112.136401. URL https://link.aps.org/doi/10.1103/PhysRevLett.112.136401.

[33] Seunghun Lee, Xiaohang Zhang, Yangang Liang, Sean W. Fackler, Jie Yong, Xi-angfeng Wang, Johnpierre Paglione, Richard L. Greene, and Ichiro Takeuchi. Obser-vation of the Superconducting Proximity Effect in the Surface State of SmB_6 Thin Films. *Phys. Rev. X*, 6:031031, Aug 2016. doi: 10.1103/PhysRevX.6.031031. URL https://link.aps.org/doi/10.1103/PhysRevX.6.031031.

[34] R. A. Snyder, C. J. Trimble, C. C. Rong, P. A. Folkes, P. J. Taylor, and J. R. Williams. Weak-link josephson junctions made from topological crystalline insulators. *Phys. Rev. Lett.*, 121:097701, Aug 2018. doi: 10.1103/PhysRevLett.121.097701. URL https://link.aps.org/doi/10.1103/PhysRevLett.121.097701.

[35] F. Kidwingira, J. D. Strand, D. J. Van Harlingen, and Y. Maeno. Dynamical Super-conducting Order Parameter Domains in Sr_2RuO_4. *Science*, 314:1267, 2006.

[36] Trupti S. Khaire, W. P. Pratt, and Norman O. Birge.Critical current behavior in Josephson junctions with the weak ferromagnet PdNi. *Phys. Rev. B*, 79:094523, Mar 2009. doi: 10.1103/PhysRevB.79.094523. URL https://link.aps.org/doi/10.1103/PhysRevB.79.094523.

[37] J. G. Checkelsky, J. Ye, Y. Onone, Y. Iwasa, and Y. Tokura. Dirac-fermion-mediated ferromagnetism in a topological insulator. *Nature Phys.*, 8:729, 2012.

[38] Victor Alexandrov, Piers Coleman, and Onur Erten. Kondo break-down in topological kondo insulators. *Phys. Rev. Lett.*, 114: 177202, Apr 2015. doi: 10.1103/PhysRevLett.114.177202. URL https://link.aps.org/doi/10.1103/PhysRevLett.114.177202.

[39] Onur Erten, Pouyan Ghaemi, and Piers Coleman. Kondo Break-down and Quantum Oscillations in SmB_6. *Phys. Rev. Lett.*, 116: 046403, Jan 2016. doi: 10.1103/PhysRevLett.116.046403. URL https://link.aps.org/doi/10.1103/PhysRevLett.116.046403.

[40] Z.-H. Zhu, A. Nicolaou, G. Levy, N. P. Butch, P. Syers, X. F. Wang, J. Paglione, G. A. Sawatzky, I. S. Elfimov, and A. Damas-celli. Polarity-Driven Surface Metallicity in SmB_6. *Phys. Rev. Lett.*, 111:216402, Nov 2013. doi: 10.1103/PhysRevLett.111.216402. URL https://link.aps.org/doi/10.1103/PhysRevLett.111.216402.

[41] L. Jiao, S. Robler, D. J. Kim, L. H. Tjeng, Z. Fisk, F. Steglich, and S. Wirth. Additional energy scale in SmB_6 at low-temperature. *Nat. Commun.*, 7:13762, 2016.

[42] Xingshuai He, Haibo Gan, Zongzheng Du, Bicong Ye, Liang Zhou, Yuan Tian, Shaozhi Deng, Guoping Guo, Haizhou Lu, Fei Liu, and Hongtao He. Magnetore-sistance anomaly in topological kondo insulator smb6 nanowires with strong surface magnetism. *Advanced Science*, 5(7):1700753, 2018. doi: 10.1002/advs.201700753.

[43] S. Wolgast, Y. S. Eo, T. Öztürk, G. Li, Z. Xiang, C. Tinsman, T. Asaba, B. Lawson,
F. Yu, J. W. Allen, K. Sun, L. Li, C. Kurdak, D.-J. Kim, and Z. Fisk. Magneto-transport measurements of the surface states of samarium hexaboride using corbino structures. *Phys. Rev. B*, 92:115110, Sep 2015. doi: 10.1103/PhysRevB.92.115110. URL https://link.aps.org/doi/10.1103/PhysRevB.92.115110.

[44] Zhu Lin, Yong Zhou, Ling-Jian Kong, Dongsheng Tang, Hai-Zhou Lu, Shiu-Ming Huang, Rui Zhu, Jun Xu, Fang Lin, Jianbo Wang, Zhi-Min Liao, and Dapeng Yu. In-terplay between topological surface states and superconductivity in Smb_6/NbN tunnel junctions. *Phys. Rev. B*, 96:165408, Oct 2017. doi: 10.1103/PhysRevB.96.165408. URL https://link.aps.org/doi/10.1103/PhysRevB.96.165408.

SECTION

2. SUMMARY AND CONCLUSIONS

In this dissertation, we have studied the effects of disorder on two different kinds of problems: (i) the formation of stripe phase in a frustrated magnet and (ii) the nonequilibrium transition in the contact process. We have also included an experimental study of Josephson junctions.

In the first section of the dissertation, we introduced some general concepts in the physics of phase transitions such as Laudau theory, order parameter, and scaling hypothesis. Because clean systems are well-studied and hard to achieve in the real world, we then introduced phase transitions under the influence of disorder. We distinguished two different kinds of disorder: random-field disorder and random-mass disorder. We discussed how the Imry-Ma and Harris criteria determine the stability of phases and phase transitions against disorders. We then gave a short introduction into rare regions and Griffiths effects. In order to familiarlize the reader with topics of papers 1 to 3, we gave a basic introduction into the contact process and the $J_1 - J_2$ Ising model. We then introduced two basic concepts of my experimental study: Josephson junctions and topological insulators.

The first paper studied the stability of the stripe phase in disordered s ystem. Such a stripe phase is unstable under uncorrelated disorder due to random-field m echanism. By combining symmetry arguments, percolation theory and large-scale Monte Carlo simulations, we proved that introducing a weak spatial interaction anisotropy can restore the stripe phase. We also explained the phase transition using percolation theory.

The second paper studied the 1D contact process under both spatial and temporal disorders. We discussed the stability of directed percolation universality class against such disorder by using a generalized Harris criterion. We confirmed our theory by performing large-scale Monte Carlo simulations. We also studied the Griffiths singularities to further compare theory and simulations.

The third, experimental paper studied unconvensional Josephson junction using the Kondo insulator SmB_6. We have constructed a Josephson junction by coupling superconducting Nb leads to surface states of a SmB_6 crystal, and found a robust critical current at low temperatures. Such critical currents as well as their Shaphiro steps behavior prove the existence of Josephson effect.

Our research raises a number of interesting questions that can be studied in the future. The study of the effects of simultaneous spatial and temporal disorders can be extended to higher dimensions and to other nonequilibrium transitions. To better understand the stability of the stripe phase, weak interlayer couplings (that are present in real 3D materials) need to be included. Although the present research focused on the thermodynamic behavior of the stripe phase, it is also interesting to study the real-time dynamics. More realistic models can be used to estimate quantitatively the phase transition of real materials and real-world problems such as the spreading of a disease.

REFERENCES

[1] L. D. Landau. *Phys. Z. Sowjetunion*, 11:26, 1937.

[2] L. D. Landau. Theory of phase transformations. i. *Zh. Eksp. Teor. Fiz.*, 7:19, 1937. [Phys. Z. Sowjetunion 11, 26 (1937)].

[3] L. D. Landau. *Phys. Z. Sowjetunion*, 11:545, 1937.

[4] L. D. Landau. Theory of phase transformations. ii. *Zh. Eksp. Teor. Fiz.*, 7:627, 1937. [Phys. Z. Sowjetunion 11, 545 (1937)].

[5] B. Widom. Surface tension and molecular correlations near the critical point. *J. Chem. Phys.*, 43:3892, 1965.

[6] Leo P Kadanoff, Wolfgang Götze, David Hamblen, Robert Hecht, EAS Lewis, V V Palciauskas, Martin Rayl, J Swift, David Aspnes, and Joseph Kane. Static phenomena near critical points: theory and experiment. *Reviews of Modern Physics*, 39(2):395, 1967.

[7] BD Josephson. Inequality for the specific heat: I. derivation. *Proceedings of the Physical Society (1958-1967)*, 92(2):269, 1967.

[8] GS Rushbrooke. On the thermodynamics of the critical region for the ising problem. *The Journal of Chemical Physics*, 39(3):842–843, 1963.

[9] Lars Onsager. Crystal statistics. i. a two-dimensional model with an order-disorder transition. *Phys. Rev.*, 65:117–149, Feb 1944. doi: 10.1103/PhysRev.65.117. URL http://link.aps.org/doi/10.1103/PhysRev.65.117.

[10] Yoseph Imry and Shang-keng Ma. Random-field instability of the ordered state of continuous symmetry. *Phys. Rev. Lett.*, 35:1399–1401, Nov 1975. doi: 10.1103/PhysRevLett.35.1399.

[11] Yoseph Imry and Michael Wortis. Influence of quenched impurities on first-order phase transitions. *Phys. Rev. B*, 19:3580–3585, Apr 1979. doi: 10.1103/PhysRevB.19.3580.

[12] Michael Aizenman and Jan Wehr. Rounding of first-order phase transitions in systems with quenched disorder. *Phys. Rev. Lett.*, 62:2503–2506, May 1989. doi: 10.1103/PhysRevLett.62.2503.

[13] Michael Aizenman, Rafael L. Greenblatt, and Joel L. Lebowitz. Proof of rounding by quenched disorder of first order transitions in low-dimensional quantum systems. *J. Math. Phys.*, 53(2):023301, 2012. doi: http://dx.doi.org/10.1063/1.3679069. URL http://scitation.aip.org/content/aip/journal/jmp/53/2/10.1063/1.3679069.

[14] A. B. Harris. Effect of random defects on the critical behaviour of Ising models. *J. Phys. C*, 7:1671, 1974. doi: 10.1088/0022-3719/7/9/009.

[15] D. S. Fisher. Critical behavior of random transverse-field Ising spin chains. *Phys. Rev. B*, 51:6411, 1995. doi: 10.1103/PhysRevB.51.6411.

[16] Thomas Vojta and Ronald Dickman. Spatiotemporal generalization of the harris criterion and its application to diffusive disorder. *Phys. Rev. E*, 93:032143, Mar 2016. doi: 10.1103/PhysRevE.93.032143.

[17] T. Vojta. Rare region effects at classical, quantum, and non-equilibrium phase transi-tions. *J. Phys. A*, 39:R143, 2006. doi: 10.1088/0305-4470/39/22/R01.

[18] R. B. Griffiths. Nonanalytic behavior above the critical point in a random Ising ferromagnet. *Phys. Rev. Lett.*, 23:17, 1969. doi: 10.1103/PhysRevLett.23.17.

[19] T. Vojta and J. Schmalian. Quantum Griffiths effects in itinerant Heisenberg magnets. *Phys. Rev. B*, 72:045438, 2005. doi: 10.1103/PhysRevB.72.045438.

[20] B. M. McCoy and T. T. Wu. Random impurities as the cause of smooth specific heats near the critical temperature. *Phys. Rev. Lett.*, 21:549, 1968.

[21] B. M. McCoy and T. T. Wu. Theory of a two-dimensional Ising model with random impurities. i. thermodynamics. *Phys. Rev.*, 176:631, 1968.

[22] B. M. McCoy and T. T. Wu. Theory of a two-dimensional Ising model with random impurities. ii. spin correlation functions. *Phys. Rev.*, 188:982, 1969.

[23] B. M. McCoy. Theory of a two-dimensional Ising model with random impurities. iii. boundary effects. *Phys. Rev.*, 188:1014, 1969.

[24] Daniel S. Fisher. Random transverse field ising spin chains. *Phys. Rev. Lett.*, 69: 534–537, Jul 1992. doi: 10.1103/PhysRevLett.69.534.

[25] Rastko Sknepnek and Thomas Vojta. Smeared phase transition in a three-dimensional ising model with planar defects: Monte carlo simulations. *Phys. Rev. B*, 69:174410, May 2004. doi: 10.1103/PhysRevB.69.174410. URL https://link.aps.org/doi/10.1103/PhysRevB.69.174410.

[26] A. J. Millis, D. K. Morr, and J. Schmalian. Local defect in metallic quantum critical systems. *Phys. Rev. Lett.*, 87:167202, 2001.

[27] A. J. Millis, D. K. Morr, and J. Schmalian. Quantum Griffiths effects in metallic systems. *Phys. Rev. B*, 66:174433, 2002.

[28] Thomas Vojta. Disorder-induced rounding of certain quantum phase transitions. *Phys. Rev. Lett.*, 90:107202, Mar 2003. doi: 10.1103/PhysRevLett.90.107202.

[29] Songbo Jin, Arnab Sen, and Anders W. Sandvik. Ashkin-teller criticality and pseudo-first-order behavior in a frustrated ising model on the square lattice. *Phys. Rev. Lett.*, 108:045702, Jan 2012. doi: 10.1103/PhysRevLett.108.045702. URL https://link.aps.org/doi/10.1103/PhysRevLett.108.045702.

[30] Songbo Jin, Arnab Sen, Wenan Guo, and Anders W. Sandvik. Phase transitions in the frustrated ising model on the square lattice. *Phys. Rev. B*, 87:144406, Apr 2013. doi: 10.1103/PhysRevB.87.144406. URL https://link.aps.org/doi/10.1103/PhysRevB.87.144406.

[31] Ansgar Kalz, Andreas Honecker, and Marion Moliner. Analysis of the phase transition for the ising model on the frustrated square lattice. *Phys. Rev. B*, 84:174407, Nov 2011. doi: 10.1103/PhysRevB.84.174407. URL https://link.aps.org/doi/10.1103/PhysRevB.84.174407.

[32] Ansgar Kalz and Andreas Honecker. Location of the potts-critical end point in the frustrated ising model on the square lattice. *Phys. Rev. B*, 86:134410, Oct 2012. doi: 10.1103/PhysRevB.86.134410. URL https://link.aps.org/doi/10.1103/PhysRevB.86.134410.

[33] Shashikant Singh Kunwar, Arnab Sen, Thomas Vojta, and Rajesh Narayanan. Tuning a random-field mechanism in a frustrated magnet. *Phys. Rev. B*, 98:024206, Jul 2018. doi: 10.1103/PhysRevB.98.024206. URL https://link.aps.org/doi/10.1103/PhysRevB.98.024206.

[34] J. Marro and R. Dickman. *Nonequilibrium Phase Transitions in Lattice Models*. Cambridge University Press, Cambridge, 1999.

[35] T. E. Harris. Contact interactions on a lattice. *Ann. Prob.*, 2:969, 1974. doi: doi:10.1214/aop/1176996493.

[36] P. Grassberger and A. de la Torre. *Ann. Phys. (NY)*, 122:373, 1979. doi: 10.1016/0003-4916(79)90207-0.

[37] B. D. Josephson. Possible new effects in superconductive tunnelling. *Phys. Lett.*, 1: 251, 1962.

[38] Liang Fu and C. L. Kane. Superconducting Proximity Effect and Majorana Fermions at the Surface of a Topological Insulator. *Phys. Rev. Lett.*, 100:096407, Mar 2008. doi: 10.1103/PhysRevLett.100.096407.

[39] J. R. Williams, A. J. Bestwick, P. Gallagher, Seung Sae Hong, Y. Cui, Andrew S. Bleich, J. G. Analytis, I. R. Fisher, and D. Goldhaber-Gordon. Unconventional Josephson Effect in Hybrid Superconductor-Topological Insulator Devices. *Phys. Rev. Lett.*, 109:056803, Jul 2012. doi: 10.1103/PhysRevLett.109.056803. URL http://link.aps.org/doi/10.1103/PhysRevLett.109.056803.

[40] Cihan Kurter, Aaron D. K. Finck, Yew San Hor, and Dale J. Van Harlingen. Evidence for an anomalous current–phase relation in topological insulator Josephson junctions. *Nat. Commun.*, 6:7130, 2015.

[41] Martin P. Stehno, Vladimir Orlyanchik, Christopher D. Nugroho, Pouyan Ghaemi, Matthew Brahlek, Nikesh Koirala, Seongshik Oh, and Dale J. Van Harlingen. Signature of a topological phase transition in the Josephson supercurrent through a topological insulator. *Phys. Rev. B*, 93:035307, 2016.

[42] Sungjae Cho, Brian Dellabetta, Alina Yang, John Schneeloch, Zhijun Xu, Tonica Valla, Genda Gu, Matthew J. Gilbert, and Nadya Mason. Symmetry protected Josephson supercurrents in three-dimensional topological insulators. *Nat. Commun.*, 4:1689, 2013. URL http://dx.doi.org/10.1038/ncomms2701.

[43] Jian Wang, Cui-Zu Chang, Handong Li, Ke He, Duming Zhang, Meenakshi Singh, Xu-Cun Ma, Nitin Samarth, Maohai Xie, Qi-Kun Xue, and M. H. W. Chan. Interplay between topological insulators and superconductors. *Phys. Rev. B*, 85:045415, Jan 2012. doi: 10.1103/PhysRevB.85.045415. URL http://link.aps.org/doi/10.1103/PhysRevB.85.045415.

[44] M. Veldhorst, M. Snelder, M. Hoek, T. Gang, V. K. Guduru, X. L. Wang, U. Zeitler, W. G. van der Wiel, A. A. Golubov, H. Hilgenkamp, and A. Brinkman. Josephson supercurrent through a topological insulator surface state. *Nat. Mater.*, 11:417, 2012. URL dx.doi.org/10.1038/nmat3255.

[45] Fanming Qu, Fan Yang, Jie Shen, Yue Ding, Jun Chen, Zhongqing Ji, Guangtong Liu, Jie Fan, Xiunian Jing, Changli Yang, and Li Lu. Strong Superconducting Proximity Effect in Pb-Bi_2Te_3 Hybrid Structures. *Sci. Rep.*, 2:339, 2012. URL http://dx.doi.org/10.1038/srep00339.

[46] Benjamin Sacépé, Jeroen B. Oostinga, Jian Li, Alberto Ubaldini, Nuno J.G. Couto, Enrico Giannini, and Alberto F. Morpurgo. Gate-tuned normal and superconducting transport at the surface of a topological insulator. *Nat. Commun.*, 2:575, 2011. URL http://dx.doi.org/10.1038/ncomms1586.

[47] Duming Zhang, Jian Wang, Ashley M. DaSilva, Joon Sue Lee, Humberto R. Gutier-rez, Moses H. W. Chan, Jainendra Jain, and Nitin Samarth. Superconducting prox-imity effect and possible evidence for Pearl vortices in a candidate topological insu-lator. *Phys. Rev. B*, 84:165120, Oct 2011. doi: 10.1103/PhysRevB.84.165120. URL http://link.aps.org/doi/10.1103/PhysRevB.84.165120.

[48] M. Z. Hasan and C. L. Kane. *Colloquium* : Topological insulators. *Rev. Mod. Phys.*, 82:3045–3067, Nov 2010. doi: 10.1103/RevModPhys.82.3045. URL http://link.aps.org/doi/10.1103/RevModPhys.82.3045.

[49] This drawing is done by A13ean - Own work, CC BY-SA 3.0, https://commons.wikimedia.org/w/index.php?curid=11101461.

[50] Masatoshi Sato and Yoichi Ando. Topological superconductors: a review. *Reports on Progress in Physics*, 80(7):076501, 2017. URL http://stacks.iop.org/0034-4885/80/i=7/a=076501.

[51] Y. Xia, D. Qian, D. Hsieh, L. A. Wray, A. Pal, H. Lin, A. Bansil, D. Grauer, Y.S. Hor, R. J. Cava, and M.Z. Hasan. Observation of a large-gap topological-insulator class with a single dirac cone on the surface. *Nat. Phys.*, 5:398, 2009.

[52] Yang Xu, Ireneusz Miotkowski, Chang Liu, Jifa Tian, Hyoungdo Nam, Nasser Alidoust, Jiuning Hu, Chih-Kang Shih, M. Zahid Hasan, and Yong P. Chen. Observation of topological surface state quantum hall effect in an intrinsic three-dimensional topological insulator. *Nat. Phys.*, 10:956, 2014.

[53] Pavan Hosur, Pouyan Ghaemi, Roger S. K. Mong, and Ashvin Vishwanath. Majorana modes at the ends of superconductor vortices in doped topological insulators. *Phys. Rev. Lett.*, 107:097001, Aug 2011. doi: 10.1103/PhysRevLett.107.097001. URL http://link.aps.org/doi/10.1103/PhysRevLett.107.097001.

[54] C. W. J. Beenakker, D. I. Pikulin, T. Hyart, H. Schomerus, and J. P. Dahlhaus. Fermion-parity anomaly of the critical supercurrent in the quantum spin-hall effect. *Phys. Rev. Lett.*, 110:017003, Jan 2013. doi: 10.1103/PhysRevLett.110.017003. URL http://link.aps.org/doi/10.1103/PhysRevLett.110.017003.

[55] Maxim Dzero, Jing Xia, Victor Galitski, and Piers Coleman. Topological Kondo Insulators. *Annual Review of Condensed Matter Physics*, 7(1): 249–280, 2016. doi: 10.1146/annurev-conmatphys-031214-014749. URL https://doi.org/10.1146/annurev-conmatphys-031214-014749.

[56] Maxim Dzero, Victor Galitski, Kai Sun, and Piers Coleman. Topological Kondo Insulators. *Phys. Rev. Lett.*, 104: 106408, Mar 2010. doi: 10.1103/PhysRevLett.104.106408. URL https://link.aps.org/doi/10.1103/PhysRevLett.104.106408.

[57] Maxim Dzero, Kai Sun, Piers Coleman, and Victor Galitski. Theory of topological Kondo insulators. *Phys. Rev. B*, 85: 045130, Jan 2012. doi: 10.1103/PhysRevB.85.045130. URL https://link.aps.org/doi/10.1103/PhysRevB.85.045130.

[58] Seunghun Lee, Xiaohang Zhang, Yangang Liang, Sean W. Fackler, Jie Yong, Xiangfeng Wang, Johnpierre Paglione, Richard L. Greene, and Ichiro Takeuchi. Observation of the Superconducting Proximity Effect in the Surface State of SmB_6 Thin Films. *Phys. Rev. X*, 6:031031, Aug 2016. doi: 10.1103/PhysRevX.6.031031. URL https://link.aps.org/doi/10.1103/PhysRevX.6.031031.

[59] Zhu Lin, Yong Zhou, Ling-Jian Kong, Dongsheng Tang, Hai-Zhou Lu, Shiu-Ming Huang, Rui Zhu, Jun Xu, Fang Lin, Jianbo Wang, Zhi-Min Liao, and Dapeng Yu. Interplay between topological surface states and superconductivity in Smb_6/NbN tunnel junctions. *Phys. Rev. B*, 96:165408, Oct 2017. doi: 10.1103/PhysRevB.96.165408. URL https://link.aps.org/doi/10.1103/PhysRevB.96.165408.

VITA

Xuecheng Ye was born in Wuhan, China in 1991. He went through first and secondary schools in Wuhan and won 2nd prize in physics in national Olympics competition in high school. He went to the University of Science and Technology of China (USTC) in 2010 and earned his B.S. degree in physics there in 2014. After a year as research assistant working in Prof. Xiaoliang Xu's micro-nano functional materials group in USTC, he was then accepted by Missouri University of Science and Technology (Missouri S&T) in Rolla, USA, to pursue graduate education in 2015.

At Missouri S&T, he joined Dr. Cihan Kurter group to do experimental research on Kondo insulators. After Prof. Kurter left Missouri S&T, he joined Dr. Thomas Vojta's quantum many-particle research group in 2018 and worked on theory and simulations of phase transitions in disordered systems, until he earned his PhD degree in Physics in December 2022. Since 2020, he has been a member of the American Physical Society.